NAVAL POSTGRADUATE SCHOOL
Monterey, California

THESIS

REDUCTION OF MUTUAL COUPLING IN
SMALL DIPOLE ARRAY ANTENNAS

by

Chua Eng Hock

March 2003

Thesis Advisor:	David Jenn
Second Reader:	Richard Adler

Approved for public release, distribution is unlimited

THIS PAGE INTENTIONALLY LEFT BLANK

13. ABSTRACT *(maximum 200 words)*

The mutual coupling in phased array is a well-known phenomenon. It affects the active element pattern of the array as the phase of the individual element is altered. In an array that has many elements, the effect is identical for all the elements that are nearer to the center of the antenna, thus allowing a more predictable scan performance with respect to the phase of the elements. However, in a small array that has only three elements, the active element pattern for the elements at the end can be significantly different from the center element and this affects the predictability of operations such as direction finding.

The thesis investigates two ways that can potentially reduce or at least control the mutual coupling in small arrays. The first method simply adds a dummy element with a special load condition to each end of the array to make the edge element "feel" as if there are more elements next to it. The second method uses a passive feedback circuit to both monitor and correct the magnitude and phase of the mutual coupling at the input of each array element. A hybrid ring is attached to each of the elements to monitor the amount of interference received by that element.

Simulation results for the dummy element method shows that some reduction in phase error can be achieved if the spacing and length of the element are selected properly. The compensation network approach relies on an efficient two-port array element. The research has focused on the design of a two-port printed circuit dipole that could be used in such an array. The dipole was designed, simulated, and fabricated. Future research will use this element in a compensation network.

i

THIS PAGE INTENTIONALLY LEFT BLANK

**REDUCTION OF MUTUAL COUPLING IN
SMALL DIPOLE ARRAY ANTENNAS**

Chua Eng Hock
Major, The Republic of Singapore Navy
B.Eng., Nanyang Technological University, Singapore, 1992

Submitted in partial fulfillment of the
requirements for the degree of

MASTER OF SCIENCE IN SYSTEMS ENGINEERING

from the

**NAVAL POSTGRADUATE SCHOOL
March 2003**

Author: Chua Eng Hock

Approved by: David Jenn
                 Thesis Advisor

                 Richard Adler
                 Second Reader

                 Dan Boger
                 Chairman, Department of Information Sciences

THIS PAGE INTENTIONALLY LEFT BLANK

ABSTRACT

The mutual coupling in a phased array is a well-known phenomenon. It affects the active element pattern of the array as the phase of the individual element is altered. In an array that has many elements, the effect is identical for all the elements that are nearer to the center of the antenna, thus allowing a more predictable scan performance with respect to the phase of the elements. However, in a small array which has only three elements, the active element pattern for the elements at the ends can be significantly different from the center element pattern and this affects the predictability of operations such as direction finding.

The thesis investigates two ways that can potentially reduce or at least control the mutual coupling in small arrays. The first method simply adds a dummy element with a special load condition to each end of the array to make the edge element "feel" as if there are more elements next to it. The second method uses a passive feedback circuit to both monitor and correct the magnitude and phase of the mutual coupling at the input of each array element. A hybrid ring is attached to each of the elements to monitor the amount of interference received by that element.

Simulation results for the dummy element method shows that some reduction in phase error can be achieved if the spacing and length of the element are selected properly. The compensation network approach relies on an efficient two-port array element model. The research has focused on the design of a two-port printed circuit dipole that could be used in such an array. The dipole was designed, simulated, and fabricated. Future research will use this element in a compensation network.

THIS PAGE INTENTIONALLY LEFT BLANK

TABLE OF CONTENTS

LIST OF FIGURES

x

THIS PAGE INTENTIONALLY LEFT BLANK

LIST OF TABLES

THIS PAGE INTENTIONALLY LEFT BLANK

ACKNOWLEDGMENTS

I would like to express my most sincere gratitude to Professor David Jenn of the Naval Postgraduate School, Monterey, California for his guidance and invaluable contributions to the completion of this work. He has never failed to stop whatever work he is doing to attend to my questions and I really appreciate it. I would also like to thank Professor Richard Adler for agreeing to be the second reader to the thesis. Both of them have prepared me in electromagnetics, antenna theory and radar cross section theory while I was in Naval Postgraduate School and the knowledge acquired has allowed me to proceed with the thesis work.

I would also like to thank my wife Lim Yuen Yuen and my daughter Chua XueYi, for their supports back home in Singapore, without which I would not have been able to focus on my work. Much appreciations also go to my mother-in-law, Madam Kim for helping to take good care of my daughter and my wife while I am away from Singapore.

THIS PAGE INTENTIONALLY LEFT BLANK

I.   INTRODUCTION

A.   MUTUAL COUPLING EFFECTS

The existence of mutual coupling between elements in a phased array antenna affects the final antenna pattern and it cannot be neglected in the design of high performance arrays. It can be significant in applications that demand high accuracy for direction finding (DF). In a large phased array, the coupling effect is generally uniform for most of the elements except for the last few elements near the edge. The effect near the end of the array is known as the edge-effect.

For a majority of the elements in a large phased array, the active element pattern approach [Ref. 4] has helped designers to overcome the complex effects of the mutual coupling. Elements at the edges are usually assumed to have the same active element pattern as the center element. The rationale is that the number of edge elements in a large array is small compared to the number of non-edge elements, and therefore mutual coupling change near the edge can be neglected. However, the mutual coupling effect can be quite severe when there are only few elements in the antenna. This is because the active element patterns are severely modified by the mutual coupling and thus differ significantly from one element to the next.

Small phased array antennas are commonly used on small platforms where space is at a premium in the overall structure. For example, a DF antenna must be small yet capable of high resolution and capable of accurate measurements even with the "edge effect." Therefore the study of how such mutual coupling can be controlled is warranted.

B.   OBJECTIVE OF STUDY

The intent of this study is to investigate the ability of two methods to control mutual interference. The first method is to use dummy elements at the edge of the phased array. The second method is to use compensation networks at the inputs of the elements to reject or cancel the interference it receives from other elements.

1

In the first method, the phase differences between the elements in a three-element dipole array are compared with and without parasitic dummy elements at the edges of the array.

In the second method, a hybrid ring is used at the input of each dipole element. It is used to couple some of the voltage generated at the dipole to other dipole elements to influence these input signals such that they give linear phase across the entire antenna.

C.   APPROACH

The two methods of controlling mutual coupling were simulated using commercially available computational electromagnetics (*CEM*) software packages. While other antenna design software packages such as *Patch* and *Ansoft High Frequency Structure Simulator* (*HFSS*) are available, the *Computer Simulation Technology* (*CST*) *Microwave Studio* is chosen to conduct the simulations, due to the ease of use and powerful features offered by it. *Patch* uses the Method of Moments (MoM) while the *HFSS* uses the Finite Element Method (FEM) and both work in the frequency domain. *CST* uses the Finite Integration Technique (FIT) and solves problems in the time domain. Its functionality will be discussed in more detail subsequently.

Extensive simulations were conducted for two aspects of mutual coupling studies. First, a parasitic element is added to each end of a three-element array and the effects on the phases between the active elements are investigated. Next, without parasitic elements, the source is fed through a hybrid ring to the inputs of the dipole. The additional terminal in the hybrid ring can be used to tap off some amount of mutual interference and it is used to adjust the phase of the other dipoles. The ultimate objective of the two methods is to minimize the phase error introduced by the mutual coupling.

The thesis will compare simulated array data for the compensation methods to data for the standard array and explain the results from a quantitative perspective.

D.   OVERVIEW

Chapter II explains the electromagnetic theory and the simulation methods, i.e. the finite integration technique (FIT) used by the *CST* simulation software to compute the electric field at various mesh nodes defined by the user. It also explains how scattering parameters generated by the simulations are used to derive the various voltages and phases at the dipole element inputs.

Chapter III shows the simulation results. The scattering parameters for different antenna configurations are used to generate the element voltage amplitudes and phases. These values will be compared with the theoretical values, and the effects on the element voltage due to adding the dummy elements or the compensation network will be discussed. This chapter also lists the fabrication processes for the dipole antenna with the hybrid ring and the test results are presented. Preliminary experiments on the difference-port signal are also conducted to ascertain that the hybrid ring is a correct candidate for the compensation network.

Chapter IV comments on the results obtained in chapter III.

Chapter V lists future work that can be explored as follow-on research. One possibility is feeding the signal from the isolated arm of the hybrid ring of one dipole to its neighbors to correct the coupling signal, thereby eliminating the phase error between the various dipoles. This will give a good linear phase front for the dipole array.

Chapter VI concludes the findings in the thesis.

THIS PAGE INTENTIONALLY LEFT BLANK

II. THEORY

A. MUTUAL COUPLING

Arrays are the preferred antenna configuration for most radar and electronic warfare (EW) applications. With advancements in solid-state technology, it is possible to realize the feed network required for exciting small antennas with reasonable cost. This allows the concept of lining up many of these small antennas to form a phased array. However, mutual coupling alters [Ref. 8] the voltage phases of the elements on small array elements causing large variations near the edges of the array. The variation in the element currents which are related to the voltage phase at the terminal will subsequently affect the accuracy of the scan angle.

The active element pattern [Ref. 4] is usually used by antenna designers to estimate the element pattern. It works well for large array antennas where most of the elements are away from the edge, but not in the case of a small array antenna, because the element pattern can differ significantly from one element to another. This presents a challenge to have a special network or compensation circuitry to minimize the phase errors between elements, which is an inherent disadvantage of small array antenna structures.

The study of mutual coupling compensation involves interactions between radiation sources. A comprehensive set of formulas that include the mutual coupling requires the full collection of both the near and far fields on and around the structure. For an ideal dipole, the magnetic, $\vec{H}$ and electric fields $\vec{E}$ [Ref. 4] are,

$$\vec{H} = I\frac{\Delta z}{4\pi}(\frac{j\beta}{r}+\frac{1}{r^2})e^{-j\beta\vec{r}}\sin\theta\widehat{\Phi} \text{ and} \tag{1}$$

$$\vec{E} = I\frac{\Delta z}{4\pi}\left[\frac{j\omega\mu}{r}+\sqrt{\frac{\mu}{\varepsilon}}\frac{1}{r^2}+\frac{1}{j\omega\varepsilon r^2}\right]e^{-j\beta\vec{r}}\sin\theta\hat{\theta}+I\frac{\Delta z}{2\pi}\left[\sqrt{\frac{\mu}{\varepsilon}}\frac{1}{r^2}+\frac{1}{j\omega\varepsilon r^3}\right]e^{-j\beta\vec{r}}\cos\theta\hat{r}. \tag{2}$$

5

where Δz is the dipole length along the Z-axis, I the current, ε the permittivity of free space, μ the permeability of free space, $\omega = 2\pi f$, $\beta = \sqrt{\mu\varepsilon}$ and $j = \sqrt{-1}$. The dipole is located at the center of spherical coordinate system (r, θ, ϕ) with unit vectors $(\hat{r}, \hat{\theta}, \hat{\phi})$.

If a complex structure is approximated by a combination of many differential dipoles, it will be necessary to solve the above formulas for all the fields generated by each of these dipoles and combine them to get the final field pattern. In fact, the current will change due to the fields set up by other dipoles. It is obvious that this solution becomes complicated and tedious for the prediction of the mutual coupling, and the computations definitely warrant the use of computers.

Three choices of software are available in the Microwave Laboratory: (1) *Patch* which uses method of moments, (2) *HFSS* which uses finite element method, and (3) *CST Microwave Studio* which uses the finite integration method. This research does not make extensive use of the first two methods however a brief description of each follows.

B.   METHOD OF MOMENTS

In the method of moments calculation [Ref. 8], the starting equation that is used to calculate the electric field is the electric field integral equation (EFIE) [Ref. 1]. This is derived from using Green's function and applying boundary conditions for electric fields. The method of moments represents the current as a series,

$$\vec{J_s} = \sum_n I_n \vec{J_n} \tag{3}$$

and using this in the EFIE and performing a testing procedure gives

$$\vec{E_i}(\vec{r})\big|_{\tan} = \sum_{n=1}^{N} I_n \iint_S \left\{ j\omega\mu \vec{J_n}(\vec{r}')G(\vec{r},\vec{r}') - \frac{j}{\omega\varepsilon}\left[\nabla' \cdot \vec{J_n}(\vec{r}')\right]\nabla'G(\vec{r},\vec{r}') \right\}_{\tan} ds' \tag{4}$$

where $\vec{E_i}$ is the incident field, $\vec{J_n}$ are the expansion functions, and I_n the expansion coefficients.

Selection of the appropriate basis function $\vec{J_n}$ affects accuracy and determines the complexity of the calculations. Once the expansion coefficients are determined, the

current expansion can be used to calculate the radiation field. As it can be seen from the EFIE, obtaining the electric fields at various points in space requires a numerical solution, as it is generally impossible to solve the EFIE in closed form.

C.   FINITE ELEMENTS METHOD

The *HFSS* also uses a weighting method like the method of moments. The basis functions are three dimensional tetrahedrals that segment the whole structure and its surroundings. The method starts with the vector wave equation [Ref. 5],

$$\nabla\times\left(\frac{\nabla\times\vec{E}}{\mu_r}\right)-k_o^2\varepsilon_r\vec{E}=-jk_oZ_o\vec{J}-\nabla\times\left(\frac{\vec{J_m}}{\mu_r}\right) \tag{5}$$

to which the testing procedure is used. Each side is multiplied by a testing (weighting) function, $\vec{W}$ and integrated across the volume domain Ω that encloses the structure

$$\int_{\Omega}\left[\left(\nabla\times\left(\frac{\nabla\times\vec{E}}{\mu_r}\right)-k_o^2\varepsilon_r\vec{E}=-jk_oZ_o\vec{J}-\nabla\times\left(\frac{\vec{J_m}}{\mu_r}\right)\right)\bullet\left(\vec{W}\right)\right]d\Omega$$
$$=\int_{\Omega}\left[\left(-jk_oZ_o\vec{J}-\nabla\times\left(\frac{\vec{J_m}}{\mu_r}\right)\right)\bullet\left(\vec{W}\right)\right]d\Omega. \tag{6}$$

Ideally, both the left hand side and right hand side of the wave equation should be equal and the difference zero. In practice, the difference will not be zero, and therefore has to be minimized. Using Green's first vector identity to eliminate the double curl results in the weak form of the wave equation,

$$\int_{\Omega}\left[\frac{1}{\mu_r}\left(\nabla\times\vec{E}\right)\bullet\left(\nabla\times\vec{W}\right)-k_o^2\varepsilon_r\vec{E}\bullet\vec{W}\right]d\Omega-\oint_{S}\frac{1}{\mu_r}\left(\hat{n}\times\nabla\times\vec{E}\right)\bullet\vec{W}ds+\int_{\Omega}\vec{f_i}\bullet\vec{W}d\Omega=0 \tag{7}$$

where $\vec{f_i}=0$ for scattering problems, but not for antenna problems. The unknown quantity is the electric field, $\vec{E}$. A dual equation can be derived for $\overline{H}$. Both fields are the total fields ($\overline{H}=\overline{H}_i+\overline{H}_s$ and $\vec{E}=\vec{E}_i+\vec{E}_s$). The incident fields are known while the scattered fields are quantities that are to be calculated.

7

In the equation for $\vec{E}$, the integral over the perfect electric conductor (PEC) portions of the tetrahedral surfaces vanish. If the exterior surface of the tetrahedral is not a PEC, then a boundary condition must be imposed.

For any object, a volume surrounding it is discretized into N tetrahedrals, each with N_e edges, the scattered field in each of the tetrahedrals can be expanded into a series of basis functions with unknown expansion coefficients, E_m^e. The field inside tetrahedral e can be expressed as,

$$\vec{E}^e = \sum_{m=1}^{N_e} E_m^e \vec{W}_m^e \quad (e = 1, \ldots, N_e) \tag{8}$$

where the expansion coefficients are determined by solving the matrix equation:

$$\left[A_{mn}^e \right]\left[E_m^e \right] = \left[B_m^e \right] \tag{9}$$

where

$$A_{mn}^e = \int_\Omega \left[\frac{1}{\mu_r}\left(\nabla \times \vec{W}_m^e \right) \bullet \left(\nabla \times \vec{W}_n^e \right) - k_o^2 \varepsilon_r \vec{W}_m^e \bullet \vec{W}_n^e \right] d\Omega \text{ and} \tag{10}$$

$$B_{mn}^e = \oint_{S_d} \frac{1}{\mu_r}\left(\hat{n} \times \nabla \times \vec{E} \right) \bullet \vec{W}_m^e ds - \int_\Omega \left[\nabla \times \left(\frac{1}{\mu_r} \nabla \times \vec{E}_i \right) - k_o^2 \varepsilon_r \vec{E}_i \right] \bullet \vec{W}_m^e d\Omega . \tag{11}$$

D. FINITE INTEGRATION TECHNIQUES

Although *CST* provides both time domain and frequency domain methods to solve antenna problems, only the time domain method will be discussed as the simulations are all conducted using this feature of the package.

The finite integration technique is a Time-Domain Integral Equation (TDIE) approach, solving for the electric and magnetic fields on and around the antenna structure. It calculates the fields at different time steps using the Maxwell's Equations in integral form

$$\oint_{Contour} \vec{E} \bullet d\vec{l} = -\iint_{Area} \frac{\partial \vec{B}}{\partial T} \bullet d\vec{A}, \tag{12}$$

$$\oint_{Contour} \vec{H} \bullet d\vec{l} = \iint_{Area} \left(\frac{\partial \vec{D}}{\partial T} + \vec{J} \right) \bullet d\vec{A}, \tag{13}$$

$$\oiint_{Area} \vec{D} \bullet d\vec{A} = \iiint_{Volume} \rho \bullet dV \text{ and} \tag{14}$$

$$\oiint_{Area} \vec{B} \bullet d\vec{A} = 0. \tag{15}$$

CST first divides the antenna structure and the space around it into boxes. The electric and magnetic fields in each box are computed using the above equations and time stepping. The boxing process is known as meshing and the density of the meshing is based on the number of divisions per wavelength. Each box is known as a grid cell. At every time step, Maxwell's equations are applied on each of the grid cells. A line integration is performed along the rectangular closed-loop path for each face of the grid cell as shown in Figure 1. A surface integration is performed on each face of the grid cell for the closed surface integrals and over the interior of the box for volume integrals.
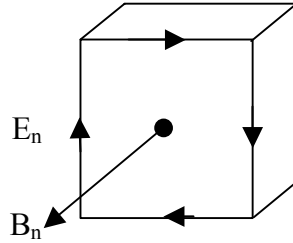
Figure 1.   A Grid Cell

The applied electric fields at the sources are generally *Gaussian* pulses. The process of the calculation within each grid cell commences from the source for transmit mode and at the edges of the bounding box for the receive mode. The *Gaussian* pulse is chosen to ease the Fourier transform process to convert the time domain data into frequency response for presentation. The calculated fields for the current grid cell will be treated as the source cell for the computation of the next grid cell. The process continues until the bounding box declared around the structure has been reached.

For efficient computation, an orthogonal mesh grid based on Cartesian co-ordinates is adopted by *CST*. However, the disadvantage of this meshing method is the deficiency in modeling very complicated three-dimensional cavities, including curved boundaries, with high precision. To overcome this deficiency, *CST* adopts the Perfect Boundary Approximation (PBA) [Ref. 6] method that does not require the computational grids to conform to the rounded boundaries as shown in Figure 2.
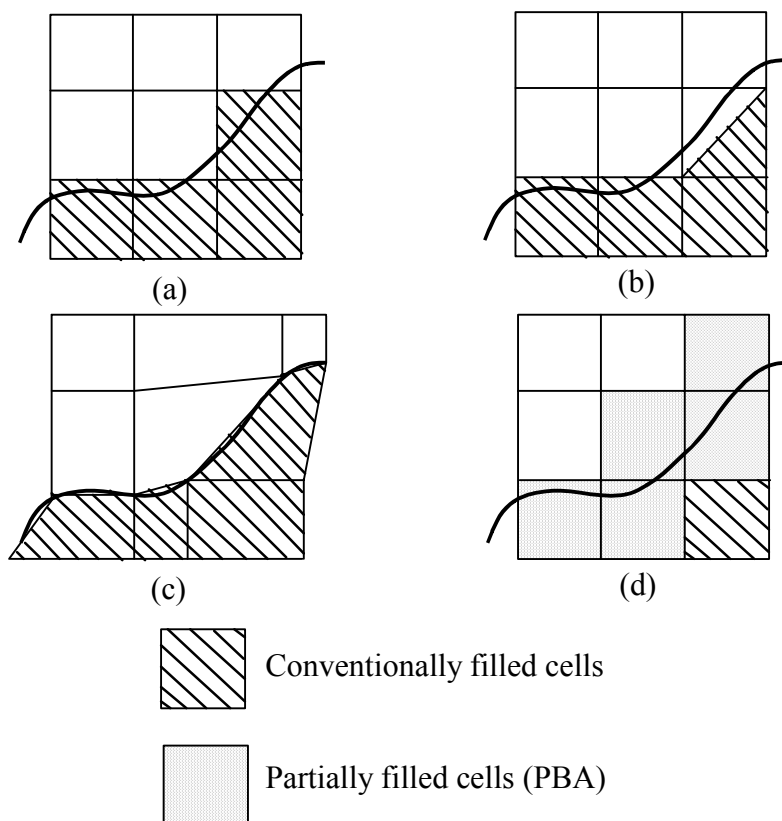
Figure 2.   Grid approximations of rounded boundaries: (a) Standard, (b) Triangular, (c) non-orthogonal, (d) PBA (adopted from Ref. 6)

In conventionally filled cells, the staircase effect limits the accuracy of the calculation. Not only the electric and magnetic fields, but sometimes the global quantities like resonance frequencies and Q-values suffer from modeling errors along curved boundaries. For PBA, sub-cellular information such as the relative permeability of the grid cell is taken into account, leading to an algorithm with higher accuracy for arbitrary shaped boundaries. Furthermore, *CST* also uses automatic meshing. After initial computations, it increases the number of meshes per wavelength at locations where the software deems it will help to increase the accuracy. The automatic meshing is also

10

governed by conditions such as the percentages of material for PBA to declare a grid cell as a perfect conductor, or of other permeability values. Meshing parameters are adjustable but are generally based on user experience.

The *CST version 4.0* also generates scattering parameters, voltage and current magnitudes, and phases in text formats that are readable by Matlab. These files are located in the same directory with the structure files. This allows greater flexibilities for post processing when Matlab is used.

The mutual coupling problem can be approached in two ways: (1) the transmit mode where voltages are applied at each dipole or (2) the receive mode, where a plane wave is incident on the array. Since *CST* generates the scattering parameters for the transmit case, the first approach will be used. The receive mode may not be investigated as it has previously been studied [Ref. 8] but will be mentioned.

E. TRANSMIT MODE – SCATTERING PARAMETERS

The radiation characteristics of an array antenna can be obtained from a knowledge of the properties of each element, the array geometry, and the combined interaction of all elements of the array. The combined mutual interaction of all elements can be obtained from the scattering parameters. Scattering parameters are important when designing microwave circuitry. The scattering matrix of an N-port network generally has the form [Ref. 2],

$$
\begin{bmatrix} V_1^- \\ V_2^- \\ \vdots \\ V_N^- \end{bmatrix} = \begin{bmatrix} S_{11} & S_{12} & \cdots & S_{1N} \\ S_{21} & \ddots & & \vdots \\ \vdots & & \ddots & S_{N-1N} \\ S_{N1} & \cdots & & S_{NN} \end{bmatrix} \begin{bmatrix} V_1^+ \\ V_2^+ \\ \vdots \\ V_N^+ \end{bmatrix}
$$

(16)

or in a more compact form,

$$
\begin{bmatrix} \vec{V}^- \end{bmatrix} = [S] \begin{bmatrix} \vec{V}^+ \end{bmatrix},
$$

(17)

where the minus superscript represents the reflected signal from a port while the plus sign represents the signal injected into the port. The same matrix can be applied to either voltage or current for the N-port network.

Scattering parameters relate the input and output signals at every port and are denoted S_{11} to S_{NN} for N ports. They represent the reflection and transmission coefficients at those ports and it is generally desired to make S_{nn} ($1 \le n \le N$) as small as possible.

Other elements (S_{mn} ($m \ne n$)), in the scattering matrix represent transmission from port n where the signal is injected to port m where the signal is transmitted, while the other ports are terminated with matched loads. The designer determines the distribution of power to ports by setting the respective scattering parameter in the matrix. However, in a phased array, it is desired to reduce (or at least keep constant) all of the S_{mn} ($m \ne n$) since transmission between ports represent mutual coupling.

Whenever waveguide or discrete ports are assigned in a structure, *CST* automatically generates scattering parameters related to these ports. The scattering matrix is then used to generate required voltages which are generally complex, so that the phases of the voltages can be compared to the ideal plane wave linear phase, to produce a phase error at each element.
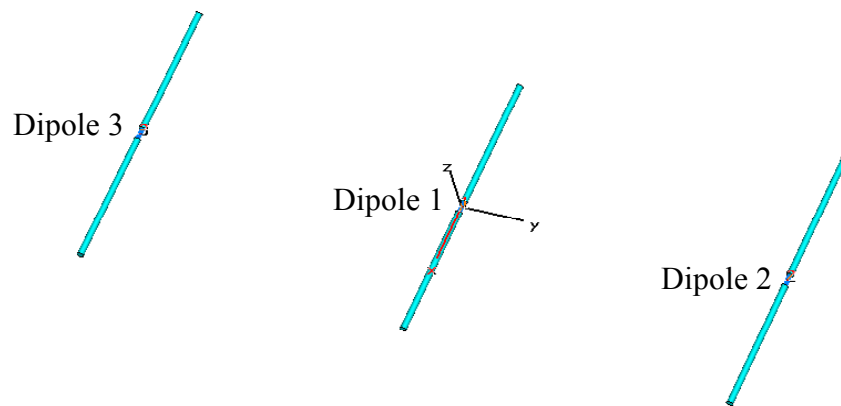
Figure 3.   Dipole naming

The convention in simulations for the dummy element compensation method are shown in Figure 3. With this notation, path differences between adjacent elements in the dipole array are determined, and the effect on the phase of the voltage at the terminals of

each element can be calculated. Adjacent dipoles are named 3-1 and 1-2 pairs for subsequent discussions and the phase difference between two adjacent dipoles will be tied with this convention.
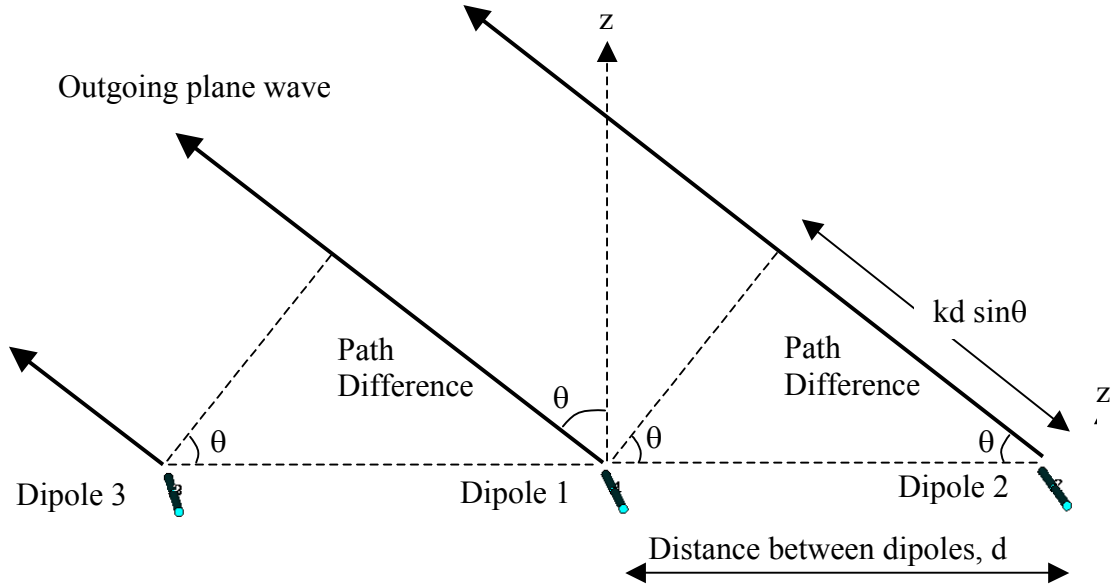
Figure 4.   Phase differences between dipoles

Theoretically, for a scan angle of θ, the path difference (Figure 4) is $d\sin(\theta)$ and the phase difference contributed by this path difference is $kd\sin(\theta)$. Thus, if mutual coupling is omitted, phase difference variations with respect to the array scan angle follows a sine curve.

For voltages impressed on the various dipoles, (or in the receive case, a unity magnitude plane wave incident) the phases are in accordance with the naming convention of the 3 dipoles in Figure 3. Therefore, for the angle θ shown in Figure 4, dipole 3 leads dipole 1 and dipole 1 leads dipole 2 in terms of the excitation phases,

$$
\begin{aligned}
V_1^+ &= 1e^{j0} = 1 \\
V_2^+ &= 1e^{-j\psi_s} \\
V_3^+ &= 1e^{+j\psi_s}
\end{aligned}
\tag{18}
$$

where ψ_s is related to the scan-angle, θ_S of the phased array by $kd \sin(\theta_S)$. The scan angle is selected to be zero along the z-axis to be consistent with the spherical co-ordinate system. At broadside radiation, ψ_s is zero and the path difference between elements will be zero. For other angles, voltages are generally complex to control the beam of the phased array.

The reflected voltages from each of the dipole ports are calculated using scattering parameters that are generated from *CST*:

$$V_1^- = |S_{11}|e^{j\theta_{s11}}V_1^+ + |S_{12}|e^{j\theta_{s12}}V_2^+ + |S_{13}|e^{j\theta_{s13}}V_3^+$$
$$V_2^- = |S_{21}|e^{j\theta_{s21}}V_1^+ + |S_{22}|e^{j\theta_{s22}}V_2^+ + |S_{23}|e^{j\theta_{s23}}V_3^+ \qquad (19)$$
$$V_3^- = |S_{31}|e^{j\theta_{s31}}V_1^+ + |S_{32}|e^{j\theta_{s32}}V_2^+ + |S_{33}|e^{j\theta_{s33}}V_3^+$$

where S_{mn} is represented in polar form as $|S_{mn}|e^{i\theta_{Smn}}$.

The total voltage can then be determined by the addition of both incident and reflected waves. The actual phase and magnitude of the total voltages can then be determined from

$$V_1 = V_1^+ + V_1^-$$
$$V_2 = V_2^+ + V_2^- \qquad (20)$$
$$V_3 = V_3^+ + V_3^-.$$

Once these voltage phases are known, the phase difference between two elements can be calculated and compared with the ideal phase difference as defined by $kd \sin(\theta_S)$. The differences are due to the presence of mutual coupling in the structure and will be examined in later chapters.

F.   RECEIVE MODE – PLANE WAVE

In the receive mode, a plane wave illuminates the array and voltages and currents across element ports are measured. This allows the analysis of differences in the voltage phases between the various dipoles, and the comparison to the ideal linear plane wave phases. It also permits examination of impedance at dipole terminals, via additional post

processing in Matlab. Based on $kd\sin(\theta_S)$, when a plane wave is approaching from broadside, there should be zero phase difference between dipoles.

G.   COMPENSATION METHODS

Two methods of compensation are investigated in this study. The first method adds dummy elements to the sides of the dipole array while the second method adds a compensation circuit to the beam forming network of the dipoles.

1.   Dummy Elements Compensation Method

The dummy element method places a dummy at the each end of the array. Due to the fields from the active elements, currents induced on the dummies will radiate fields back to active elements. With dummies present, edge elements in the array will hopefully experience nearly the same environment as those elements further way from the ends. This modification will reduce the edge effect, producing an active element pattern at the edge elements that is similar to that of elements away from the edges.

To quantify this method, one compares voltages between two types of arrays; one with a large number of elements and the other with three active and two dummy elements. Voltages at various terminals of the large array are expressed in terms of mutual impedances. N is assumed to be odd in the present analysis. The voltages at the N elements are related to the currents by the following matrix:

$$
\begin{bmatrix}
V_1 \\
V_2 \\
V_3 \\
\vdots \\
V_{\frac{N-1}{2}} \\
V_{\frac{N-1}{2}+1} \\
V_{\frac{N-1}{2}+1} \\
\vdots \\
V_{N-1} \\
V_N
\end{bmatrix}
=
\begin{bmatrix}
I_1 Z_{11} & + & I_2 Z_{12} & + & I_3 Z_{13} & +\cdots+ & I_{N-1} Z_{1,N-1} & + & I_N Z_{1N} \\
I_1 Z_{21} & + & I_2 Z_{22} & + & I_3 Z_{23} & +\cdots+ & I_{N-1} Z_{2,N-1} & + & I_N Z_{2N} \\
I_1 Z_{31} & + & I_2 Z_{32} & + & I_3 Z_{33} & +\cdots+ & I_{N-1} Z_{3,N-1} & + & I_N Z_{3N} \\
\vdots & \cdots & \vdots & \cdots & \vdots & \cdots & \vdots & \cdots & \vdots \\
I_1 Z_{\frac{N-1}{2},1} & + & I_2 Z_{\frac{N-1}{2},2} & + & I_3 Z_{\frac{N-1}{2},3} & +\cdots+ & I_{N-1} Z_{\frac{N-1}{2},N-1} & + & I_N Z_{\frac{N-1}{2},N} \\
I_1 Z_{\frac{N-1}{2}+1,1} & + & I_2 Z_{\frac{N-1}{2}+1,2} & + & I_3 Z_{\frac{N-1}{2}+1,3} & +\cdots+ & I_{N-1} Z_{\frac{N-1}{2}+1,N-1} & + & I_N Z_{\frac{N-1}{2}+1,N} \\
I_1 Z_{\frac{N-1}{2}+2,1} & + & I_2 Z_{\frac{N-1}{2}+2,2} & + & I_3 Z_{\frac{N-1}{2}+2,3} & +\cdots+ & I_{N-1} Z_{\frac{N-1}{2}+2,N-1} & + & I_N Z_{\frac{N-1}{2}+2,N} \\
\vdots & \cdots & \vdots & \cdots & \vdots & \cdots & \vdots & \cdots & \vdots \\
I_1 Z_{N-1,1} & + & I_2 Z_{N-1,2} & + & I_3 Z_{N-1,3} & +\cdots+ & I_{N-1} Z_{N-1,N-1} & + & I_N Z_{N-1,N} \\
I_1 Z_{N,1} & + & I_2 Z_{N,2} & + & I_3 Z_{N,3} & +\cdots+ & I_{N-1} Z_{N,N-1} & + & I_N Z_{NN}
\end{bmatrix}
$$

$$(21)$$

The voltages at the three elements in the center of the large array are

$$
\begin{bmatrix}
V_{\frac{N-1}{2}} \\
V_{\frac{N-1}{2}+1} \\
V_{\frac{N-1}{2}+1}
\end{bmatrix}
=
\begin{bmatrix}
V_{\frac{N-1}{2}+1} & +\cdots+ & I_{\frac{N-1}{2}} Z_{\frac{N-1}{2},\frac{N-1}{2}} & + & I_{\frac{N-1}{2}+1} Z_{\frac{N-1}{2},\frac{N-1}{2}+1} & + & I_{\frac{N-1}{2}+2} Z_{\frac{N-1}{2},\frac{N-1}{2}+2} & +\cdots+ & I_N Z_{\frac{N-1}{2},N} \\
I_1 Z_{\frac{N-1}{2}+1,1} & +\cdots+ & I_{\frac{N-1}{2}} Z_{\frac{N-1}{2}+1,\frac{N-1}{2}} & + & I_{\frac{N-1}{2}+1} Z_{\frac{N-1}{2}+1,\frac{N-1}{2}+1} & + & I_{\frac{N-1}{2}+2} Z_{\frac{N-1}{2}+1,\frac{N-1}{2}+2} & +\cdots+ & I_N Z_{\frac{N-1}{2}+1,N} \\
I_1 Z_{\frac{N-1}{2}+2,1} & +\cdots+ & I_{\frac{N-1}{2}} Z_{\frac{N-1}{2}+2,\frac{N-1}{2}} & + & I_{\frac{N-1}{2}+1} Z_{\frac{N-1}{2}+2,\frac{N-1}{2}+1} & + & I_{\frac{N-1}{2}+2} Z_{\frac{N-1}{2}+2,\frac{N-1}{2}+2} & +\cdots+ & I_N Z_{\frac{N-1}{2}+2,N}
\end{bmatrix}.
$$

$$(22)$$

The goal of the three-element array with dummies is to achieve voltages similar to those of the three elements in the center of the large array or,

$$
\begin{bmatrix}
V_1 \\
V_2 \\
V_3
\end{bmatrix}
=
\begin{bmatrix}
I_{\frac{N-1}{2}} Z_{\frac{N-1}{2},\frac{N-1}{2}} & + & I_{\frac{N-1}{2}+1} Z_{\frac{N-1}{2},\frac{N-1}{2}+1} & + & I_{\frac{N-1}{2}+2} Z_{\frac{N-1}{2},\frac{N-1}{2}+2} \\
I_{\frac{N-1}{2}} Z_{\frac{N-1}{2}+1,\frac{N-1}{2}} & + & I_{\frac{N-1}{2}+1} Z_{\frac{N-1}{2}+1,\frac{N-1}{2}+1} & + & I_{\frac{N-1}{2}+2} Z_{\frac{N-1}{2}+1,\frac{N-1}{2}+2} \\
I_{\frac{N-1}{2}} Z_{\frac{N-1}{2}+2,\frac{N-1}{2}} & + & I_{\frac{N-1}{2}+1} Z_{\frac{N-1}{2}+2,\frac{N-1}{2}+1} & + & I_{\frac{N-1}{2}+2} Z_{\frac{N-1}{2}+2,\frac{N-1}{2}+2}
\end{bmatrix}.
$$

$$(23)$$

The dummies must generate the following compensation terms in each of the active elements in the three-element array in order to make it perform like an infinite array:

$$\begin{bmatrix} V_{d1} \\ V_{d2} \\ V_{d3} \end{bmatrix} = \begin{bmatrix} I_1 V_{\frac{N-1}{2}+1} & +\cdots+ & I_{\frac{N-1}{2}-1} Z_{\frac{N-1}{2},\frac{N-1}{2}-1} & + & I_{\frac{N-1}{2}+3} Z_{\frac{N-1}{2},\frac{N-1}{2}+3} & +\cdots+ & I_N Z_{\frac{N-1}{2},N} \\ I_1 Z_{\frac{N-1}{2}+1,1} & +\cdots+ & I_{\frac{N-1}{2}-1} Z_{\frac{N-1}{2}+1,\frac{N-1}{2}-1} & + & I_{\frac{N-1}{2}+3} Z_{\frac{N-1}{2}+1,\frac{N-1}{2}+3} & +\cdots+ & I_N Z_{\frac{N-1}{2}+1,N} \\ I_1 Z_{\frac{N-1}{2}+2,1} & +\cdots+ & I_{\frac{N-1}{2}-1} Z_{\frac{N-1}{2}+2,\frac{N-1}{2}-1} & + & I_{\frac{N-1}{2}+3} Z_{\frac{N-1}{2}+2,\frac{N-1}{2}+3} & +\cdots+ & I_N Z_{\frac{N-1}{2}+2,N} \end{bmatrix},$$

$$(24)$$

where V_{dm} ($m = 1,2,3$) represent additional voltages that the dummy must contribute to the respective port voltages.

Formulating equivalent voltage magnitudes and phases contributed by dummies requires either physical measurements to obtain the Z-matrix elements and currents or, computational determination of the impedance elements. In this study, the computational approach is adopted.

Without mutual coupling, the phase difference between two dipole elements spaced a half-wavelength apart, plotted against the scan angle, follows a sine curve. The actual phase difference of a three-element array fluctuates around the sine curve. With dummies, the phase differences are obtained from simulations and compared to the case without mutual interference. Variations are made to the dummy physical parameters such as length, separation from the last active element of the array, and terminating loads. These comparisons give a good indication of variation or combinations of variations that will help minimize the phase error induced due to mutual coupling.

2. Compensation Network

The compensation network concept uses feedback circuits connected from one dipole to the others to "inform" them how much mutual coupling it is experiencing. Receiving the information, the dipoles will adjust their voltages to reduce the phase error due to mutual coupling. This is a type of cancellation where signals are coupled from each element and used to cancel free space coupling.
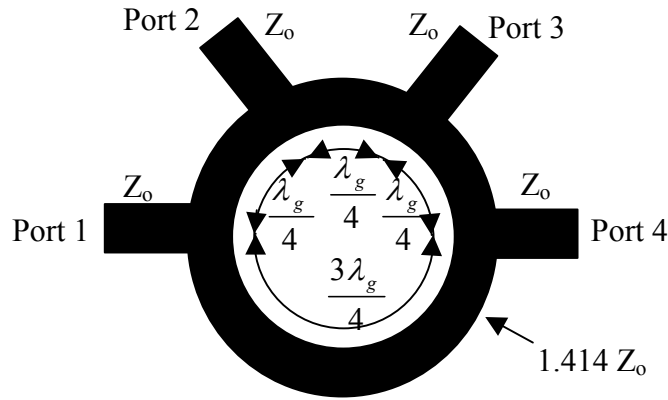
Figure 5.   Hybrid ring

The approach investigated in this study is to build dipole elements and simulate various compensation network configurations to check their effectiveness. The initial design of a single dipole with a second port for connection to a compensation network was done using *CST*. The compensation element is comprised of a microstrip hybrid ring connected to the dipole terminals, forming a 2-port dipole. A typical hybrid ring is shown in Figure 5. Note that λ_g (wavelength in the microstrip guide) depends on permittivity, which is dependent on the substrate type.

An input signal at port 1 will split and propagate in both directions, thereby creating a standing wave pattern in the transmission-line ring. A voltage null exists at port 3 since the difference in path lengths causes the two waves to arrive at that point 180° out-of-phase. The signal at port 2 and port 4 are also 180° out-of-phase. When the phase of the signal between port 2 and port 4 differs from 180°, it will produce a voltage at port 3. An example of 5° difference between the inputs at port 2 and 4 is shown in the Figure 6. The port that generates the difference voltage is commonly known as the difference-port.
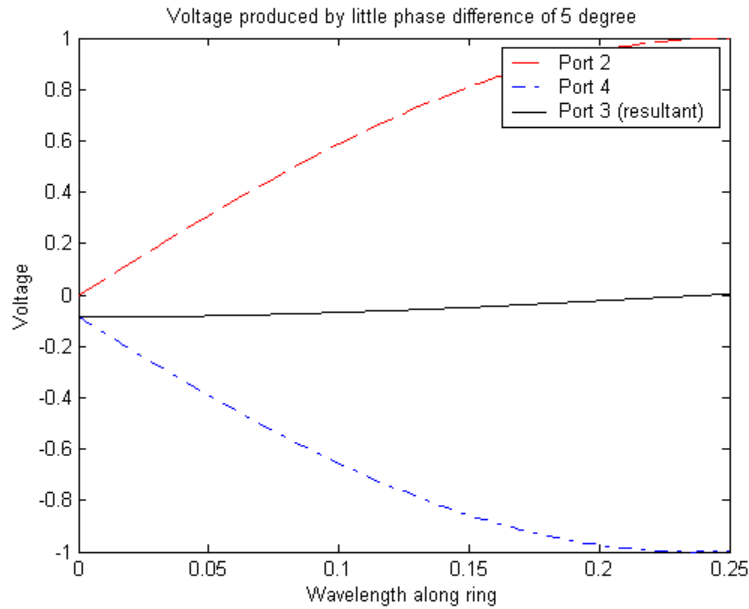
Figure 6.   Phase generated at port 3 due to phase difference between 2 and 4

The phase for 0° scan is introduced by the mutual coupling from nearby dipoles. A larger phase difference will generate a larger voltage output at port 3. This generated signal can then be fed back to other dipoles to indicate the amount of phase difference experienced.

The 180° out-of-phase signal fed to the two arms of the dipole is required for operation in the resonant mode, and both ports 2 and 4 naturally provide this for input to port 1. A typical arrangement for the connection between the dipole arms and the hybrid arm is shown in Figure 7.
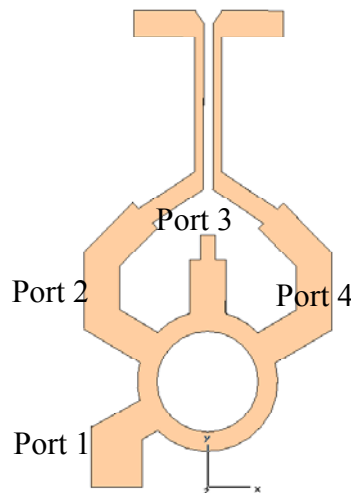
Figure 7.   Dipole connected with a hybrid ring

19

The single dipole element with its compensation network was designed in *CST* to determine if all lines are matched and to ensure that it has low reflection coefficients at the ports.

Once individual dipoles are tested and deemed working at the desired frequency with low reflection coefficients at the ports, they can be connected in various configurations to check the effectiveness of the compensation networks. One possible compensation network is shown in Figure 8. Weights can be adjusted along with phase shifters to provide compensation as the beam scans. More circuit configurations are presented in Chapter V.
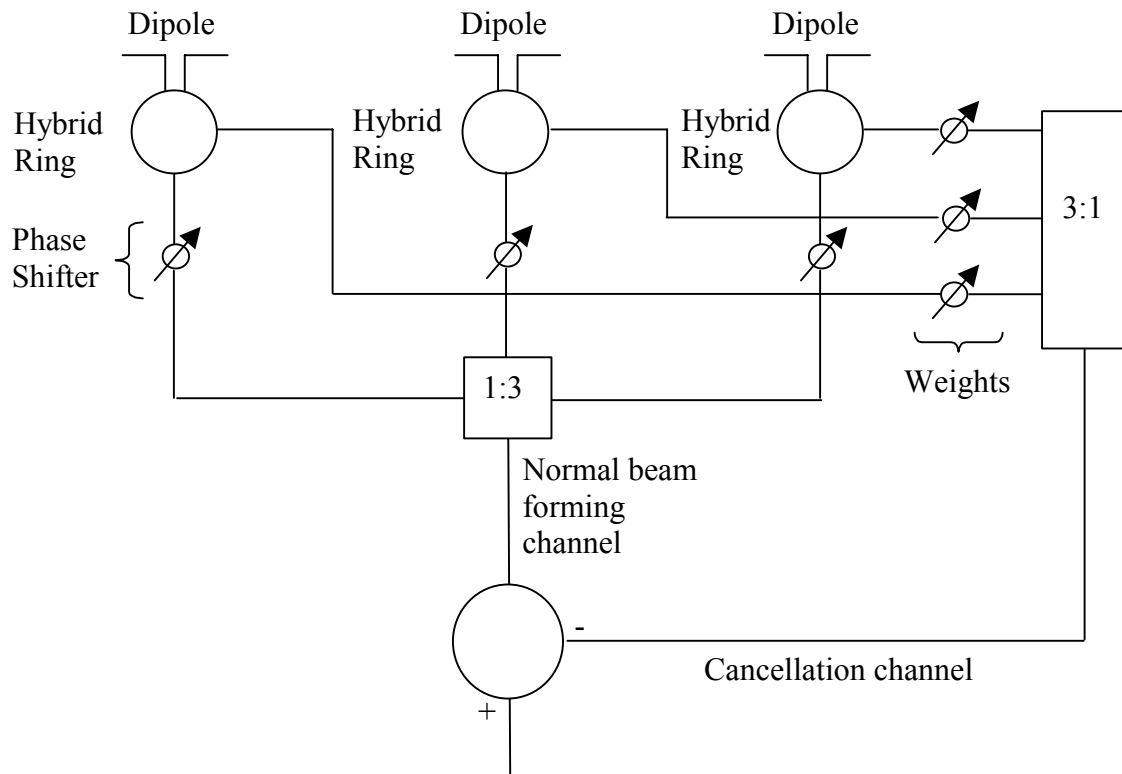
Figure 8.   A three-element array with possible compensation network for both transmit and receive scenarios

III. SIMULATIONS AND RESULTS, FABRICATIONS AND TESTINGS

A. SIMULATION SETTINGS

1. Dummy Elements Compensation Method

A three-element array with the dummies is shown in Figure 9. The length of the active and dummy dipole elements is $0.45\lambda_o$ (λ_o is the free space wavelength). The active dipole elements are spaced $0.5\lambda_o$ apart. They are driven by a $70\,\Omega$ source while the dummy elements are terminated in passive loads. The dipoles and dummies are located $0.25\lambda_o$ above an infinite ground plane. In the simulations, dummy separations vary between $0.3\lambda_o$ and $0.7\lambda_o$ in steps of $0.025\lambda_o$ and variation of the dummy length between $0.35\lambda_o$ and $0.7\lambda_o$ in steps of $0.05\lambda_o$. The load value is also varied between 1 and $100,000\,\Omega$. Complex loads are also used for simulations and the values are $j4,000\,\Omega$ and $-j4,000\,\Omega$ to represent inductive and capacitive situations respectively. For each simulation, the scattering parameters are recorded for computing voltage magnitude and phases.
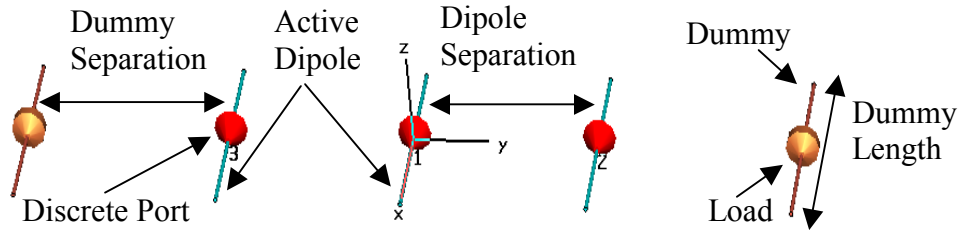
Figure 9.   Setup for three-element array with dummies

Two quantities of phase difference will be referred to regularly during the comparisons. The phase difference between active dipole 3 and dipole 1 is referred to as 3-1 while the difference between active dipole 1 and dipole 2 is 1-2. The definition of phase difference means the subtraction of the phase of the latter dipole from the first. Recall that the final phases of the voltage at the source port are calculated from the scattering parameters generated from *CST* and these are dependent on $kd\sin(\theta_s)$, where θ_s is the array scan angle desired, as in Equation (20).

2. Compensation Network Method

The compensation network method uses a different concept from the dummy element compensation method. It attempts to modify the phase of signals of the dipoles. The modification is dependent on the amount of mutual coupling experienced from other dipole elements. More explanation is provided in the next section.

B. RESULTS – DUMMY ELEMENTS COMPENSATION METHOD

1. Baseline: Three-Dipole Array

The phases between dipoles are calculated using scattering parameters obtained from *CST* simulations. The phase of dipole 3 leads dipole 1, which in turn leads that of dipole 2. In Figure 10, both green and red curves should be greater than zero but mutual coupling causes the red curve at small scan angles to lag theoretical values. This is consistent with [Ref. 8] previous findings. Additional phase differences are plotted in Figure 11 and it is a very convenient way to present how much improvement a particular type of compensation has achieved.
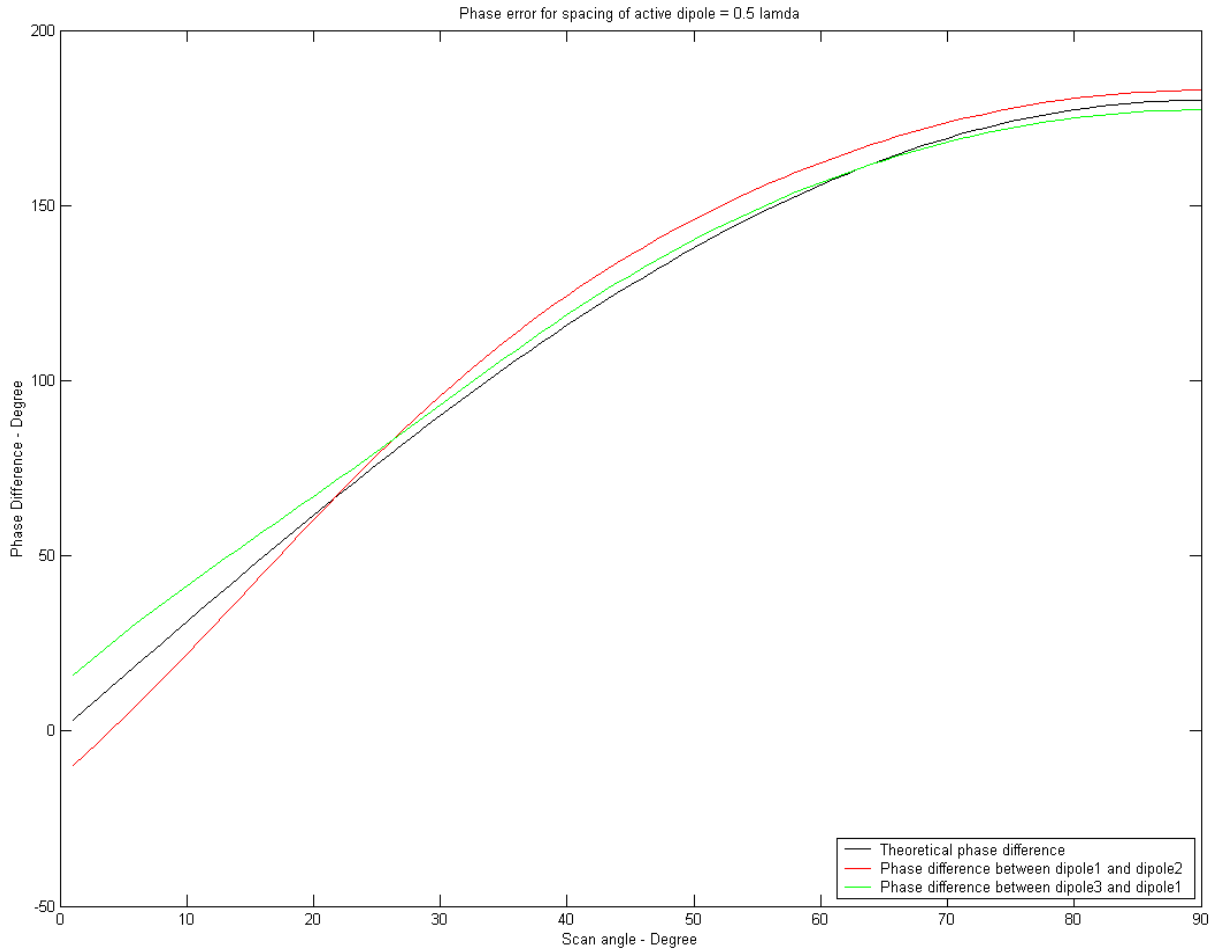
Figure 10.   Resultant phases versus theoretical phase

2.   Load Value Variations

When a half-wave dipole resonates, it has an input impedance of about $70\,\Omega$ which is the basis for load variations. The load attached to a dummy element is varied in steps of $70\,\Omega$ and a $100{,}000\,\Omega$ to simulate an open circuit at the dipole terminal. The values used are 1, 70, 140 and $100{,}000\,\Omega$. The $100{,}000\,\Omega$ attempts to emulate a near open circuit dummy. Simulation results are shown in Appendix A. A summary of the graphs follows.
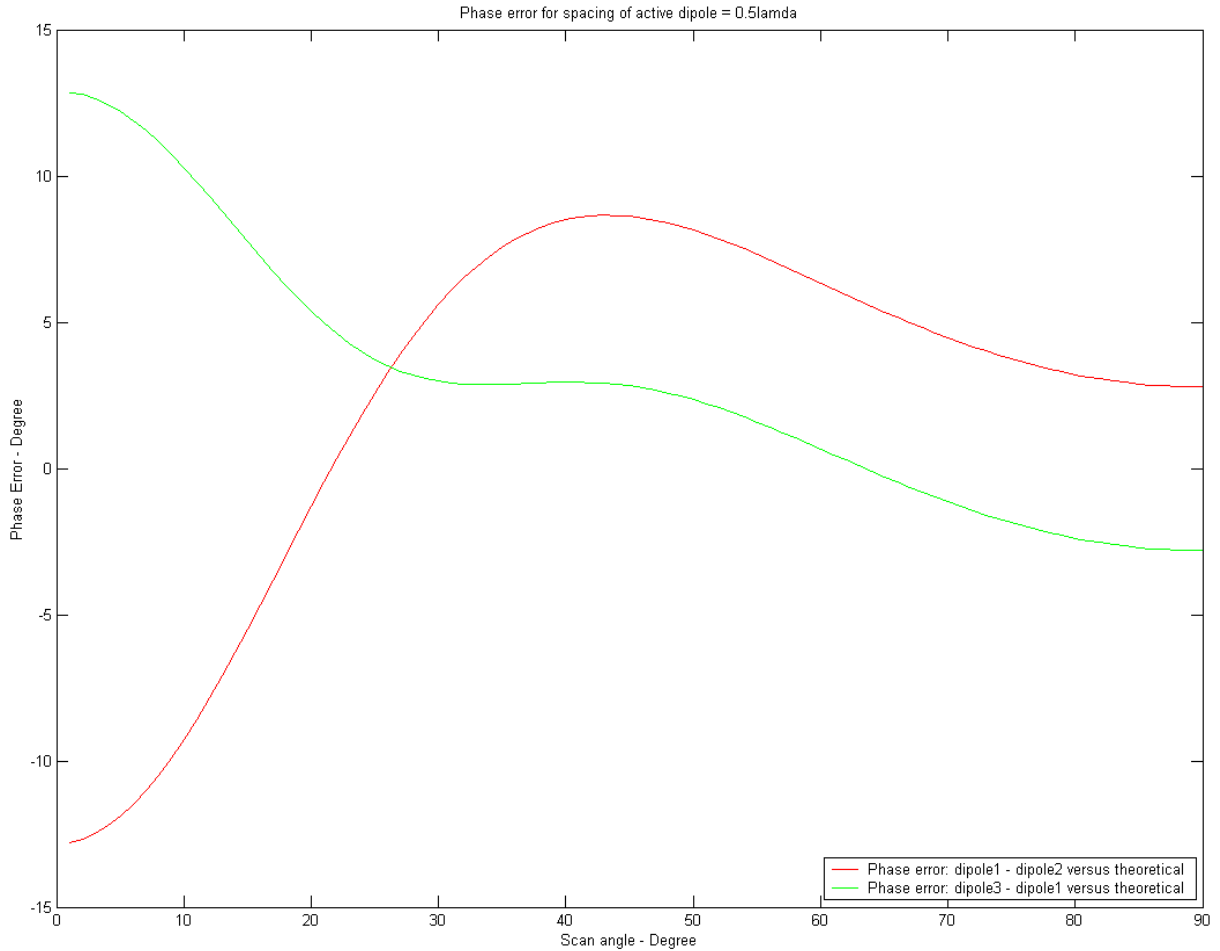
Figure 11.   Additional phase error due to mutual coupling

a.   *Low Scan Angle (Below 25°)*

Initially, the phase error appears smaller for the $100,000\,\Omega$ case if the dummies are placed nearer to the last active array elements. Simulations for this load value are then conducted for dummy separations between $0.1\,\lambda_o$ and $0.275\,\lambda_o$. The additional result is shown in Figure 12 for a dummy separation of $0.1\,\lambda_o$. The phase difference does not improve even when the dummy separation is reduced. The best achievable phase difference is 8° at the broadside scan angle.
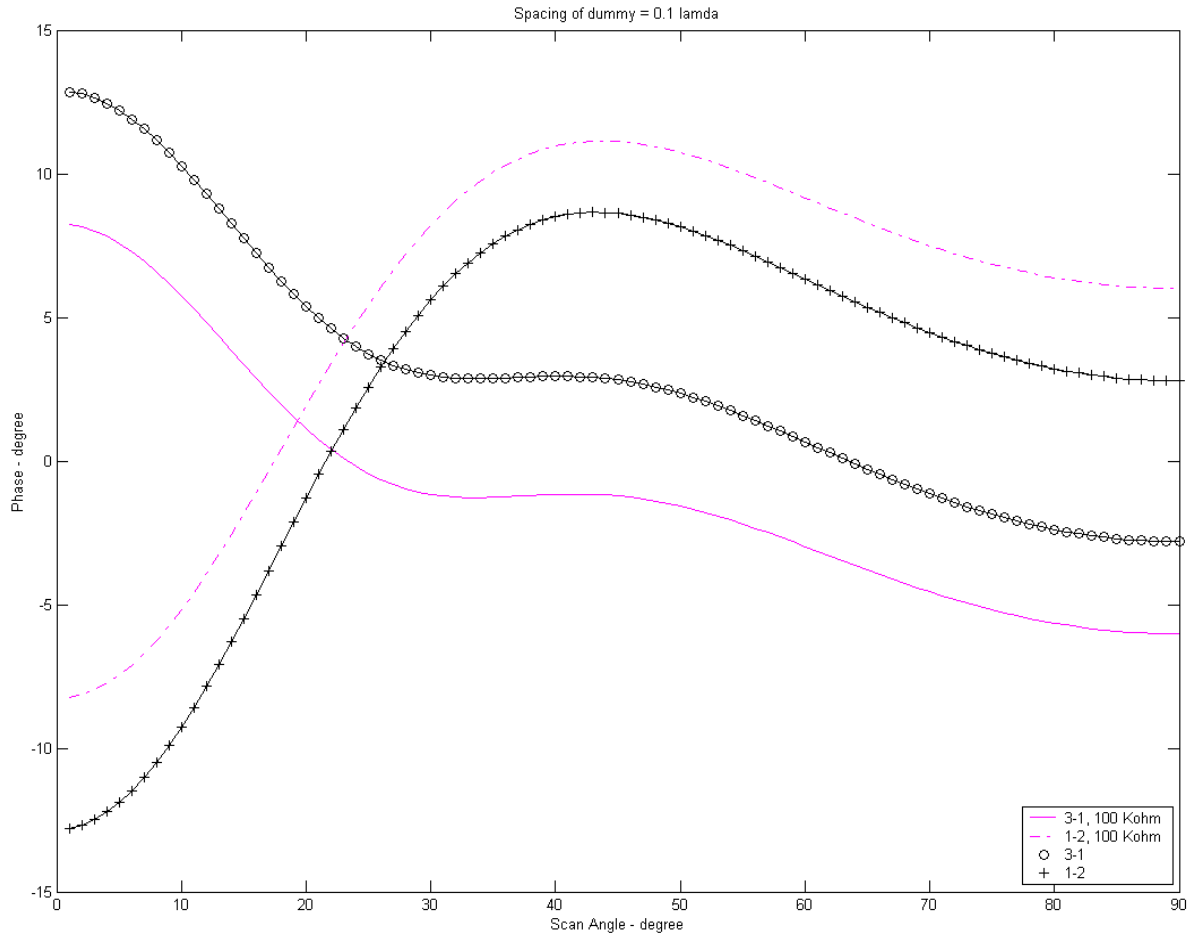
Figure 12. $100,000\,\Omega$ at closer dummy separation

The plot corresponding to dummy separation $0.6\,\lambda_o$ is extracted from Appendix A and presented in Figure 13. With the smallest load, the phase differences improve significantly when the dummy separation is between $0.475\,\lambda_o$ to $0.625\,\lambda_o$ before it degrades. The lowest possible phase difference in the low scan angle region is about $8°$ and is achieved at $0.6\,\lambda_o$ dummy separation with a $1\,\Omega$ load terminating the dummies. The phase difference achieved after compensation is about $8°$ at broadside compared to $13°$ in the uncompensated case.
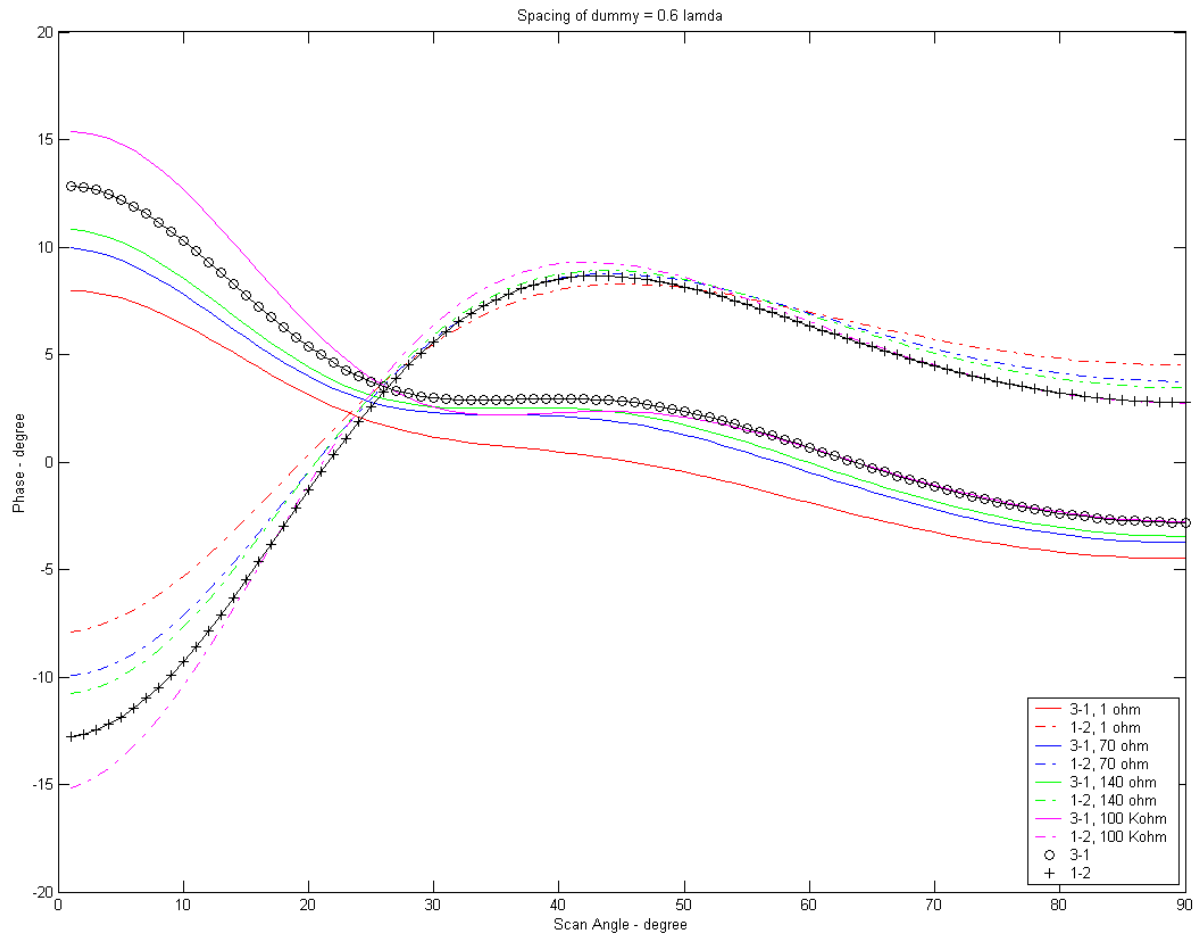
Figure 13.   Best phase difference (low scan angle)

b.   *Medium Scan Angle (25° to 60°)*

In the medium scan angle range, the uncompensated case has a phase difference of less than 8° for the 1-2 dipole pair and less than 3° for the 3-1 dipole pair. Between $0.375 \lambda_o$ to $0.475 \lambda_o$ dummy separation, the $100,000 \, \Omega$ case produces the least phase differences and best compensation for the 3-1 dipole pair. However, it deteriorates as the dummy separation is increased while other load values improve and provide lesser phase difference. For the 1-2 dipole pair, the $1 \, \Omega$ case produces the largest phase difference at about 45° scan angle while the $100,000 \, \Omega$ case produces the least phase differences. Smaller dummy separations also result in smaller phase differences. As the dummy separation is increased, the phase differences also increase, and worsen with the $100,000 \, \Omega$ case deteriorating most. However, beyond a dummy separation of $0.6 \lambda_o$, the

26

phase difference for $1\,\Omega$ is better than the uncompensated case and the improvement continues as the dummy separation is further increased.

c.   *Large Scan Angle (Above 60°)*

The phase differences for all dummy separations and load terminations do not offer much improvement, compared to the uncompensated case, at large dummy separations.   At $0.3\,\lambda_o$ dummy separation, all phase differences are less than 4° but increase as the dummy separation increases, a case worse than the uncompensated case.

3.   Dummy Length Variations

From Appendix A, it is observed that significant phase difference improvements occur when the dummy separation is between $0.45\,\lambda_o$ to $0.65\,\lambda_o$ and the load is terminated with $1\,\Omega$.   With this interval and a short circuit load, the dummy element length is now varied to check if further improvements can be achieved.   The length is varied between $0.35\,\lambda_o$ and $0.7\,\lambda_o$ in steps of $0.5\,\lambda_o$.   The plots are presented in Appendix B.   Similarly, there are 3 regions to consider because the phase difference responds differently to the scan angles.

a.   *Low Scan Angle (Below 25°)*

It is observed that a dummy element length of $0.45\,\lambda_o$ produces the least phase difference while the shortest dummy element produces the most phase difference. All other dummy element lengths produce phase differences that are larger than the $0.45\,\lambda_o$ situation.   Therefore, it can be deduced that a dummy element that has the same dimension as the active dipole elements produces the best compensation at this scan angle range.   However, the dummy length dimension does not further improve the phase difference, i.e. it remains at the best achievable compensation attained in Appendix A. As such, as long as one chooses the length of the dummy length to be same as the active elements, it should produce the best compensation.

A plot at $0.55\,\lambda_o$ dummy separation is shown in Figure 14. It can be seen that dummy lengths that are longer or shorter than the active element length will have large phase difference compared to the $0.45\,\lambda_o$ (green curve) dummy element length.
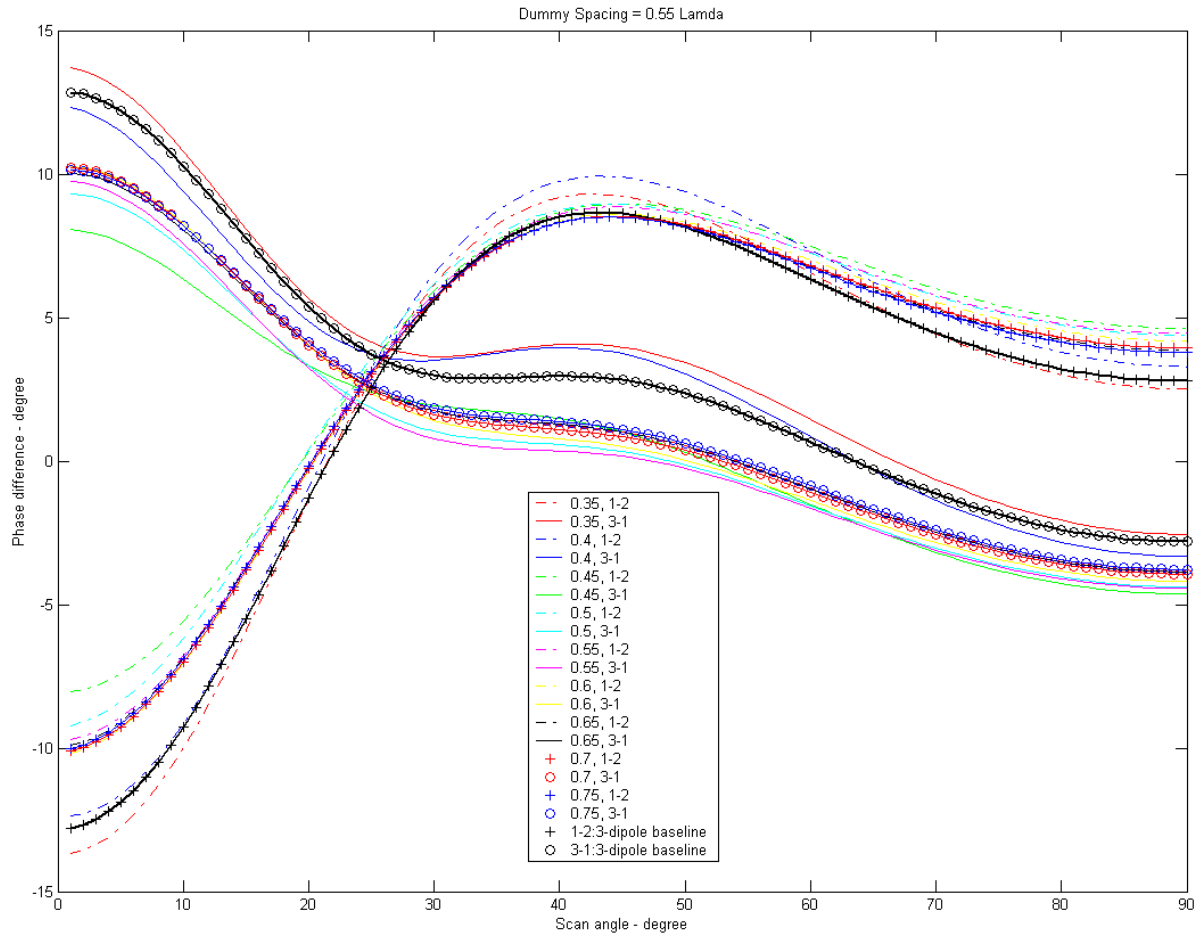

Figure 14.   Dummy length variation: $0.55\,\lambda_o$

When the dummy separation is varied, the best phase difference is still achieved by a dummy length of $0.45\,\lambda_o$. The plot for the largest dummy separation of $0.65\,\lambda_o$ is shown in Figure 15 and shows this phenomenon. Similarly all other plots in the appendix follow the same trend.
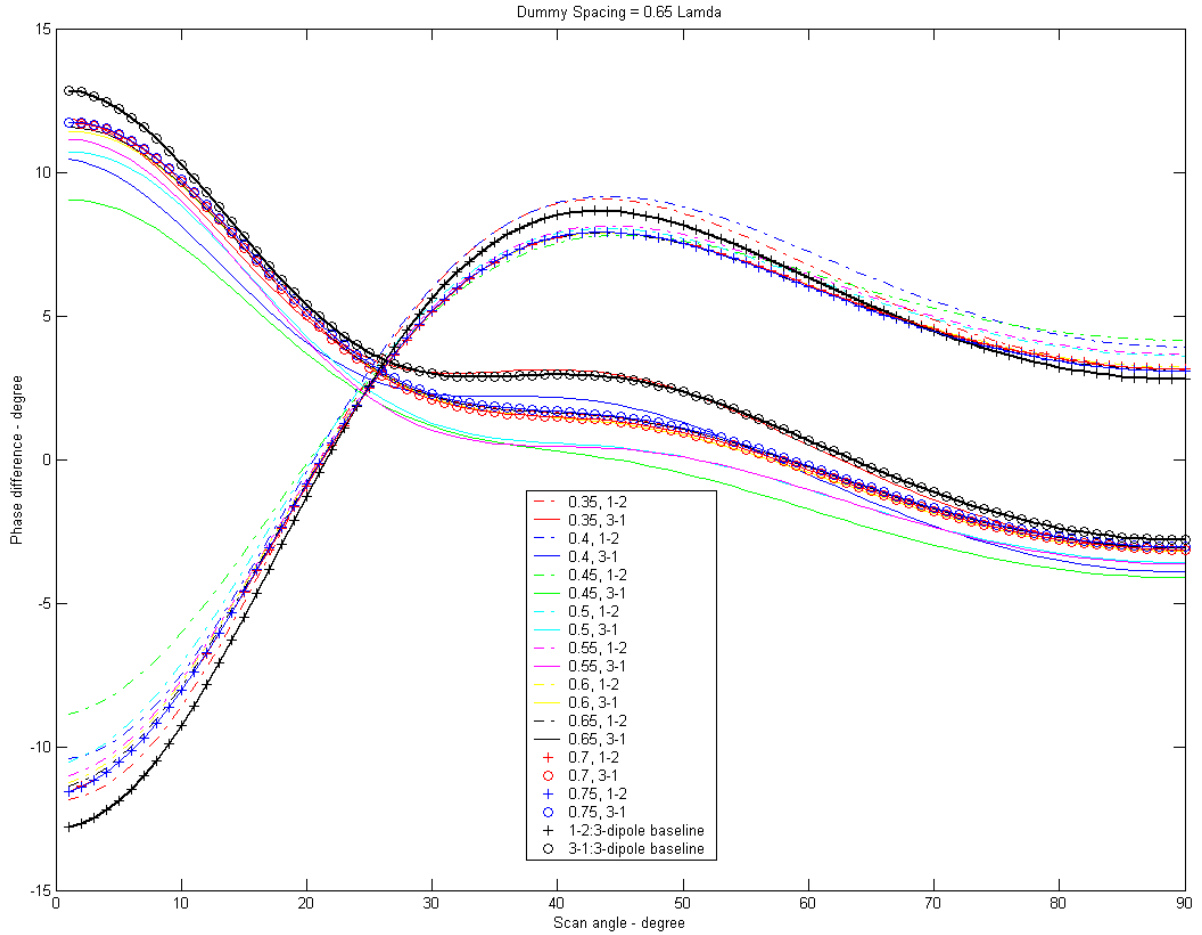
Figure 15.   Dummy length variation: $0.65\,\lambda_o$

b.   *Medium Scan Angle (Between 25° to 60°)*

The phase differences in the 3-1 dipole pair generally have a value of less than 5°, like the uncompensated case. When the dummy separation is increased from $0.45\,\lambda_o$ to $0.65\,\lambda_o$, the relative differences between various dummy lengths and the uncompensated case do not change as much as when the dummy length is $0.45\,\lambda_o$. In the 1-2 dipole pair case, the phase differences actually get worse compared to the uncompensated case.

c.   *Large Scan Angle (Above 60°)*

The compensated case generally provides worse phase difference except when the dummy length is $0.35\,\lambda_o$ or $0.4\,\lambda_o$.

29
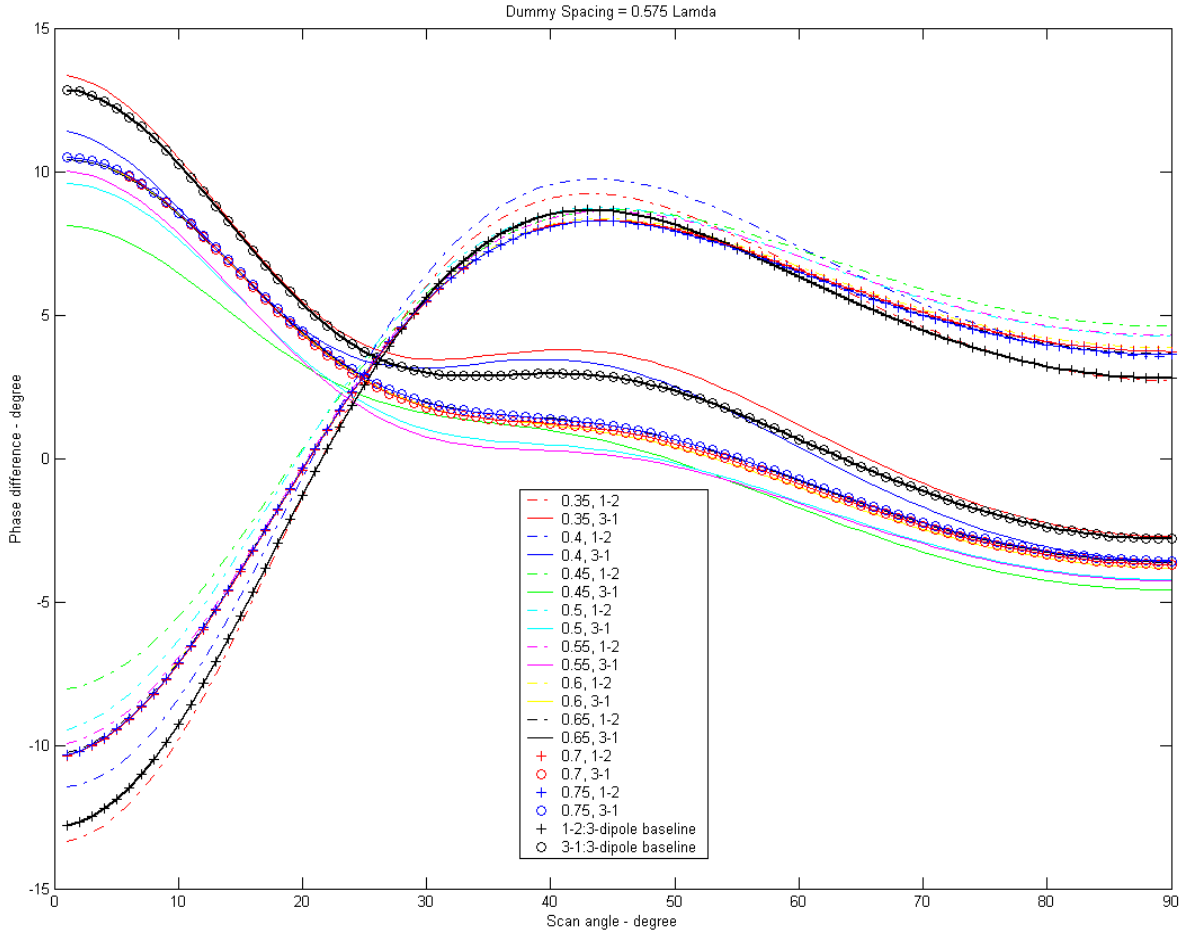
Figure 16.   Dummy length variation: $0.575\,\lambda_o$

4.   Complex Load

The phase differences obtained by varying dummy separations with complex load terminated at the dummy elements are shown in Appendix C. It can be seen that the phase difference for inductive load is larger than the uncompensated case at small scan angles and at larger scan angles, the phase differences are just as bad as for the uncompensated cases. The plots coincide with each other regardless of the values of inductor reactance. For the capacitive cases, smaller capacitance brings the plot nearer to the $1\,\Omega$ case which means it is redundant. Therefore, it can be seen that a complex load is not suitable for the dummy element compensation method.

C.   RESULTS – COMPENSATION NETWORK METHOD

In the compensation method, the interfacing ports are designed with $50\,\Omega$ characteristic impedances in order to match to commercially available connectors and cables. Therefore, the hybrid ring arms adopt this characteristic impedance. The dipole has been designed with a $100\,\Omega$ terminal impedance and a quarter–wavelength transformer is needed to match the two impedances. The quarter-wavelength transformer impedance is calculated to be $70\,\Omega$. The dipole arms are placed at $0.15\,\lambda_o$ instead of $0.25\,\lambda_o$ above the ground plane due to the presence of the printed circuit board's substrate. The connectors at the ports match RG141/U coaxial cable specifications.

The printed circuit board has a relative permittivity of 3.38 and a thickness of 60 mils. Table 1 shows the thickness of the strips and its waveguide wavelength on the printed circuit board designed at 7.5 GHz.

Characteristics Impedance, (Ω)	Line Width, (mils)	Microstrip Wavelength, λ_g (mils)
50	138.93	964.02
70.71	76.26	984.58
100	35.715	1006.4

Table 1.   Line characteristics for microstrips

The compensation network method uses passive circuits and a hybrid ring to connect to the terminals of the dipoles for phase correction in order to reduce the mutual coupling. The hybrid ring forms part of the feed network and has been fabricated onto the printed circuit board where the dipole element is located. Microstrips are used for the frequency of interest at 7.5 GHz and resulting in a very compact structure. The following sections describe the design and fabrication of the dipole element.

1.   Stripline Feedthrough Design

The stripline used for the dipole is shown in Figure 17. The substrate is 60 mils thick with a relative permittivity of 3.38. The thickness of the ground plane and stripline is 2 mils. The use of thick ground plane in the simulation will not affect the results. In fact, it simplifies the drawing of the co-axial cable that is required at port 2, whose its

dielectric is ultimately embedded in an outer conductor sleeve (port 2 is on the bottom and not visible in the figure).

The stripline feedthrough attains a low reflection coefficient of less than –30 dB and good transmission between ports 1 and 2 with near zero attenuation, as indicated by the scattering parameters in Figure 18.
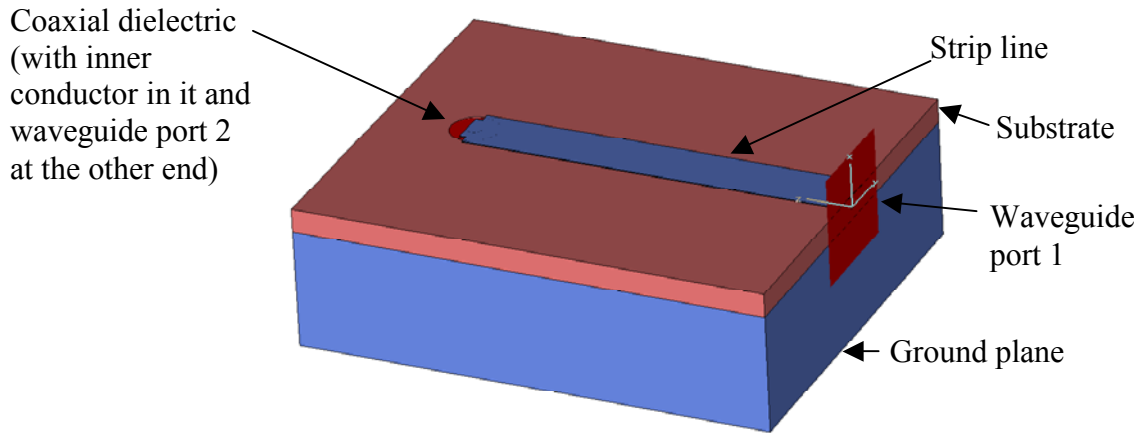

Figure 17.   Stripline feedthrough (a transition from coaxial to microstrip)
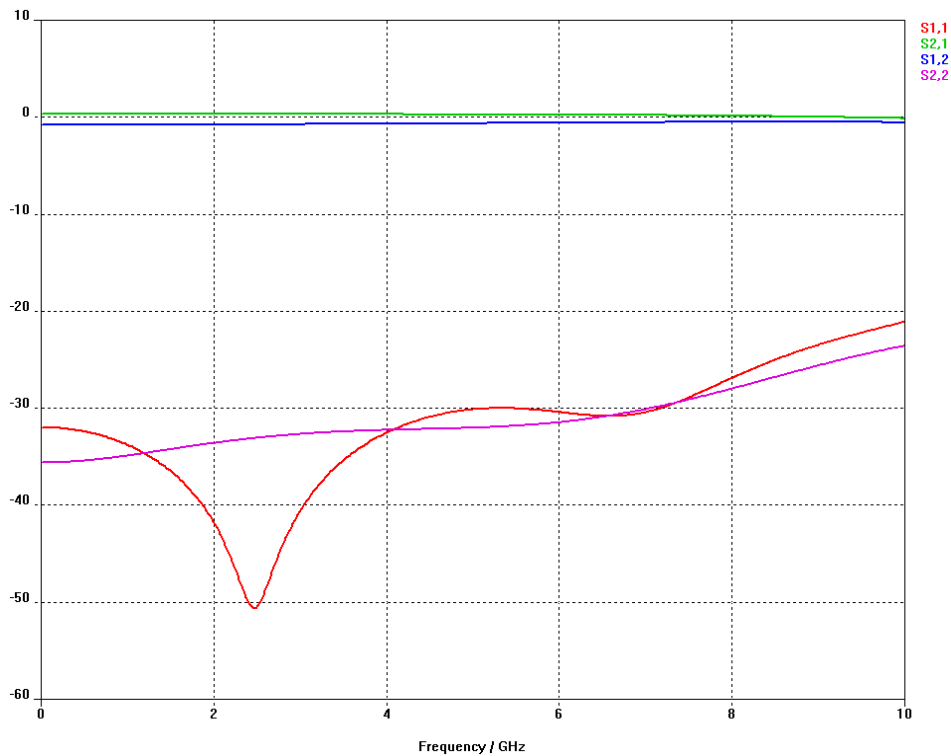

Figure 18.   Stripline feedthrough scattering parameter

2.   Hybrid Ring Check

The response of the hybrid ring is first checked in *CST* to ensure that the reflection coefficients at the ports are acceptable. The design layout of the hybrid ring in *CST* is shown in Figure 19.

The four striplines at the ports have 50Ω characteristic impedance and that of the ring is 70Ω. The yellow portion is the bare substrate where the conductor is removed by etching. The simulations in *CST* show that the port impedances at both ports is about 54Ω, 4Ω higher than the intended characteristic impedance of 50Ω.

The simulated scattering parameter responses are shown in Figure 20. All ports have less than 15 dB return loss at the designed frequency of 7.5 GHz. The isolation between ports that are adjacent ($S_{12}, S_{21}, S_{23}, S_{32}, S_{34}, S_{43}, S_{14}, S_{41}$) to each other are low, around 4-6 dB. This means about half of the power injected into a port will be absorbed by the adjacent ports. This is same as the predicted values since the input signal will be split into half upon entering a port and travels a quarter-wavelength on one side and one and one-quarter wavelengths on the other. Both waves will meet at adjacent ports with the same phase and amplitude. The ports that are diagonally opposite ($S_{13}, S_{31}, S_{24}, S_{42}$) of each other achieve good isolation as predicted due to the half-wavelength path difference. The simulation values compare to the predicted values [Ref. 2] in accordance to the working principle of the hybrid ring.
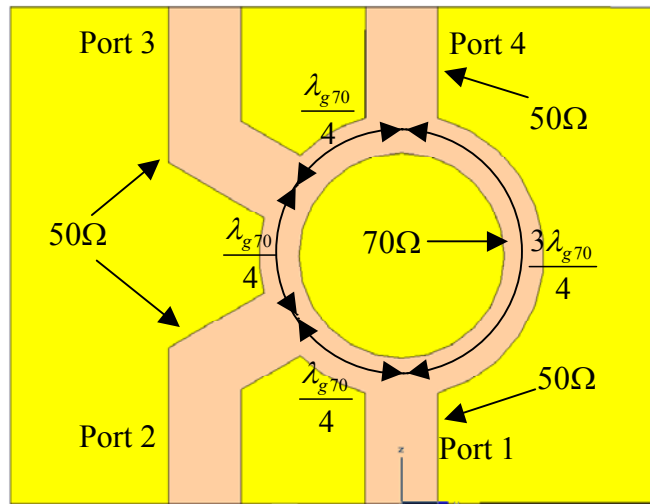

Figure 19.   Hybrid ring (also known as "rat-race")

When port 1 is used as the input, port 2 can feed one of the dipole arms and port 4 which has a reverse polarity from port 2 can feed the other arm. Port 3 is then used to provide a difference voltage that is a measure of difference in phase between the two dipole arms.

S-Parameter Magnitude in dB

S1,1
S2,1
S3,1
S4,1
S1,2
S2,2
S3,2
S4,2
S1,3
S2,3
S3,3
S4,3
S1,4
S2,4
S3,4
S4,4

S22/S33

S11/S44

Frequency / GHz
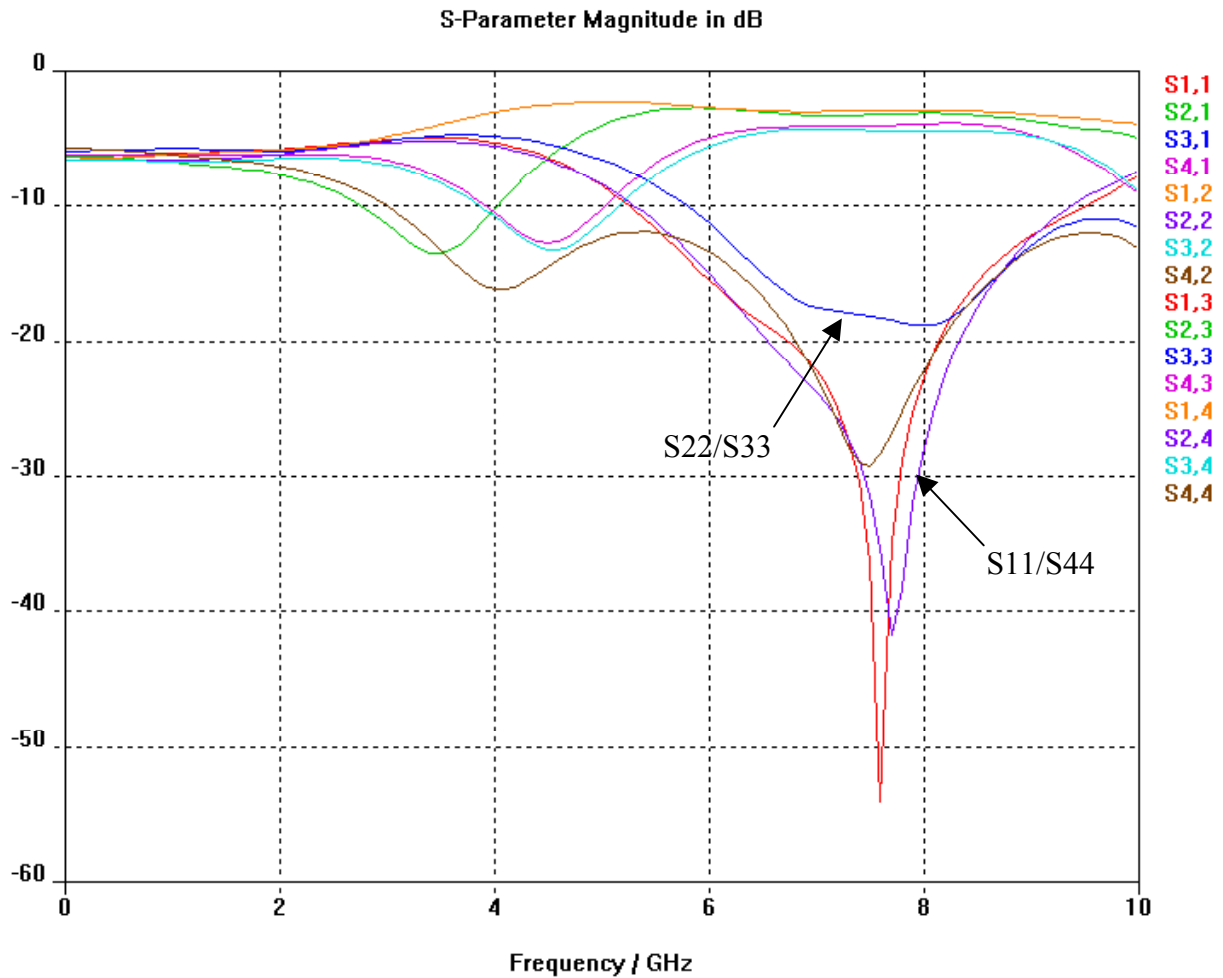
Figure 20.   Scattering parameters of a hybrid ring

3.   Coaxial Line Check

The circular coaxial transmission line is modeled using the specifications of RG141/U as this will be the actual cable used in the array. The Teflon dielectric has a relative permittivity of 2.1.

CST calculates the impedance of the waveguide as $52\,\Omega$ which is off by only $2\,\Omega$ from the specification. The scattering parameter plot shows that there is a smooth flow of power from port 1 to 2 and vice versa, with very low reflection coefficients at each port.

34
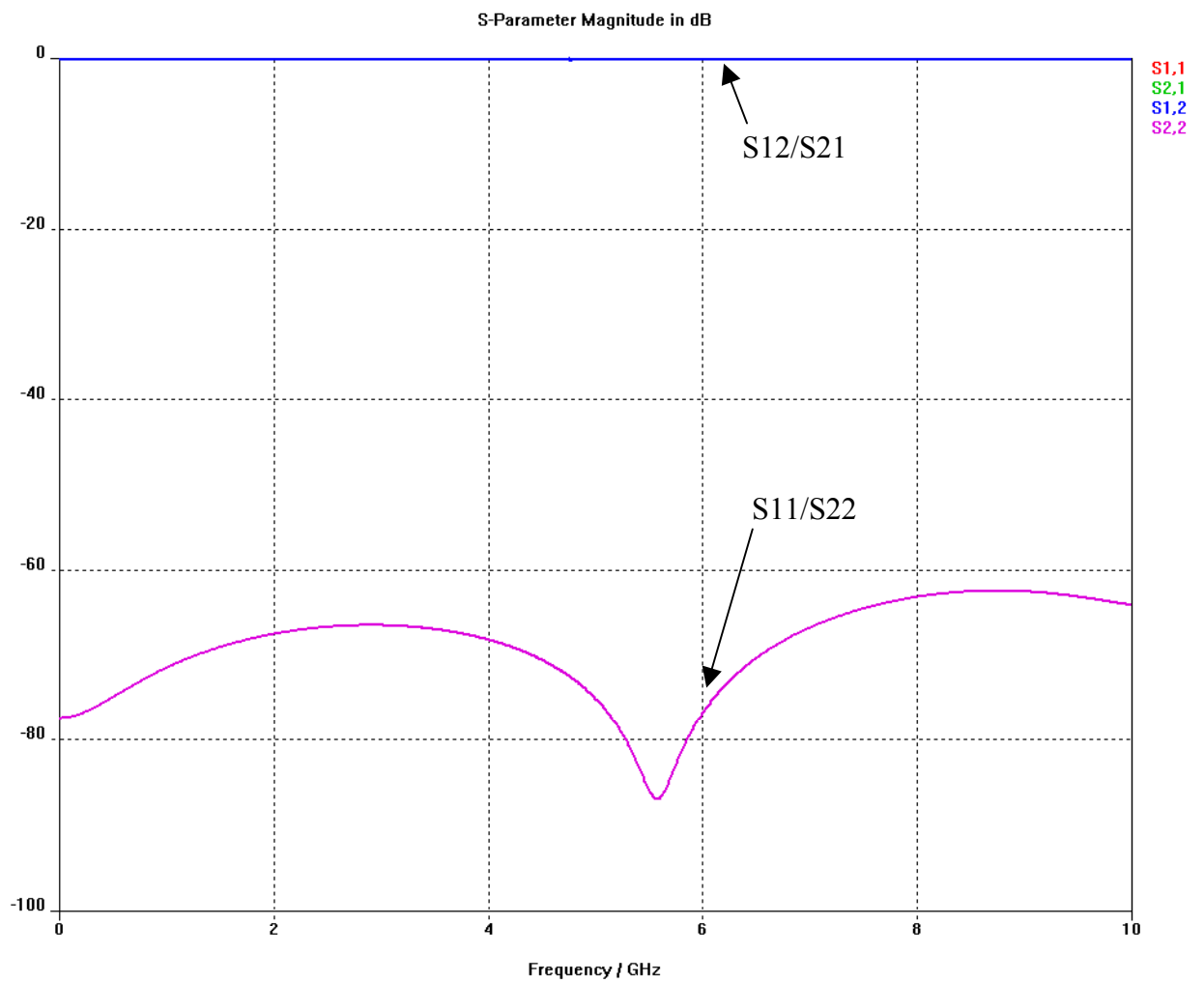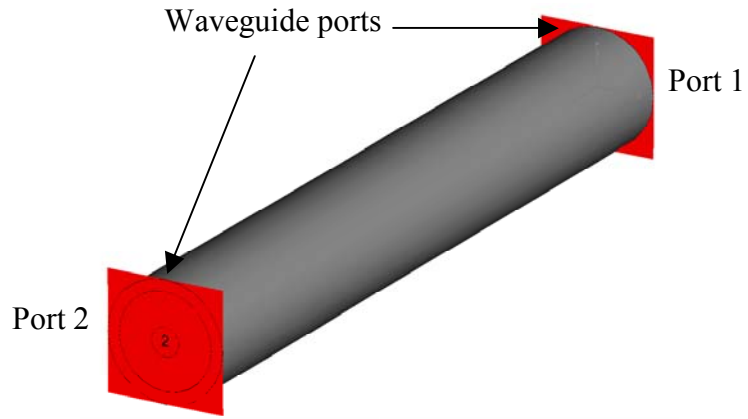
Figure 21.　A coaxial section and its scattering parameters

4.   Dipole Arm

The dipole arm dimensions are adopted from previous designs. The dipole terminal impedance is $100\,\Omega$ and must be matched to the $50\,\Omega$ line to prevent reflections. The matching between $100\,\Omega$ and $50\,\Omega$ is achieved by a quarter-wavelength transformer with a characteristic impedance of $70\,\Omega$. The length of the dipole arm, as shown between points 1 and 2 in Figure 22(a) is varied, and the scattering parameters are checked. The results are shown in Appendix D.

The dipole resonates near 8.6 GHz instead of 7.5 GHz. This could be due to the contributions from some mismatches, variations in the line widths, and the thin dielectric behind the dipole. The formulas used to calculate line widths also have many approximations which contribute to the frequency difference. Nevertheless, the dimension of 590 mils is chosen, and the scattering parameters S_{11} and S_{22} are lower than -15 dB at 8.6 GHz. Moreover, the frequency is not of importance in this investigation as the objective is to examine mutual coupling rather than to design an antenna that works at a specified frequency.

5.   Port Matching

Initially, there was a mismatch at both ports when the hybrid ring is connected to the dipole arms, as shown in Figure 23. At port 1, higher reflection is encountered and the port resistance is therefore lowered by increasing the width of the $50\,\Omega$ stripline by 60 mils. At port 2, the resonant frequency for S_{22} is higher, and therefore a tab is added to the stripline that exits from the hybrid ring. The length of the line is extended by 100 mils and the width is reduced by 80 mils.
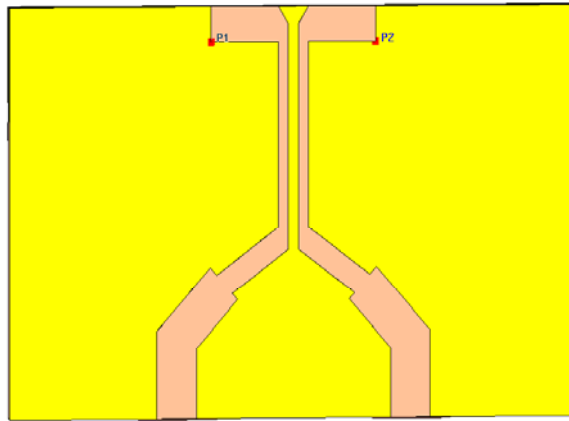
(a)
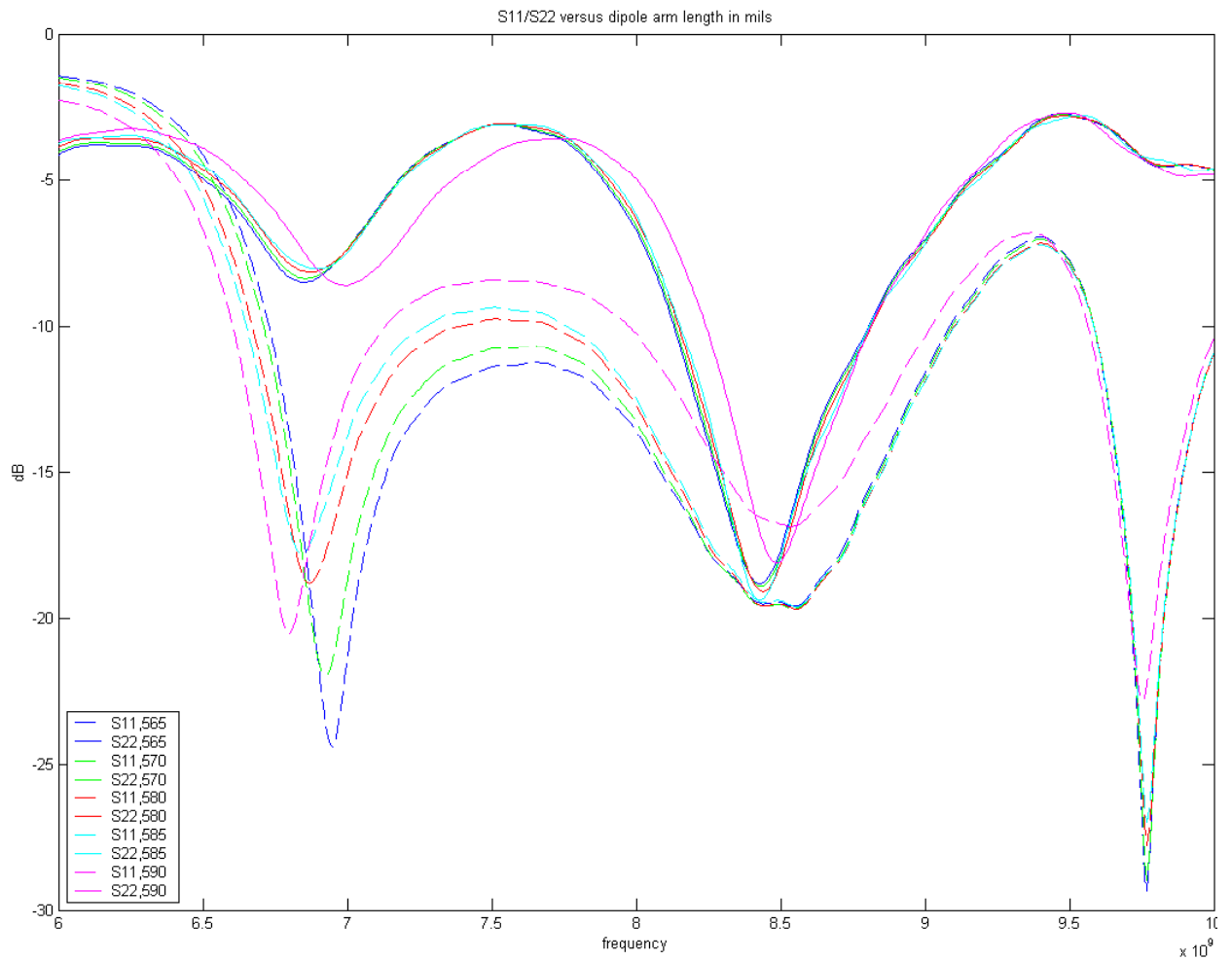
(b)

Figure 22.   (a) Dipole arm length, (b) Scattering parameter versus dipole arm length

These modifications are fine-tuned by investigating the Smith charts fom *CST* after the simulations. For example, despite modifying the strip width to achieve a matched condition at 8.7 GHz, S_{11} still has an inductive value of 32.1+2.9j and S_{22} has a capacitive value of 52.5–8.4j as shown in Appendix E. The theory used in transmission lines [Ref. 3] is applied to eliminate the complex portion of the reflection coefficients. In the simulations conducted, short-circuit and open-circuit stubs were tried, but they did not achieve better results than the configuration shown in Figure 23.
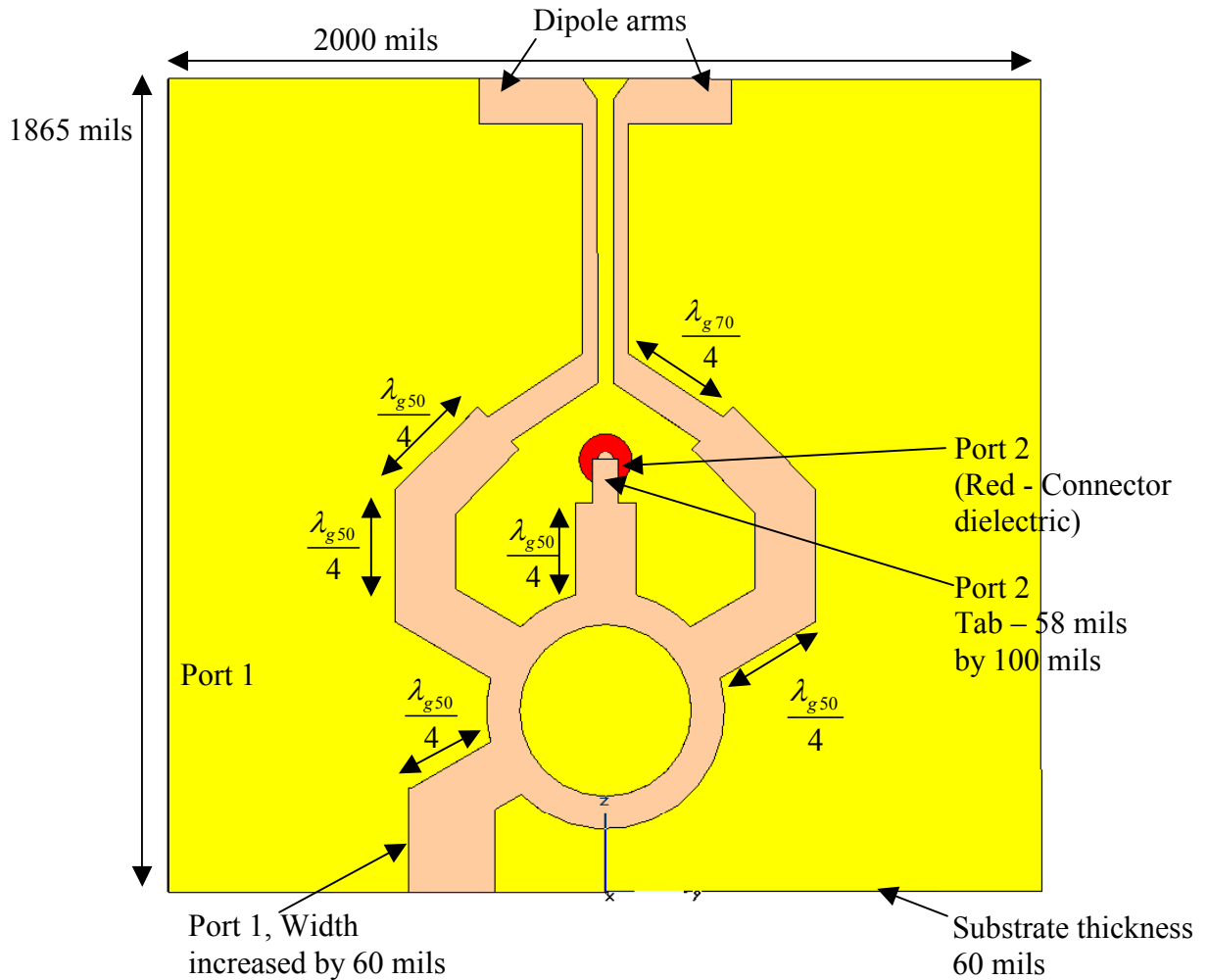
Figure 23.   Microstrip line with dimensions in wavelengths
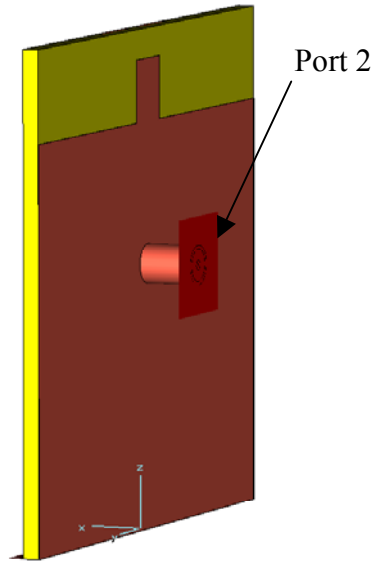
Figure 24.   Back view of single dipole element

Upon completing the modifications, the scattering parameters are obtained from *CST* and the performance is shown in Figure 25. Both S_{11} and S_{22} achieve more than 15 dB return loss at 8.7 GHz and the bandwidth as defined by 15 dB return loss is 150 MHz. The actual performance can be verified only after fabrication and measurement.

6.   Single Dipole with Coaxial Feed

Due to the software constraints, the *CST* is able to assign waveguide ports only at the bounding box that defines the domain in which Maxwell's Equations are applied. Thus, there is a need to guide the signal from port 2 to the boundary of the computation box. The circular coax is used and it is attached to port 2. There is no degradation of the scattering parameters as shown in Figure 26, because the additional coax has a characteristic impedance close to $50\,\Omega$ as verified in Figure 21.
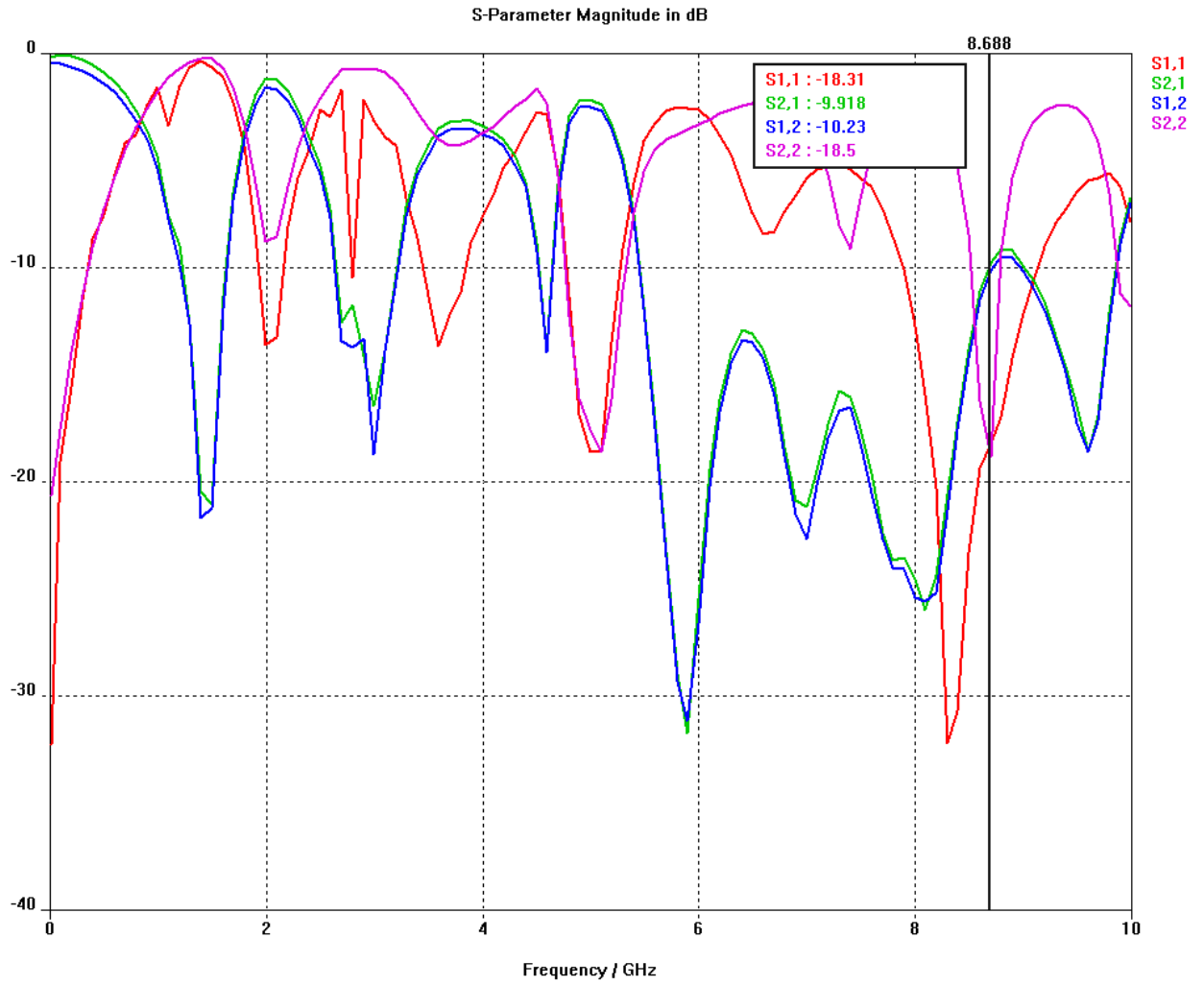
Figure 25.   Scattering parameters for the dipole element and hybrid ring
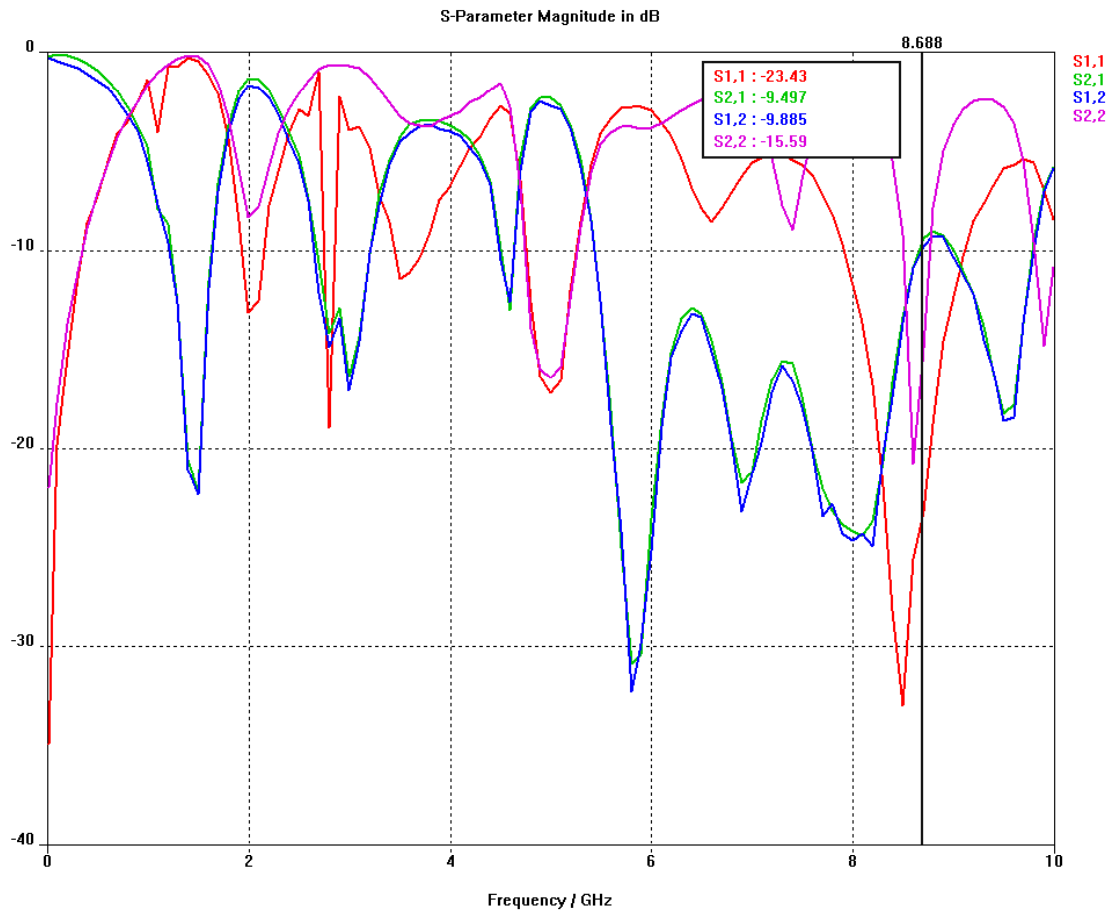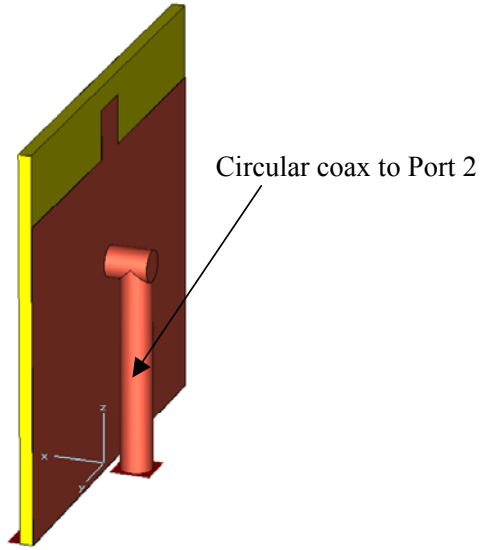
Figure 26.   Single dipole element with coax

7.   Array Assembly

Three individual dipole elements are assembled together to form the three-element dipole array as shown in Figure 27. A ground plane is added at $0.15\,\lambda_o$ below

41

the dipole arms and stretches a quarter-wavelength (at 7.5 GHz) beyond the edges of the individual dipole's substrate.

There are 36 parameters from the six ports and the scattering parameters are listed in Appendix F. The reflection coefficients at the ports are extracted and presented in Figure 28. The resonant frequency remains at 8.7 GHz with about 100 MHz of bandwidth. Although there is another resonant frequency at about 4.9 GHz with a low reflection coefficient, the transmission between ports 3 and 4 (a measure of the isolation), as shown in Appendix F is too high. The poor isolation between ports may cause interference between them. At 8.7 GHz, the transmission parameter between the ports is lower.
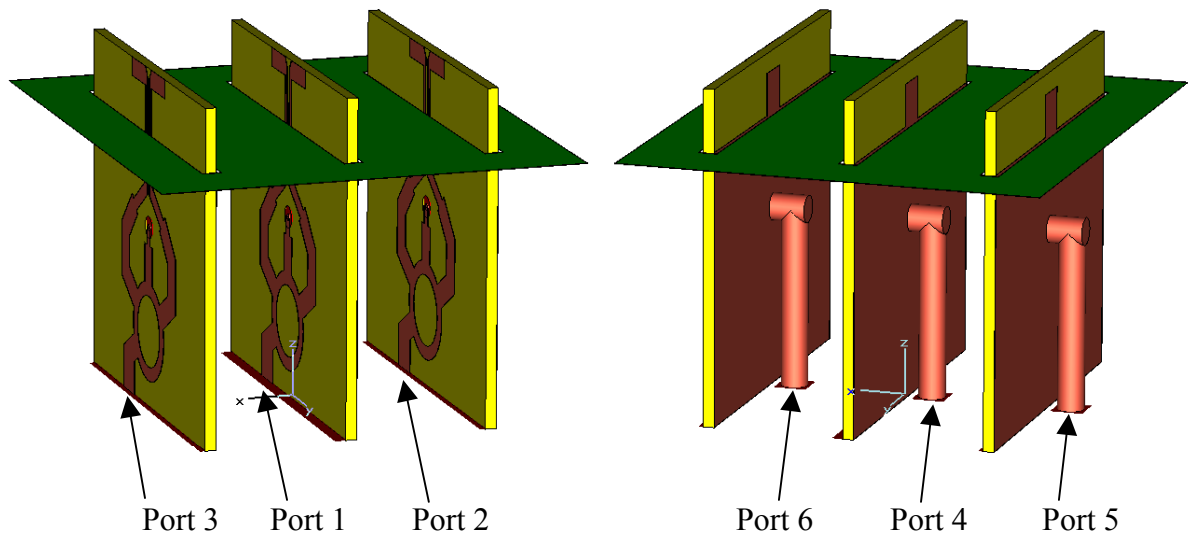
Figure 27.   Dipole arrays with ground plane
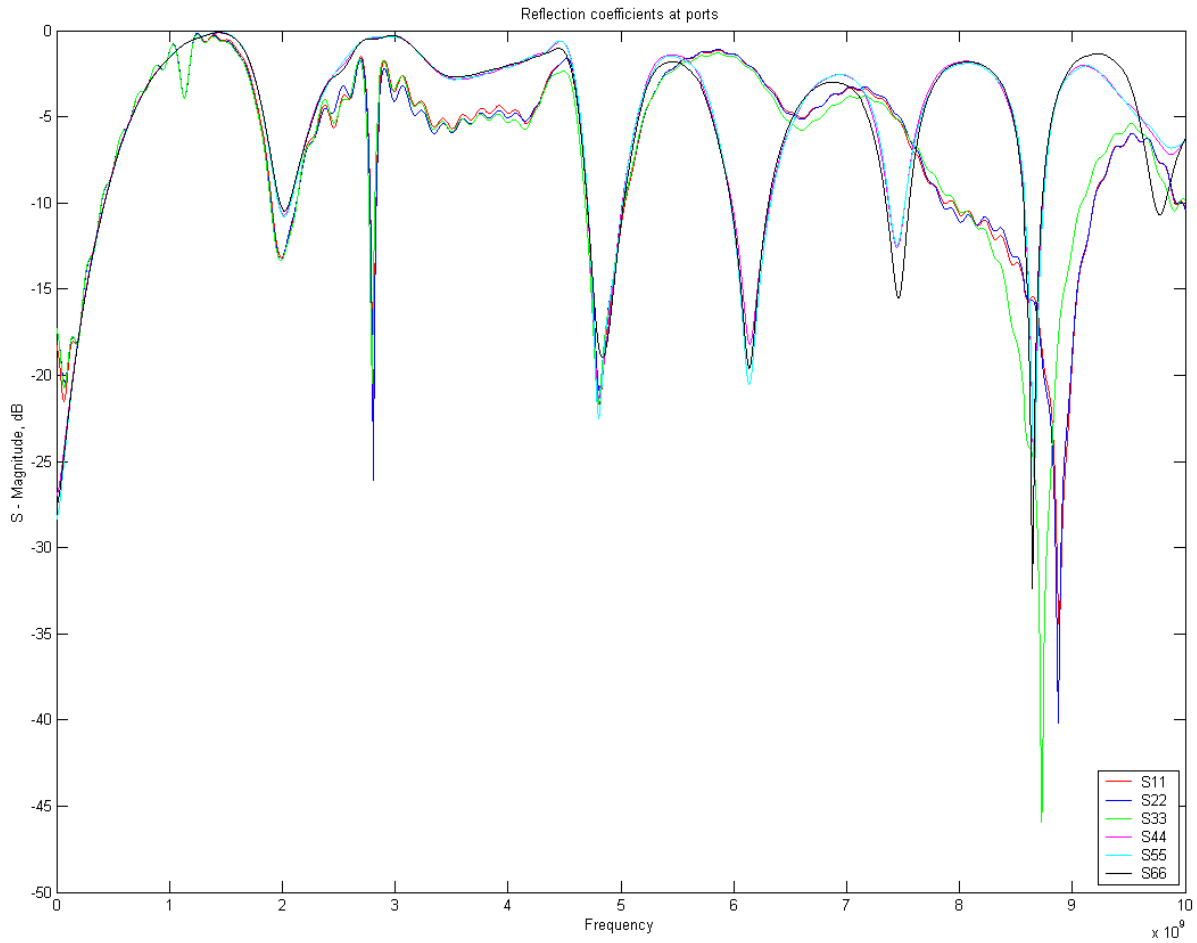
Figure 28.   Scattering parameters at the input ports

8.   Fabricated Dipole Elements

The dipole elements shown in Figures 29, 30 and 31 are dipoles 1, 2 and 3 respectively. The copper traces are covered with copper tapes at both ports to increase the capacitance for tuning the scattering parameters. SMA coax connectors are soldered to the ports. The boards are measured using a vector network analyzer (VNA).
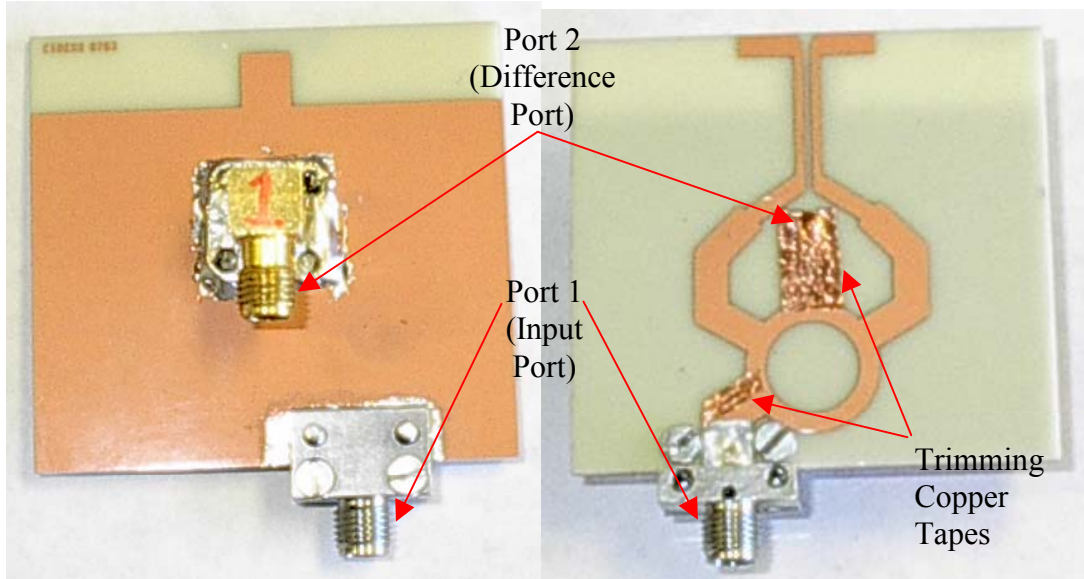
Figure 29.   Fabricated dipole element 1
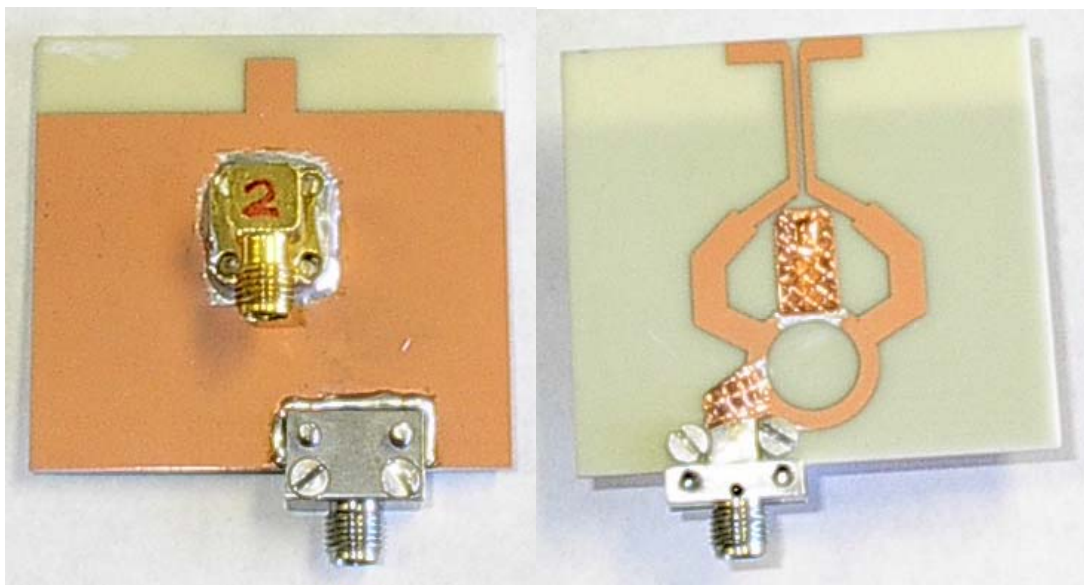
Figure 30.   Fabricated dipole element 2
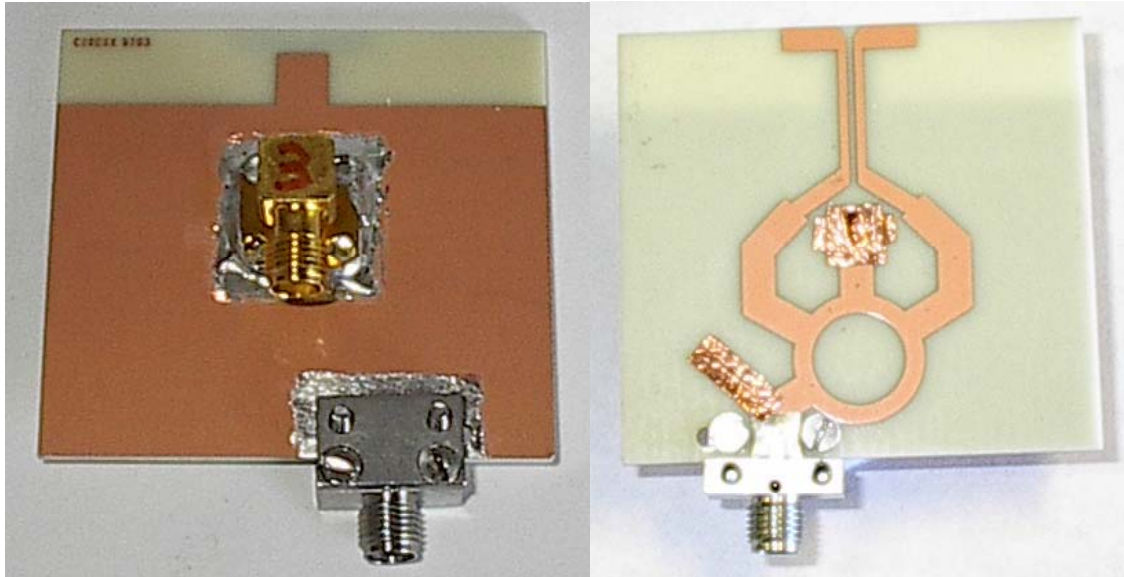
Figure 31.   Fabricated dipole element 3

9.   Scattering Parameters – Network analyzer

The scattering parameters obtained from the network analyzer for each of the fabricated dipole elements are in Figure 32, Figure 33 and Figure 34.
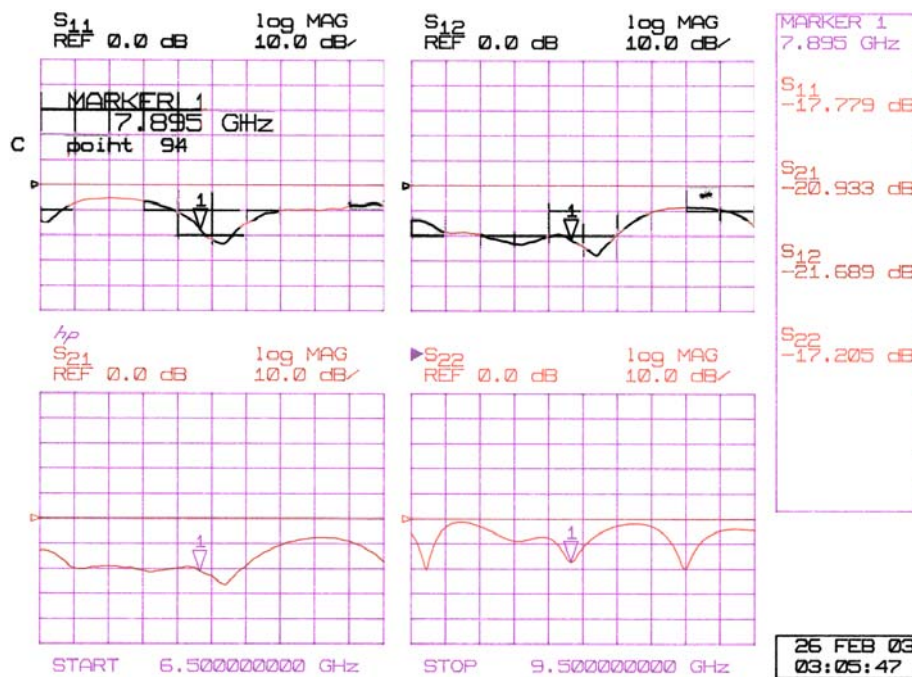

Figure 32.   Dipole 1 scattering parameters
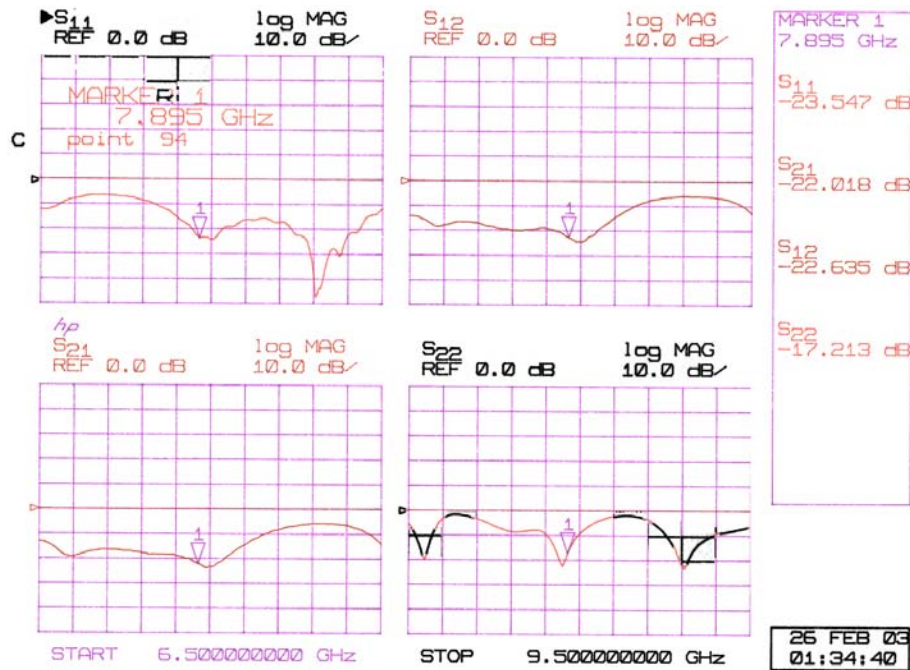
Figure 33.   Dipole 2 scattering parameters
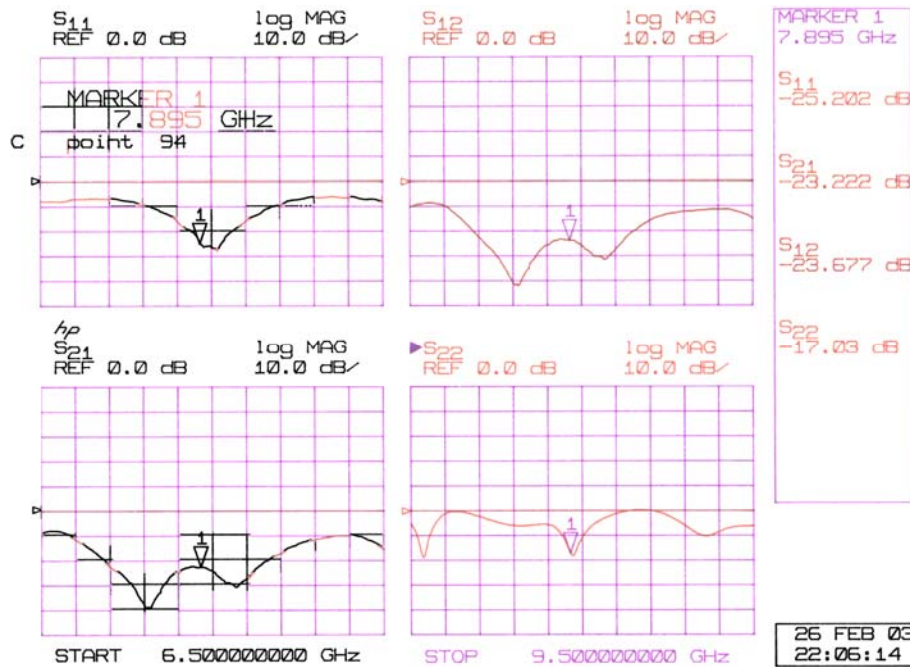
Figure 34.   Dipole 3 scattering parameters

The printed antennas generally show less than 17 dB at 7.895 GHz for S_{11}, S_{12}, S_{21} and S_{22} after the traces on the printed circuit board were trimmed. The scattering parameters for the three dipole elements are shown in Table 2.

46

Element	S_{11} (dB)	S_{12} (dB)	S_{21} (dB)	S_{22} (dB)
Dipole 1	−7.78	−21.69	−20.93	−17.21
Dipole 2	−23.55	−22.64	−22.02	−17.21
Dipole 3	−25.20	−23.68	−23.22	−17.03

Table 2.   Scattering parameters obtained from the VNA

10.   Antenna Element Patterns

The setup for the antenna pattern measurements is shown in Figure 35.   More pictures are shown in Appendix G. A ground plane is placed $0.15\,\lambda_o$ below the dipole for all measurements. The patterns shown have not been normalized to the peak gain.


(a) *H*-Plane Measurement setup

(b) *E*-Plane Measurement setup
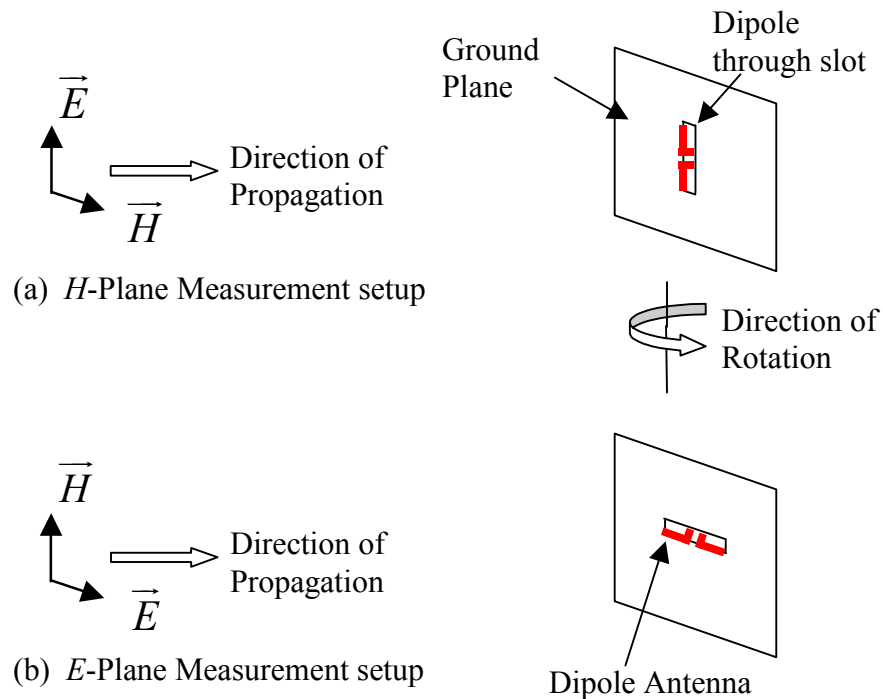
Figure 35.   Setup for *E* and *H* plane field measurements

a.   *Port 1 Patterns – Port 2 Terminated with Matched Loaded*

Figure 36, Figure 37 and Figure 38 show the antenna patterns signals obtained at port 1 which is the sum port of the hybrid ring.
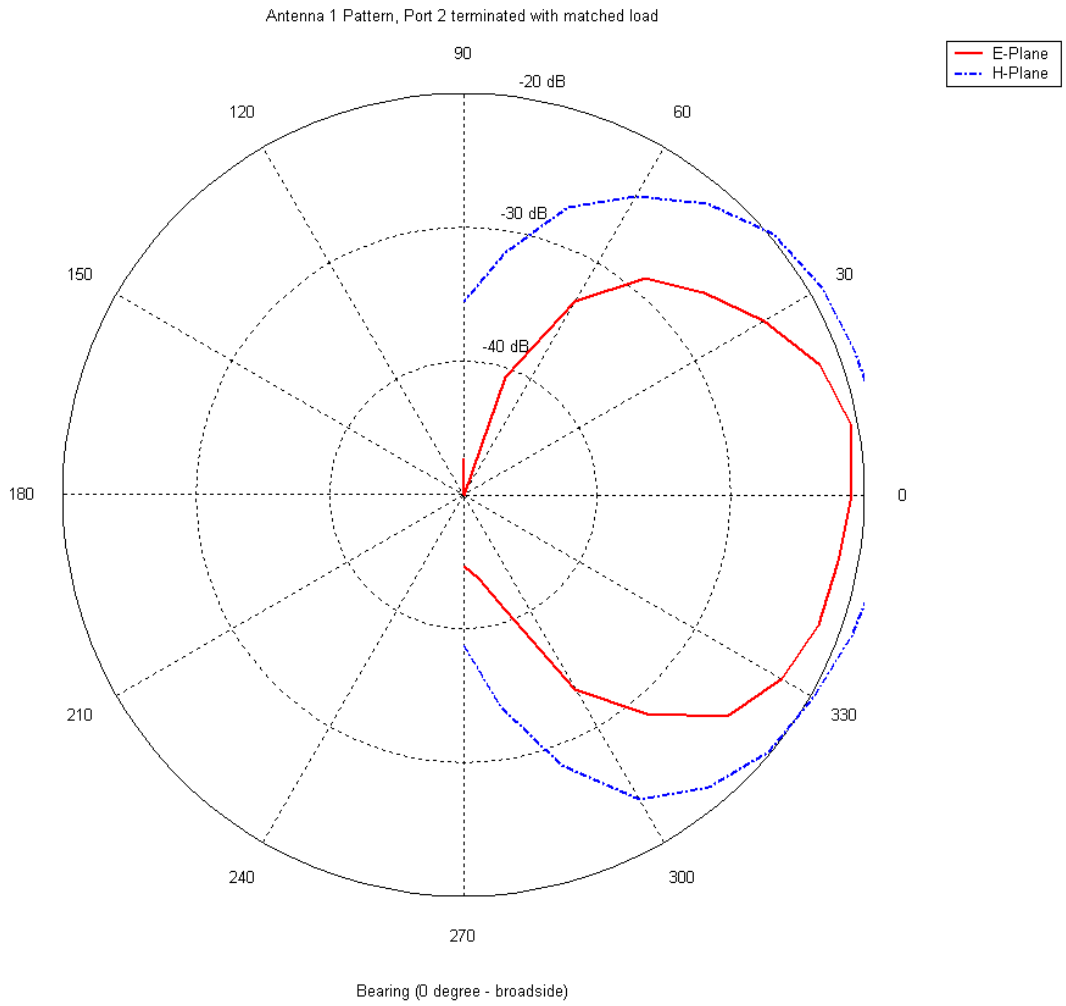
Figure 36.   *E*/*H*-plane pattern for antenna 1 at port 1 with port 2 terminated

Antenna 2 Pattern, Port 2 terminated with matched load
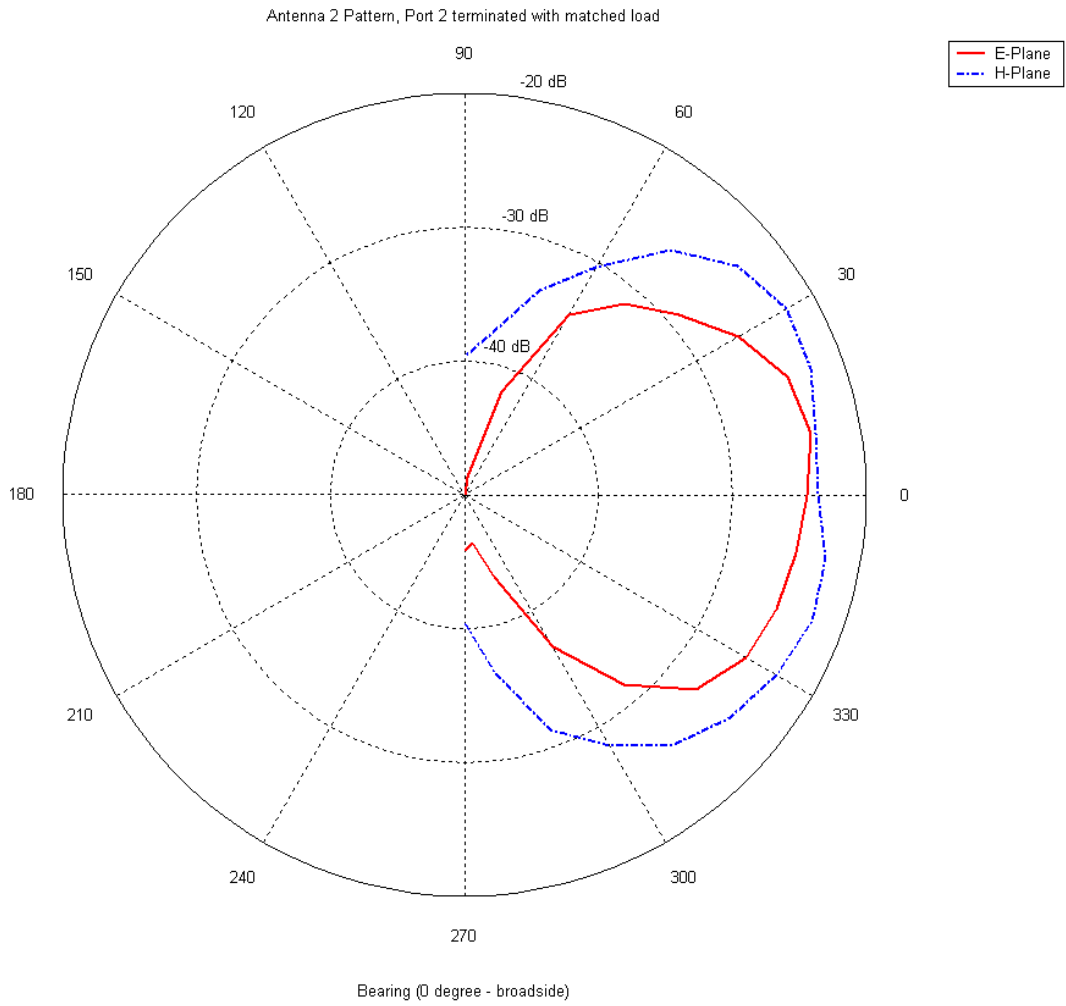
Figure 37. *E*/*H*-plane pattern for antenna 2 at port 1 with port 2 terminated

49
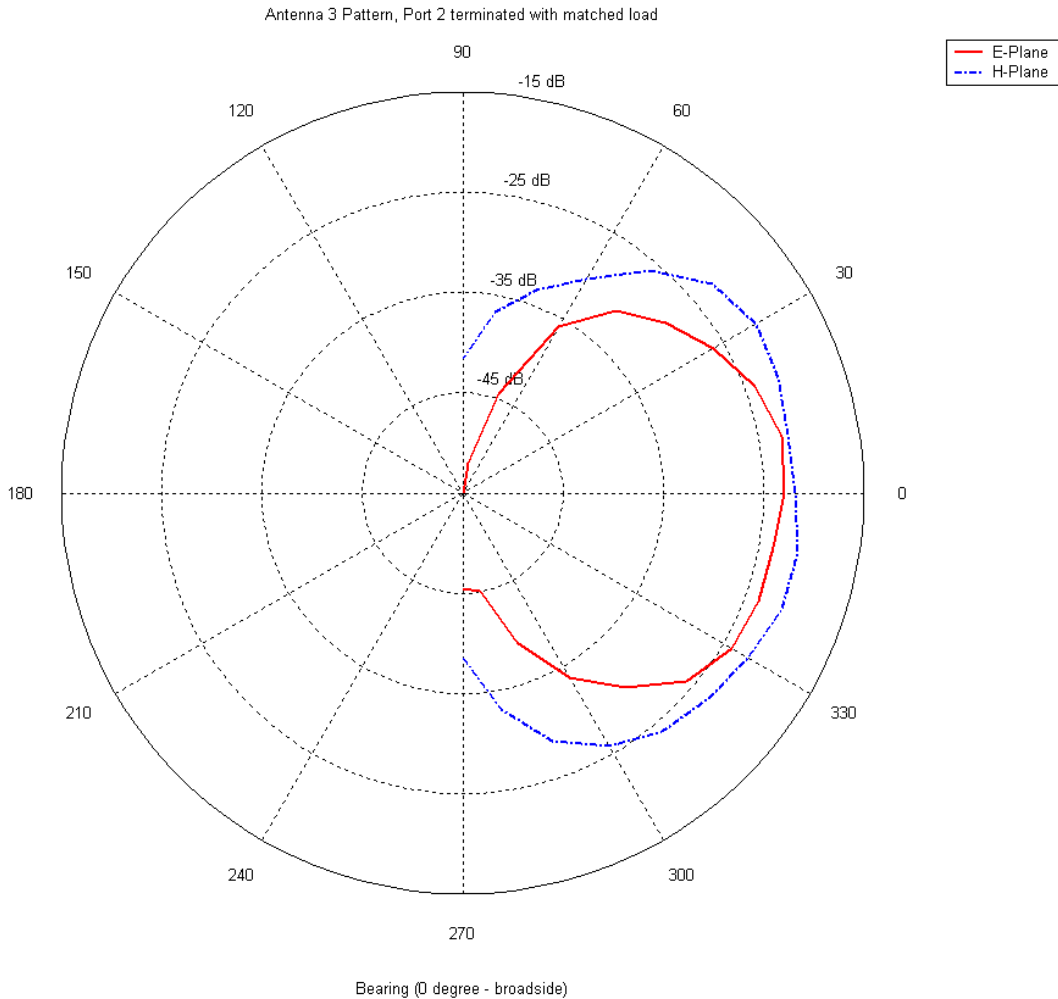
Figure 38.   *E*/*H*-plane pattern for antenna 3 at port 1 with port 2 terminated

The power at port 1 is generally 15 to 20 dB higher than that generated at port 2. The pattern follows the pattern generated from a dipole placed a quarter of a free space wavelength above an infinite ground plane. The *H*-plane strength diminishes as it approaches $\pm 90°$ as contrary to a dipole without ground plane. This pattern is validated by simulation from *CST* with a dipole along the x-axis shown in Figure 39.
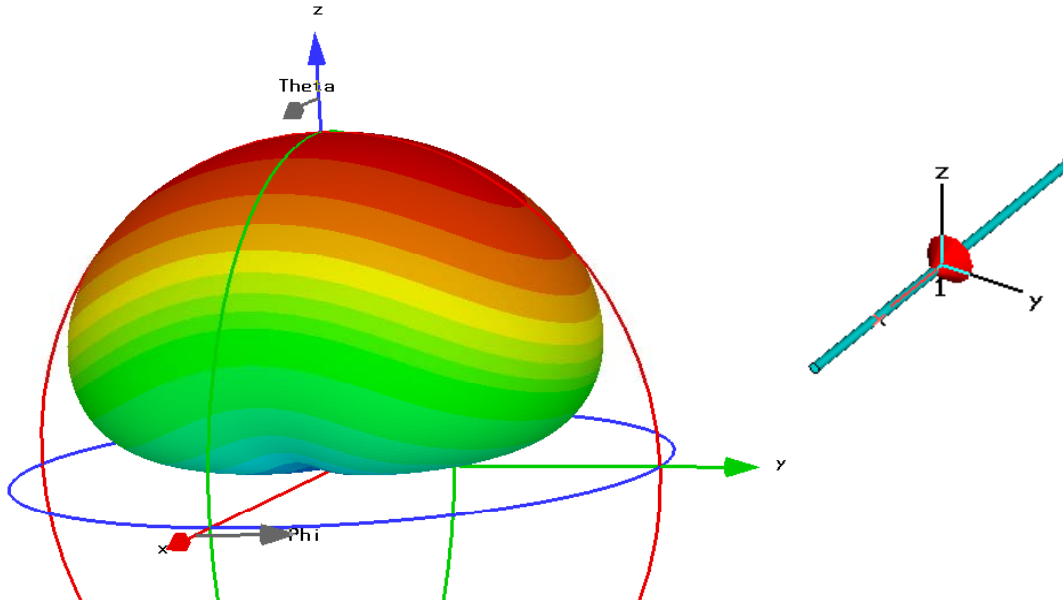
Figure 39.   Ideal pattern of a single dipole $\dfrac{1}{4}\lambda_o$ above a ground plane
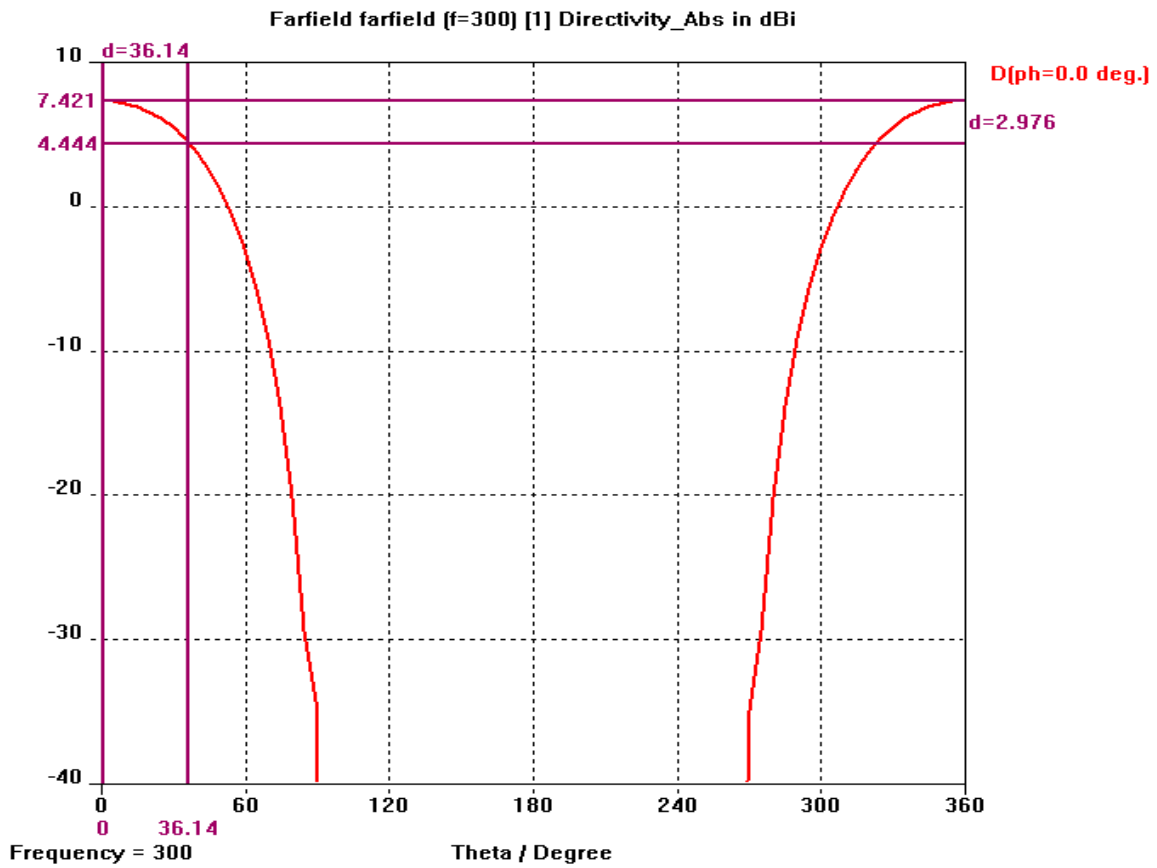

Figure 40.   Simulated beam pattern for dipole element

51

The 3-dB beamwidths obtained for the three antennas are approximately 60°. The beam pattern generated by *CST* along the *X-Z* plane is shown in Figure 40. The simulated 3-dB beamwidth is approximately 72° and the measured values are close to the simulated results.

b. *Port 2 Patterns – Port 1 Terminated with Matched Loaded*

Figure 41, Figure 42 and Figure 43 show the voltage generated at the difference-port due to the phase difference (contributed by path difference due to difference scan angles) of the wave at the two dipole arms.
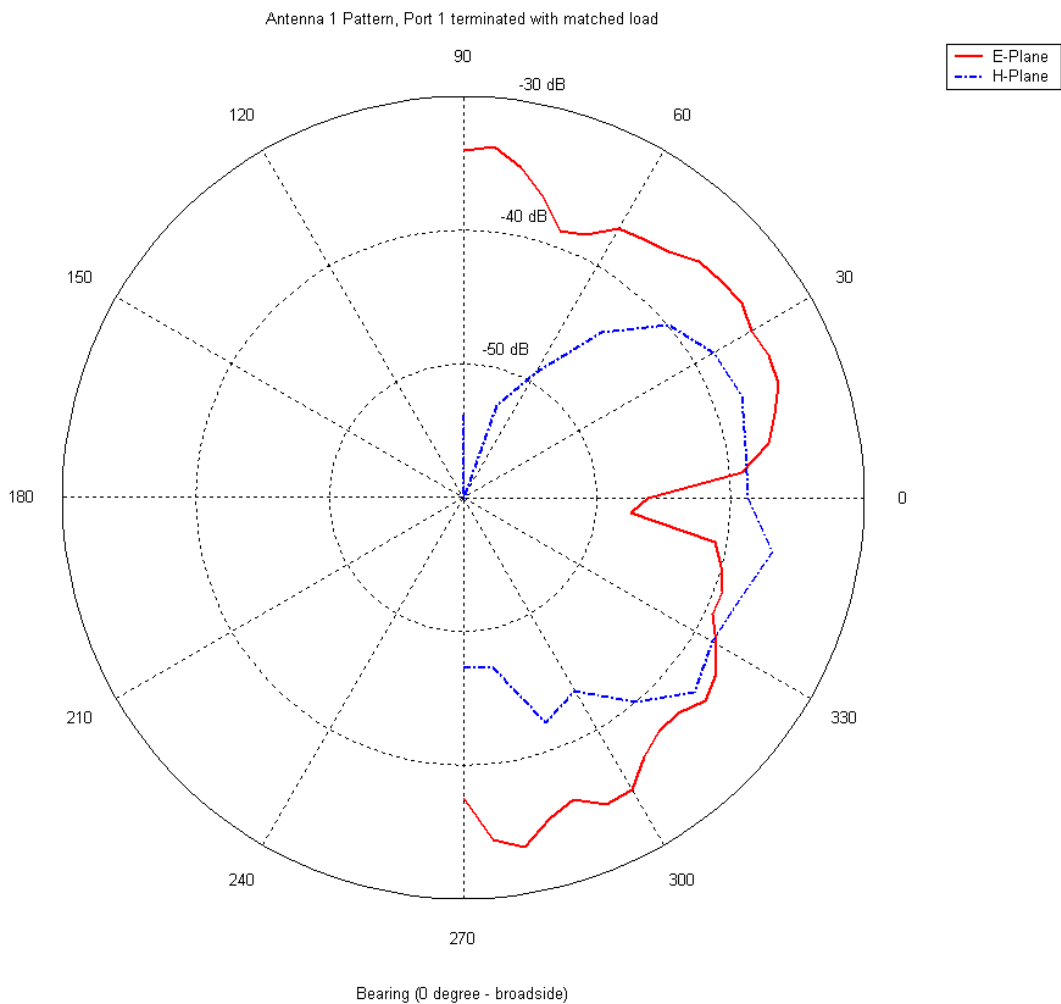

Figure 41. *E/H*-plane pattern for antenna 1 at port 2 with port 1 terminated
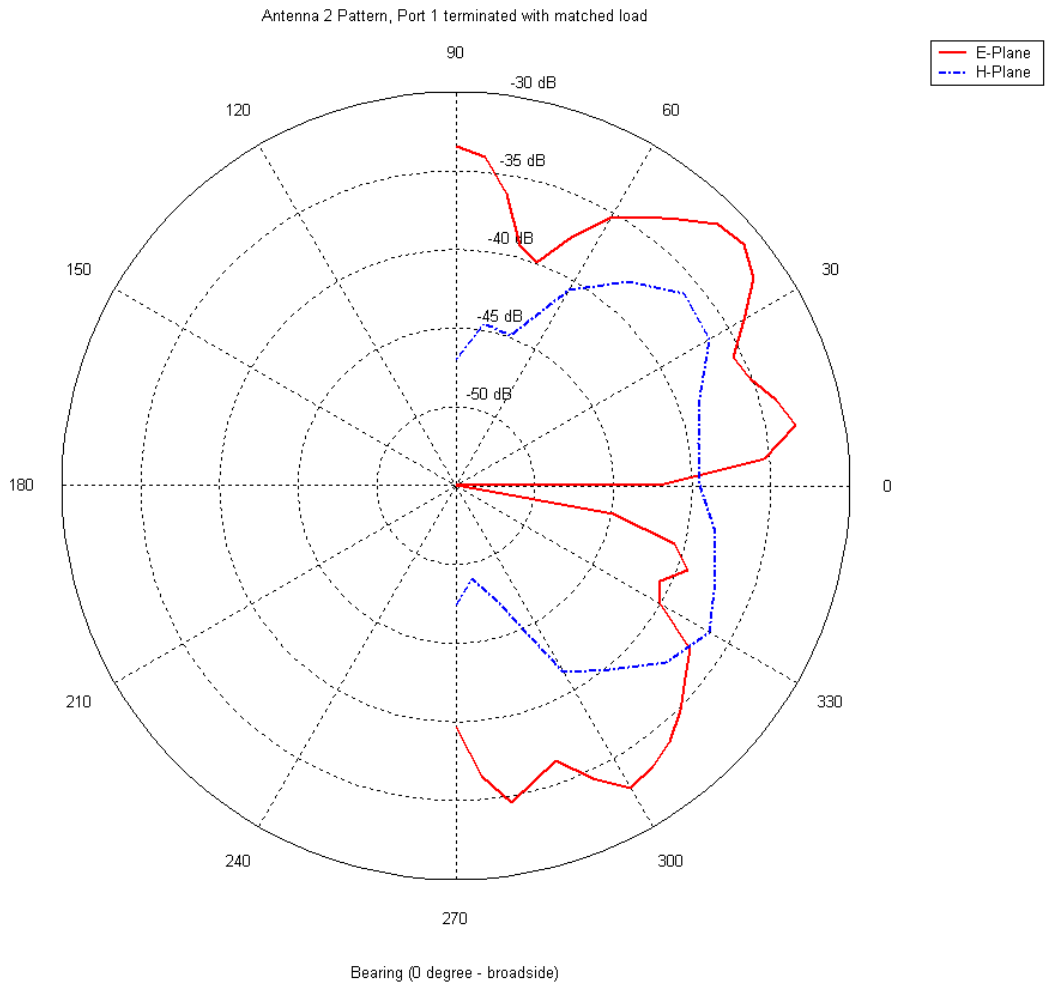
Figure 42.   *E*/*H*-plane pattern for antenna 2 at port 2 with port 1 terminated
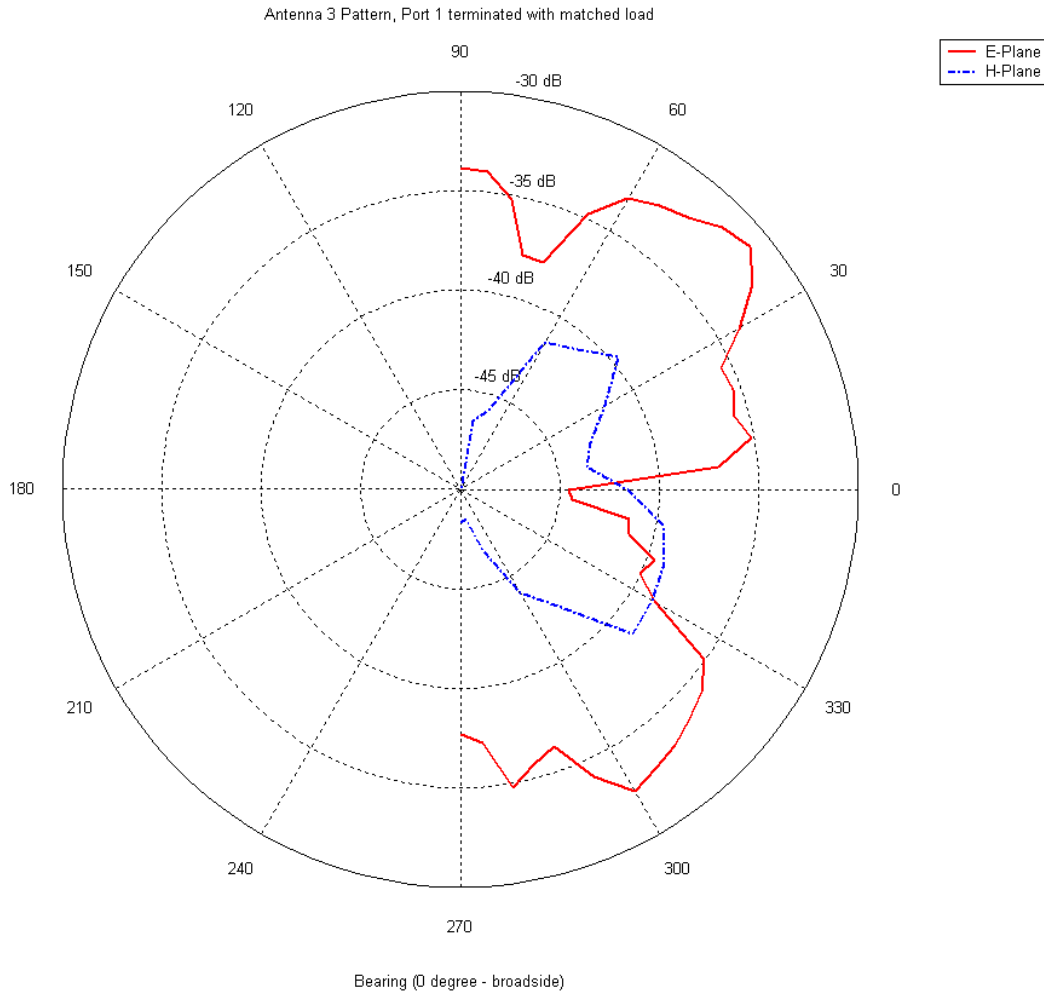
Figure 43.   *E*/*H*-plane pattern for antenna 3 at port 2 with port 1 terminated

There is a reduction in gain when the wave is approaching from 0°, i.e. broadside reception. The gain drops to approximately –50 dB (non-normalized) due to the anti-phase voltages from both arms when reception is near broadside. The signal level increases when the dipoles are rotated toward ± 90°. Ideally (for an infinite ground plane), the pattern should follow that shown in Figure 44. It varies in a $\cos\theta\sin\theta$ manner as the pattern angle θ varies from 0° to ± 90°. The reduction of the power to zero as the scan angle reaches ± 90° is due to the crossed-polarization between the incident wave and the dipole element. The measured data are more erratic because of the finite ground plane and diffraction from the ground plane edges. Also the alignment of the antenna on the pedestal is only approximate. The broadside reference (θ=0°) could be off by 2° or so.
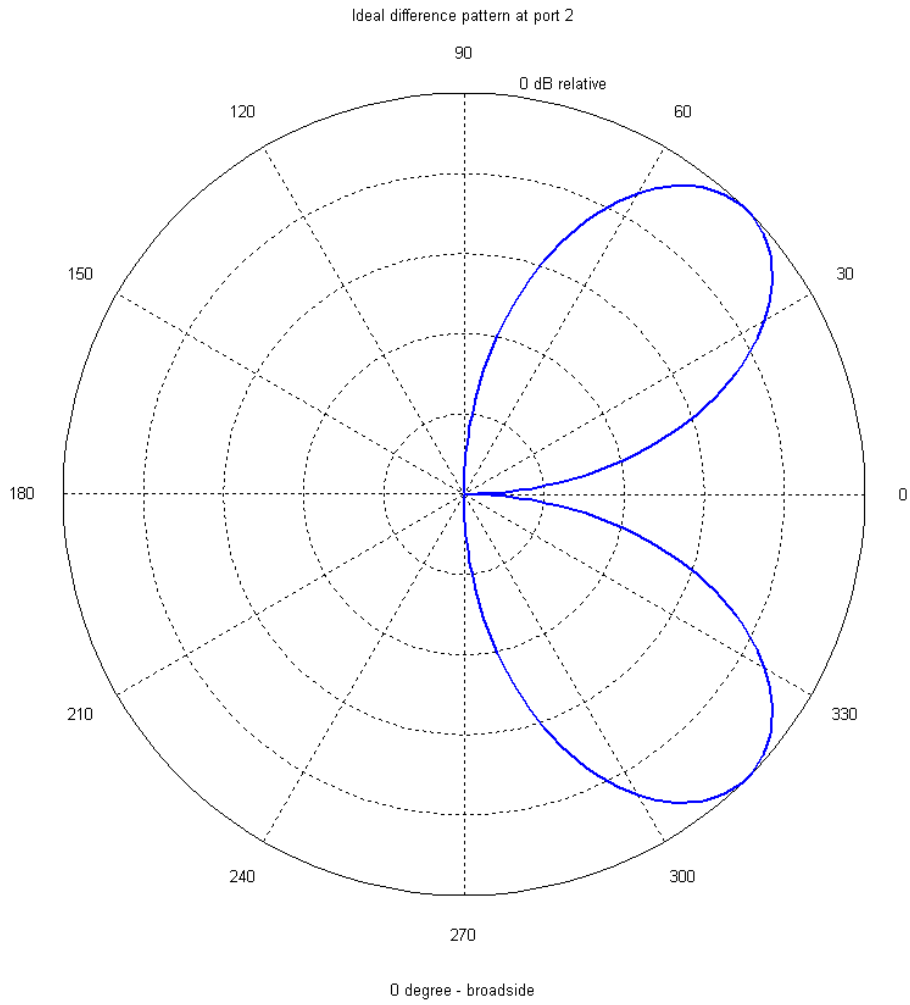
Figure 44.   Ideal power pattern at port 2 (infinite ground plane)

THIS PAGE INTENTIONALLY LEFT BLANK

IV. DISCUSSION OF RESULTS

A. DUMMY ELEMENT COMPENSATION METHOD

It is apparent that the dummy element compensation method provides some corrections to the phase errors between array elements if the length, distance from the last dummy element, and the load connected to the terminal of the dummy element are selected correctly.

1. Load and Dummy Separation Variations

Figure 45 shows the best achievable phase difference in thick red solid and blue dash lines for scan angles between 0° (broadside) to 90° (endfire). The three-element baseline phase differences are plotted in black solid and dash lines. The corresponding dummy separations and load variations for each scan angle are also plotted in thin lines. Dummy separation values are labeled from 1 to 17 which correspond to $0.3\lambda_o$ to $0.7\lambda_o$ separations respectively in steps of $0.025\lambda_o$. Load values are as indicated in the figure with 1, 2, 3, and 4 denoting 1, 70, 140 and $100,000\,\Omega$ respectively. With a combinations of varying compensations, both dipole pairs achieve less than 8° of phase error at broadside and close to 0° at endfire. The best achievable phase difference in the two dipole pairs is discussed in the following sections.
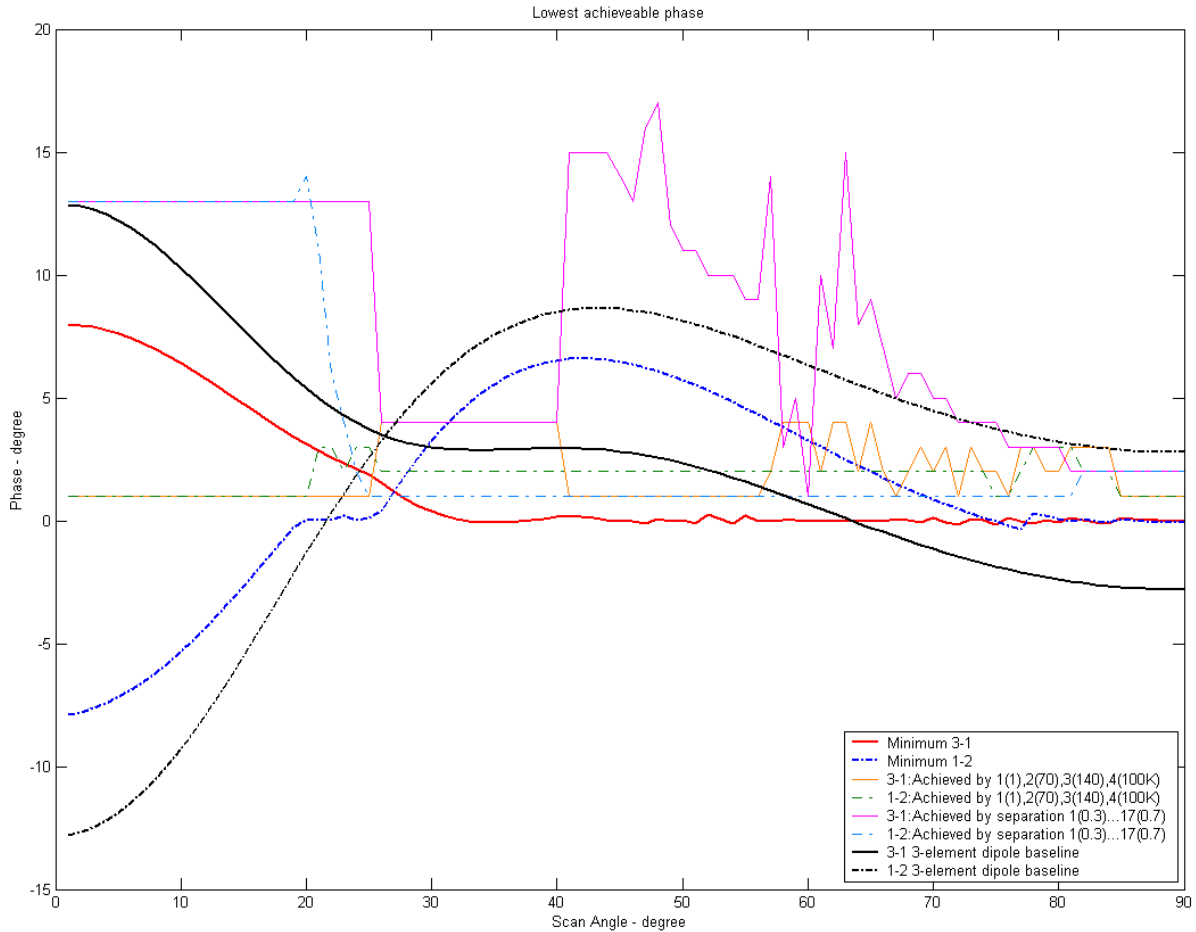
Figure 45. Best achievable phase difference

a. 3-1 Dipole Pair

At broadside scan angle, the 3-1 dipole pair has a phase difference of 8° and drops to less than 1° error when the scan angle is greater than 25°. It gradually approaches zero phase difference when the scan angle increases beyond 30°. This is an improvement of about 5° at broadside and 3° for other scan angles compared to the uncompensated case.

The load and dummy separation that provides best compensation varies and does not stay at one value after the 25° scan angle. A close examination at the plot in Figure 68 for the $0.6\lambda_o/1\,\Omega$ plot and the $0.375\lambda_o/100{,}000\,\Omega$ plot in Figure 59 of Appendix A indicates that although $0.6\lambda_o/1\,\Omega$ does not have lowest phase difference

between 25° to 40°, it differs from the $0.375\,\lambda_o/100{,}000\,\Omega$ case by only less than 1° phase difference.

The $0.6\,\lambda_o/1\,\Omega$ generally provides less than 5° phase difference for scan angles above 25° with its maximum of 4° phase difference at 90° scan angle. Therefore it is concluded that $0.6\,\lambda_o/1\,\Omega$ case generally gives the best compensation throughout the whole scan angle range. For scan angles where the $0.6\,\lambda_o/1\,\Omega$ case does not achieve the lowest phase difference, it however does not differ from the best case by more than 2°.

The contributing factors for the corresponding scan angles are summarized in Table 3.

Scan Angle	<25°	25°-40°	>40°
Load (Ω)	1	100k	Fluctuates
Dummy Separation (λ_o)	0.6	0.375	Fluctuates

Table 3.   Factors contributing 3-1 dipole pair compensation

b.   1-2 DipolePair

Table 4 summarizes the settings that give the best compensation in the 1-2 dipole pair. The phase difference drops from 8° to less than 1° when the scan angle is increased from broadside to 18°. Thereafter, it remains within 1° phase difference until the scan angle reaches 28°. Between 28° and 70°, the phase difference increases to a peak of 7° at scan angle 42°. Beyond 73°, the phase difference approaches zero. In the medium scan angle range, although it does not achieve the near zero phase difference as in the case of the 3-1 dipole pair, it produces about a 2° to 3° improvement compared to the uncompensated case.

The fluctuations of the optimum load and dummy separation settings between scan angle of 18° to 25° to achieve best compensation is of little concern. This is because all phase difference plots for the range of settings differ from each other by less than 1° and cross each other around this scan angle region. The differences between plots from the best setting and other settings are generally small even if the latter is not the lowest.

59

Scan Angle	<18°	18°-25°	25°-73°	> 73°
Load (Ω)	1	Fluctuates	70	Fluctuates
Dummy Separation (λ_o)	0.6	Fluctuates	0.3	Fluctuates

Table 4.   Factors contributing 1-2 dipole pair compensation

Since it is logical to maintain a single load and dummy separation value in hardware implementation, attempts are therefore made to see if the $0.6\lambda_o/1\Omega$ case provides good compensation in other scan angles values even though it may not provide the best compensation.

To achieve that, the $0.6\lambda_o/1\Omega$ case in Figure 68 and the $0.3\lambda_o/70\Omega$ case in Figure 56 of Appendix A are compared. Between scan angles 25-73°, the two phases differ by about 2° around 42° scan angle and the $0.3\lambda_o/70\Omega$ case has better compensation than the $0.6\lambda_o/1\Omega$ case. However, beyond 73° scan angle, the $0.6\lambda_o/1\Omega$ case differs by about 4° phase difference from the best case while the $0.3\lambda_o/70\Omega$ case achieves 1° phase difference. Therefore in the 1-2 dipole pair, compensation cannot be achieved with one value of load and dummy separation and it has to be changed between the $0.3\lambda_o/70\Omega$ and the $0.6\lambda_o/1\Omega$ settings.

2.   Dummy Element Length Variation

The plot for the best achievable phase difference by varying the dummy element length is shown in Figure 46. Only the short circuit case is examined because it offers the least phase difference near broadside scan angles as indicated in Appendix A. The black lines represent the baseline for the phase difference of a three-element array. The solid red and dash blue lines represent the best achievable phase difference in the 3-1 and 1-2 dipole pairs respectively. About 5° of improvement is achieved at broadside and the improvements in the rest of the scan angle vary between 0° to 3° when compared to the uncompensated case.
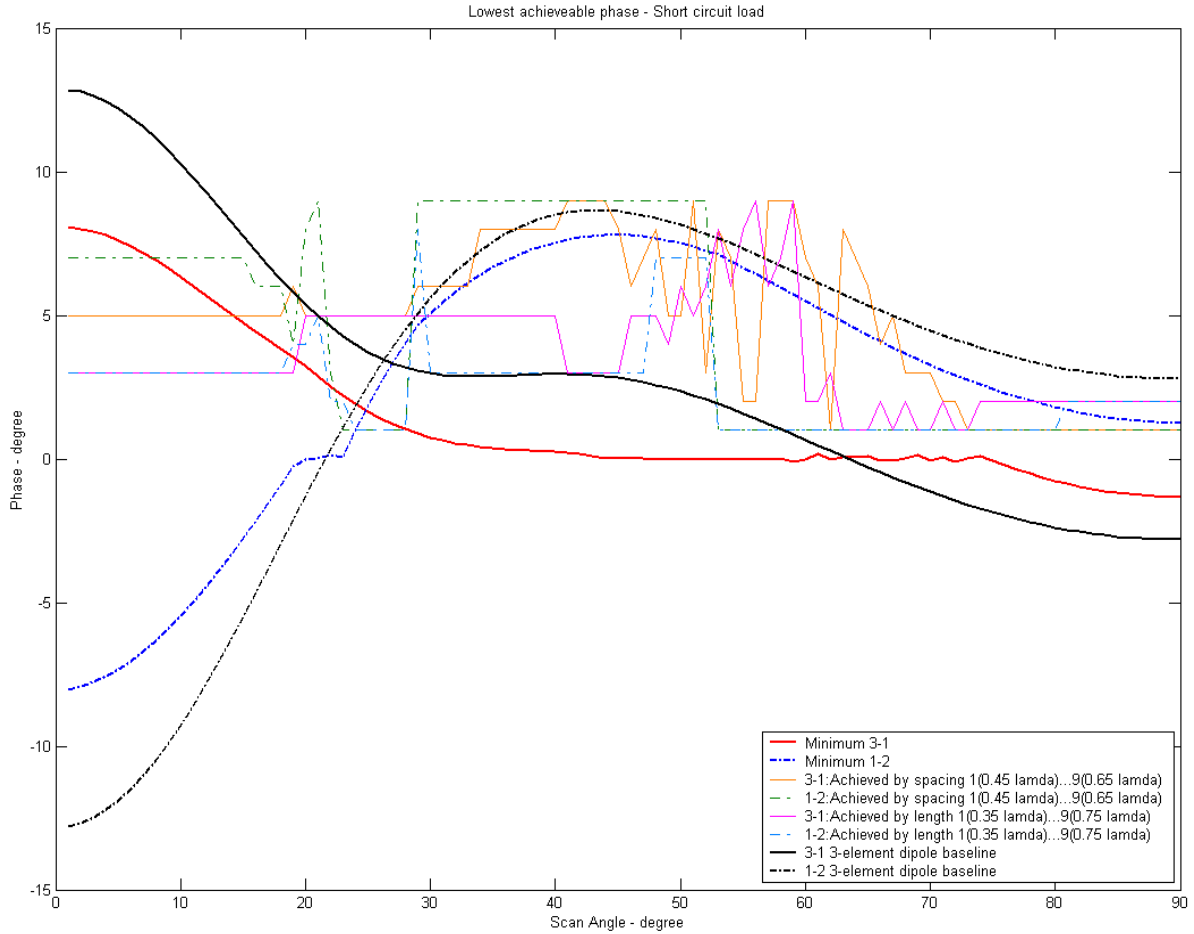
Figure 46.   Best achievable phase difference

Following the same approach, the setting combination that offers best compensation near broadside is noted. It is then used as baseline to see if it can replace the best settings at other scan angles in event that it does not provide the lowest phase difference.

a.   3-1 DipolePair

In Table 5, instead of $0.6\lambda_o$ dummy separation as previously determined, a value of $0.55\lambda_o$ provides the best compensation at near-broadside. The difference could be due to the simulations with a completely short circuit dummy element compared to a previous 1Ω case. Examining Figure 77 and Figure 79 for the $0.55\lambda_o$ and $0.6\lambda_o$ cases in Appendix B shows that the two graphs are only marginally different from one another. Thus, it should not result in large error for the studies in this section.

61

Scan Angle	< 18°	18°-20°	20°-28°	> 28°
Dummy Length (λ_o)	0.45	Fluctuates	0.55	Fluctuates
Dummy Separation (λ_o)	0.55	Fluctuates	0.55	Fluctuates

Table 5.   Dummy length variation, 3-1 dipole pair

The phase difference plots for all setting combinations cross each other and are only marginally different, thus contributing minimal error to the results of the selection for the lowest phase difference settings.

Between 20° to 28° scan angle and with a dummy separation of $0.55\lambda_o$, Figure 77 in Appendix B indicates that the two graphs for $0.45\lambda_o$ dummy length and $0.55\lambda_o$ dummy length have a phase difference of less than 1°. This suggests that $0.45\lambda_o$ will give good compensation even if it is used in the scan angle region of 20 to 28°. However, at scan angle of 50° or more, the $0.45\lambda_o$ dummy length does not compensate as well as any other dummy length and has a phase difference of 3.5° more than the best case. Therefore, the $0.45\lambda_o$ dummy length is not a good choice at wider scan angles.

b.   1-2 Dipole Pair

Table 6 shows that results below a scan angle of 15°. The best compensation setting is achieved when the dummy length is $0.45\lambda_o$ and dummy separation is $0.6\lambda_o$. Again the fluctuations between 15 to 30° are due to crossing between plots and the phase differences are only marginally different from each other.

Scan Angle	<15°	15°-30°	30°-47°	47°-53°	53°-80°	>80°
Dummy Length (λ_o)	0.45	Fluctuates	0.65	0.65	0.35	0.4
Dummy Separation (λ_o)	0.6	Fluctuates	0.45	0.65	0.45	0.3

Table 6.   Dummy length variation, 1-2 dipole pair

Although there are six regions of scan angle regions, the $0.45\lambda_o$ dummy length plot does not differ from the best by more than 3°. For example, at a scan angle of 45°, it differs from the best case by 2° while at a 90° scan angle the difference is 3°. Therefore, the acceptance of this error will depend on the tolerance of error in antenna application.

62

B. COMPENSATION NETWORK METHOD

1. General Checks

The building blocks of the compensation network have progressed to individual component testing. The stripline and coaxial line both achieve an impedance of about $50\,\Omega$, the desired characteristic impedance.

The hybrid ring attains scattering parameters predicted by theory. Reflection coefficients at individual ports are small; ports that are separated by half-wavelength have low transmission while ports with one-wavelength path difference have low losses.

In this design, the input impedance of the dipole may have a mismatch with the $100\,\Omega$ lines that are leading to its terminals. Appendix D reveals that operating frequency shifts from the design value of 7.5 GHz to about 8.6 GHz. Dipole impedance is controlled by the length and width of the arms and these are more sensitive to frequency than other components in the circuit are. The dimension of the dipole arms may have provided an input impedance of $70\,\Omega$ instead of $100\,\Omega$. Thus a $59.1\,\Omega$ quarter-wavelength transformer must be used instead of $70.7\,\Omega$ transformer and the lines that are connected to the dipole terminals should have a characteristics impedance of $70\,\Omega$. Nevertheless, the exact frequency of operation is not of importance in this study and no effort will be devoted to redesign for 7.5 GHz.

2. Fabricated Single Dipole Antenna plus Hybrid Ring

a. Fabrication

Circuits were fabricated by a commercial etching facility. The *CST* geometry files in *ACIS* format were converted to *DXF* format using *AutoCad*. The circuits were printed on Rogers R4003 material (double sided one-ounce copper cladding). Final trimming was performed on the prototypes, and the scattering parameters were measured on the VNA.

b. Scattering Parameters from Network Analyzer

The scattering parameters were measured after some trimming was performed on the traces. More capacitance and less resistance are generally required at both ports, as the uncorrected impedances tended to be inductive. All scattering

parameters were lower than –15 dB. The scattering parameters were optimized for 7.895 GHz instead of 8.7 GHz because the initial scattering parameters at the design frequency of 8.7 GHz were too high and the circuit could not be tuned sufficiently at this frequency.

c.   *Antenna Element Pattern*

The antenna pattern was measured in the *NPS* anechoic chamber in *Spanagel Hall*. Both *E* and *H* plane patterns were made with either port 1 or port 2 active, with the other port loaded.

Element patterns shown between Figure 36 and Figure 38 for the individual dipoles when the difference-ports are terminated with matched loads produced the required patterns, as predicted by theory. The 3-dB beamwidth of the antenna pattern was about the same value (70°) as the simulation in *CST*, using a half-wavelength dipole as demonstrated in Figure 40.

When the input ports are terminated with matched loads and the difference signal is received, the patterns obtained differ from those in Figure 44.   due to the presence of the finite ground plane, which introduces edge diffraction discussed in [Ref. 1]. The ground plane causes a drop in received signal at the difference-port when the scan angle is about 70°. To derive this angle quantitatively, image theory and edge diffraction have to be applied.

As the scan angle increases, the microstrip feeding the dipole arms becomes visible and acts as an antenna. Because its dimension is comparable to the dipole arm, the received signals at $\pm 90°$ have values close to those for broadside. To alleviate this problem, the dipole card must be completely shielded as shown in Figure 47. Despite this effort, there is still a small section of microstrip (about a dipole arm length) leading to the arms that is still exposed and it will affect the patterns at $\pm 90°$.

Back (Covered by Radar
Absorbing Material)

Exposed copper
traces

Dipole placed
$0.15\lambda_o$ above
ground plane

Radar
Absorbing
Material to
cover the
rest of the
dipole
circuits
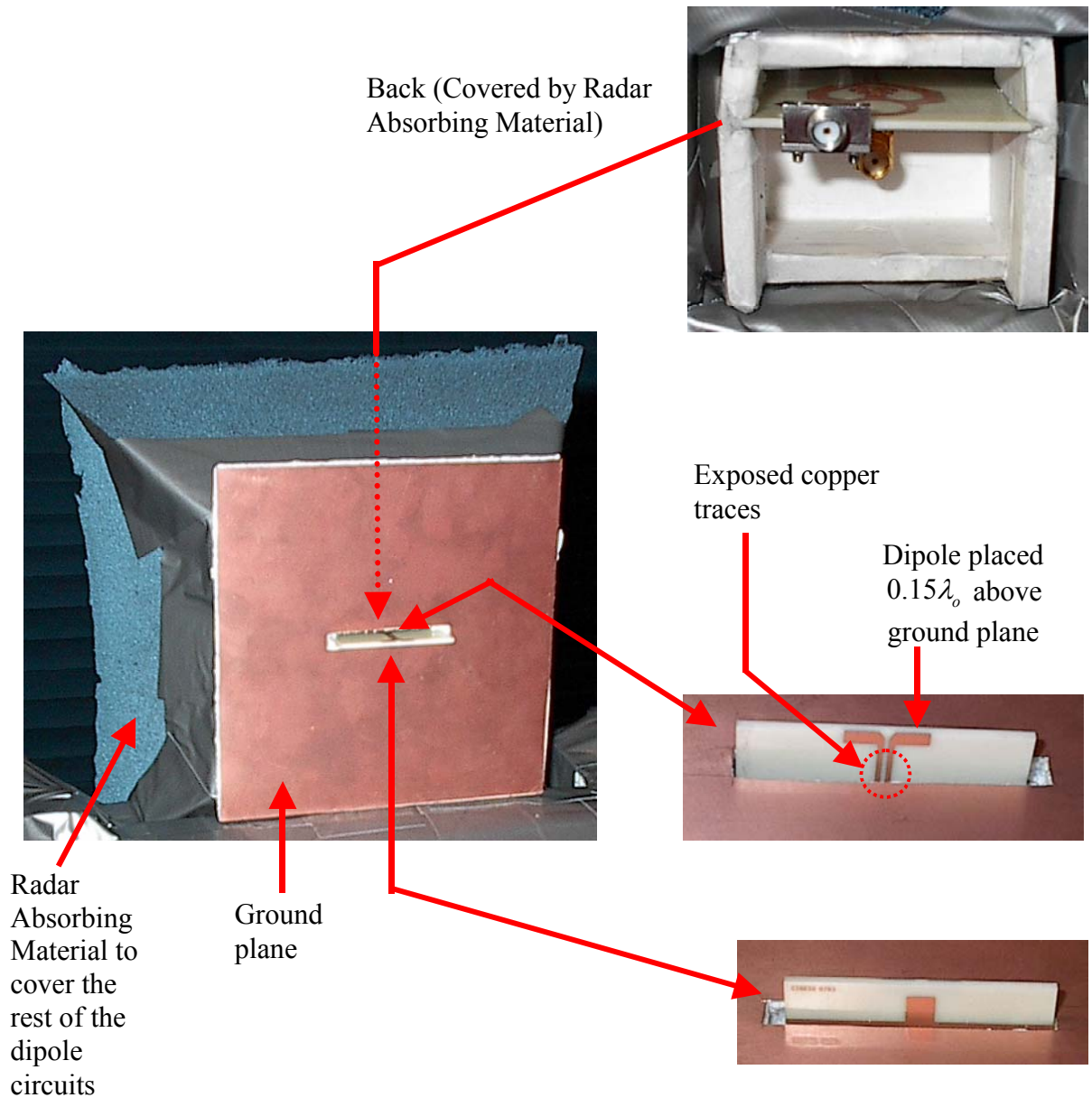
Ground
plane

Figure 47.   Dipole with ground plane on turn-table (front view)

THIS PAGE INTENTIONALLY LEFT BLANK

V.   FUTURE WORK

A.   DUMMY ELEMENT COMPENSATION METHOD

1.   Two-Dummies Configuration

Instead of using one dummy element at each end, an additional element can be used to further reduce the edge effect. The layout with $0.6\,\lambda_o$ separations for both d_1 and d_2 is shown in Figure 48.
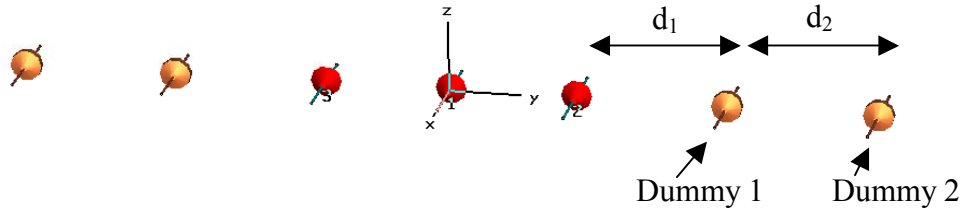
Figure 48.   Two-dummy elements layout

Preliminary simulation results are shown by the red lines in Figure 49. The load terminating each dummy is $1\,\Omega$. At broadside, the two-dummy configuration does not provide better phase error than the one-dummy configuration, however it is 2° better than the one-dummy configuration when the scan angle increases beyond 60°. This is an advantage especially at higher scan angles. Further exploration may be conducted by a parametric study that varies both d_1 and d_2 to find a combination that results in the lowest phase difference. It is unlikely, however, that the small reduction in phase error provided by the additional dummies would be worth the additional hardware and size required. In fact, most arrays will not scan beyond 45° or so from broadside, so improvements in this range are not applicable.

2.   Infinite Array Comparison

There is a need to compare dipole voltages generated by the dummy element compensation method to the three center elements in an infinite phased array, and strive for a compensated small array to achieve Equation (23) performance. To this end, the infinite array should be simulated. The arrangement is shown in Figure 50. N is odd as explained before. Software with periodic boundary conditions can simulate the radiation and impedance for infinite arrays. The *CST* has such feature and will support this study.

67
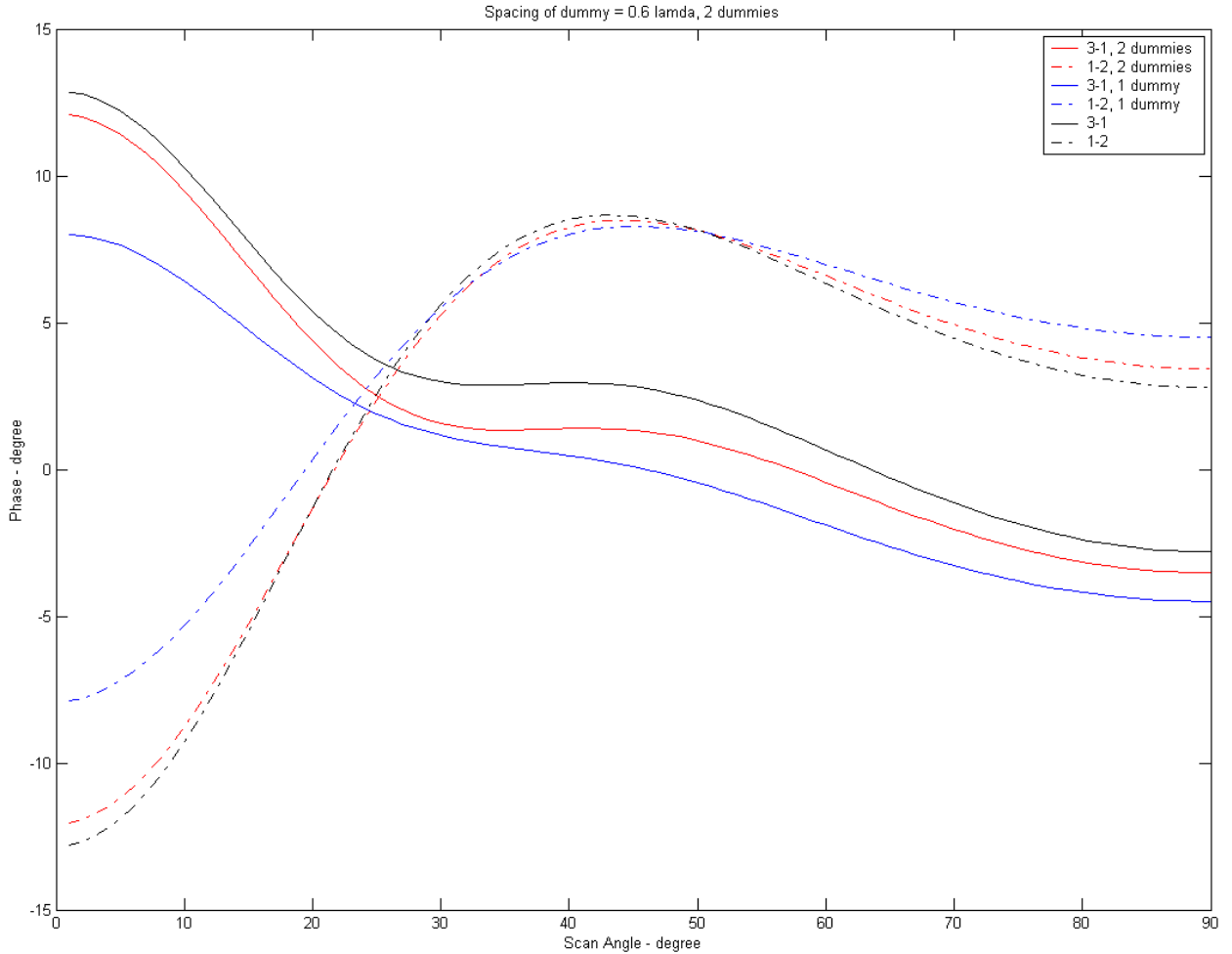
Figure 49. Two dummy elements phase difference
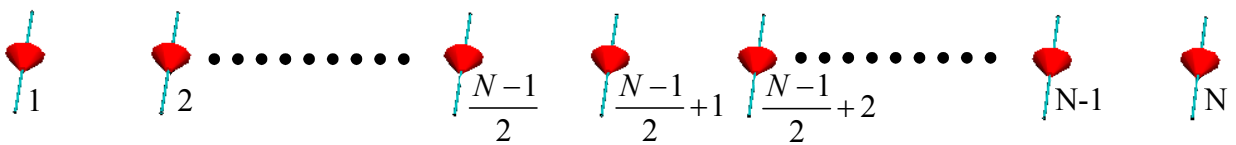
Figure 50. Infinite phased array

3. Dummy Element Topology

Another variant is to place a number of dummy elements around the active dipole elements as shown in Figure 51. The phase difference is compared to the 1Ω case in Figure 52. The phase error is worse than the uncompensated case at broadside but improves as the scan angle is increased. Similar to the two-dummies configuration, the compensation is better than the 1Ω case at scan angles that are greater than about 60°.

Since some improvements of about 2° have been observed, it may warrant further investigation to ascertain whether or not certain dummy arrangements may achieve improvements over the whole range of scan angles.

Dummies (Brown Colored)

Active Dipoles (Cyan Colored)
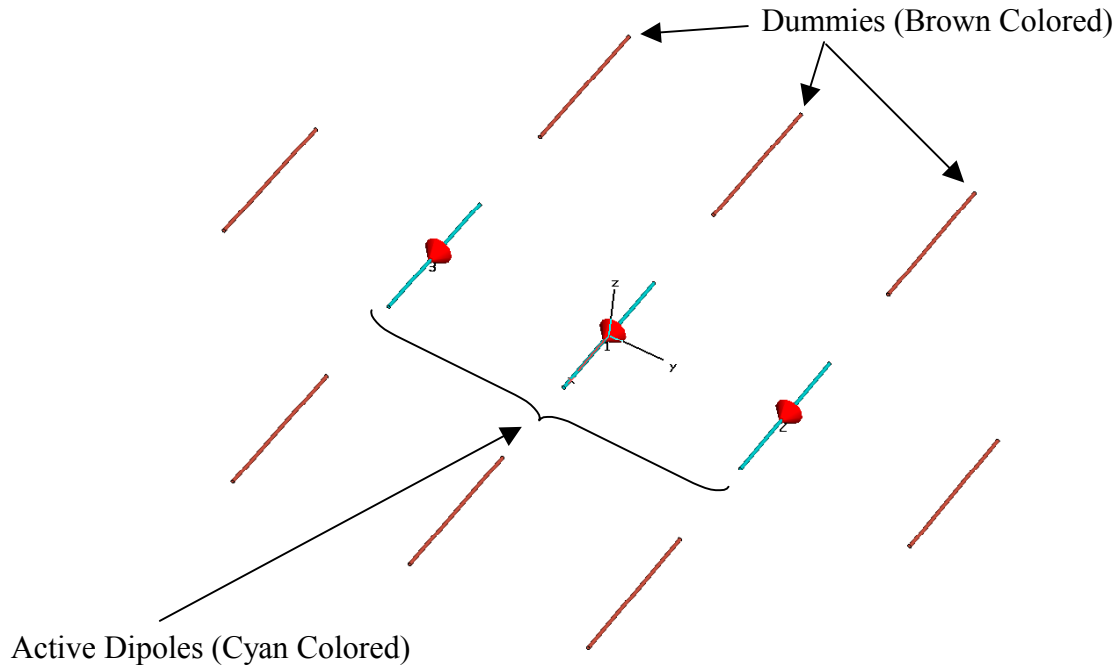
Figure 51.   Dummy configurations – new topology

The performance advantage of using more dummies has to be weighed against the use of active dipoles since both occupy large space on the platform.   With so many dummy elements, the size advantages of a small array are lost.

B.   COMPENSATION NETWORK METHOD

1.   Difference-Port Pattern

The voltage magnitude at the difference-port is used to modify the amount of mutual coupling and it is based on the phase difference of the wave incident on the two arms of the dipole. The phase difference of the incident wave arriving at the dipole arms is a function of the scan angle as well as the polarization mismatch between the incident wave and the dipole.
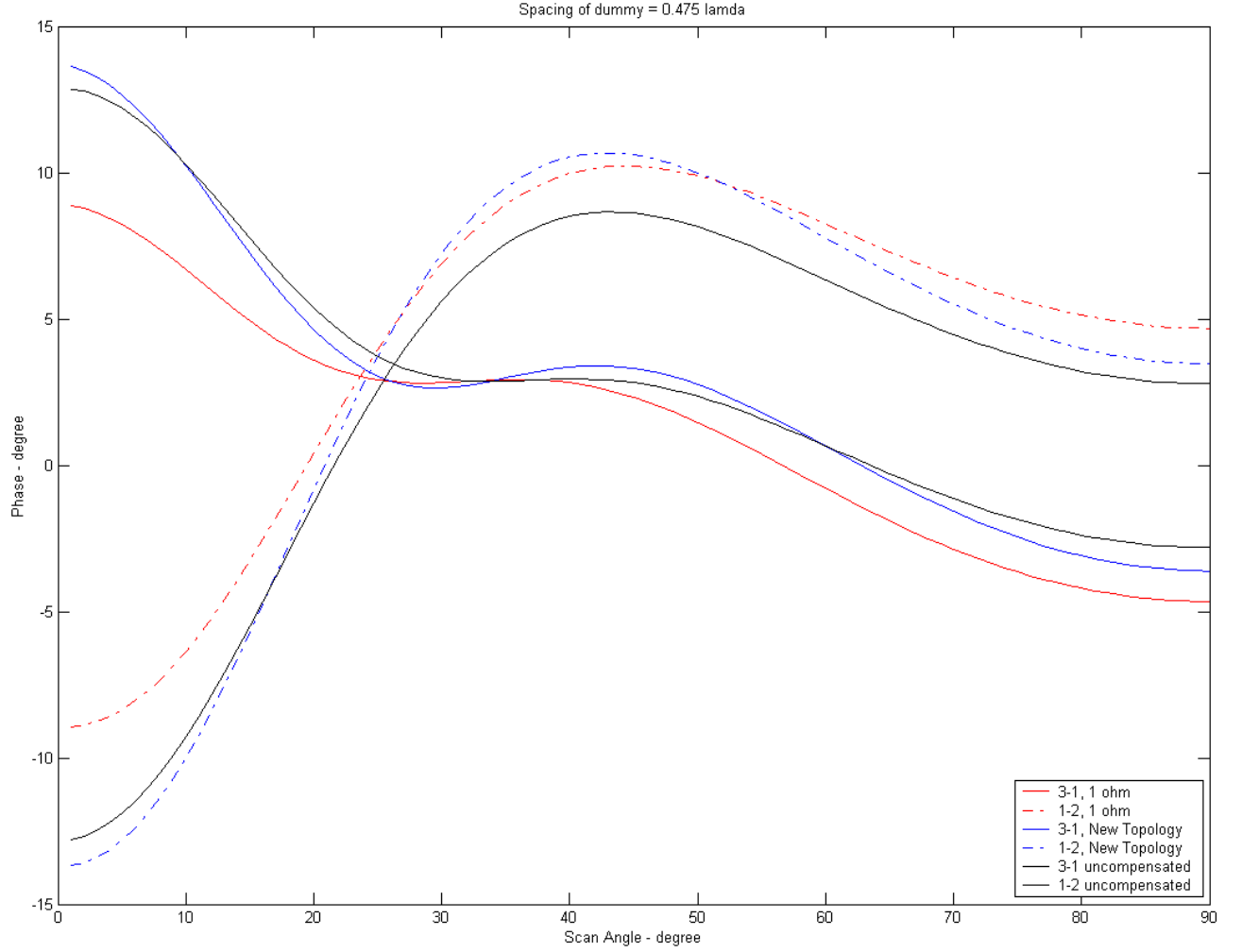
Figure 52.   New dummy topology result

The measurements conducted have thus far assumed that the electric field vectors are in the same plane as the dipole elements. However, this is untrue in real applications as waves may be incident on the dipole element from other planes. The amount of electric field inducing the dipole, and hence the voltage magnitude received at the difference-port of the hybrid ring, will be reduced. An example of this situation is shown in Figure 53. A TEM wave approaching in the $\phi_i = 0$ plane will induce voltages on both arms of the dipole,

$$V_{1,\theta_S=0} = \int_l \vec{E}_{i1} \bullet \vec{\ell} d\vec{l} = \int_l \left|\vec{E}_{i1}\right|\left|\vec{\ell}\right| \cos\theta dl \text{ and} \tag{25}$$

$$V_{2,\theta_S=0} = -\int_l \vec{E}_{i1} \bullet \vec{\ell} d\vec{l} = -\int_l \left|\vec{E}_{i1}\right|\left|\vec{\ell}\right| \cos\theta dl \tag{26}$$

and this is the usual case that we will assume. For incidence in a diagonal plane ($\phi_i = \phi_s$), the voltages generated at the dipole will be

$$V_{1,\theta_S \neq 0} = \int_l \left|\vec{E}_{i2}\right|\left|\vec{\ell}\right|\cos\theta\sin\phi_S dl \text{ and}$$ (27)

$$V_{2,\theta_S \neq 0} = -\int_l \left|\vec{E}_{i2}\right|\left|\vec{\ell}\right|\cos\theta\sin\phi_S dl \text{ .}$$ (28)

Therefore, for the same elevation angle θ, $V_{1,\theta_S=0} + V_{2,\theta_S=0}$ will be larger than $V_{1,\theta_S \neq 0} + V_{2,\theta_S \neq 0}$. This will in turn produce a smaller output at the difference-port when $\phi_i \neq 0$, thus reducing the signal available for compensation.

More work must be conducted to predict the exact theoretical shape of the signal at the difference-port versus the scan angle of the radiation. This includes the total understanding of how a signal is generated at the difference-port especially with the presence of the ground plane at $0.15\lambda_o$ below the dipole arms and the additional voltage induced at the microstrip feed line. This is critical as the difference power will be for feedback to the compensation circuit to determine the "level" of compensation required to cancel the mutual coupling.
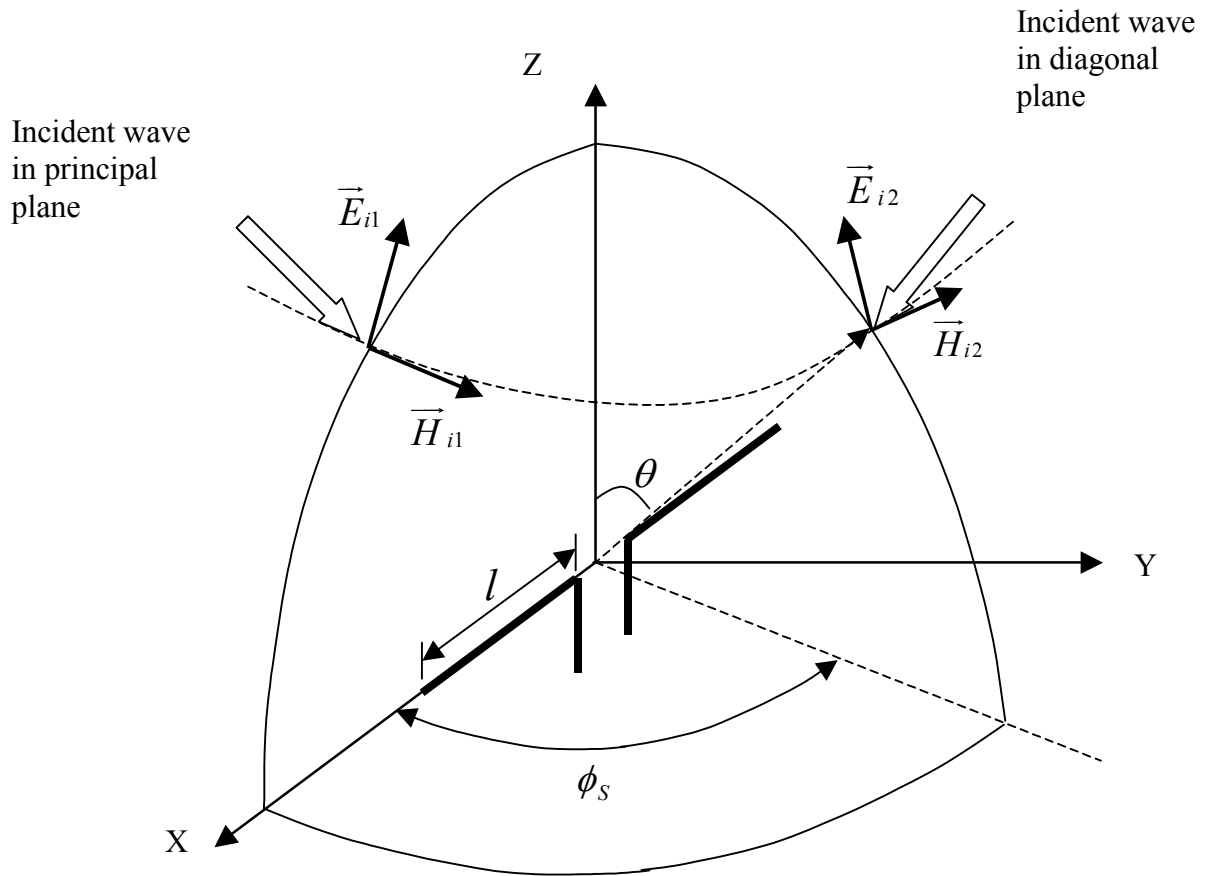
Figure 53. Effect of oblique incident wave

2. Feedback Network Configurations

One possible way of using the difference-port in a three-element array was shown previously in Figure 8. The power generated at all difference-ports are weighted and combined to form the feedback signal that will adjust the inputs to the three dipole elements. A more comprehensive method may include using signals from the difference-ports to individually control the inputs to the dipoles. The circuit will be more complex but offers higher flexibility in the control loops as shown in Figure 54 and Figure 55.
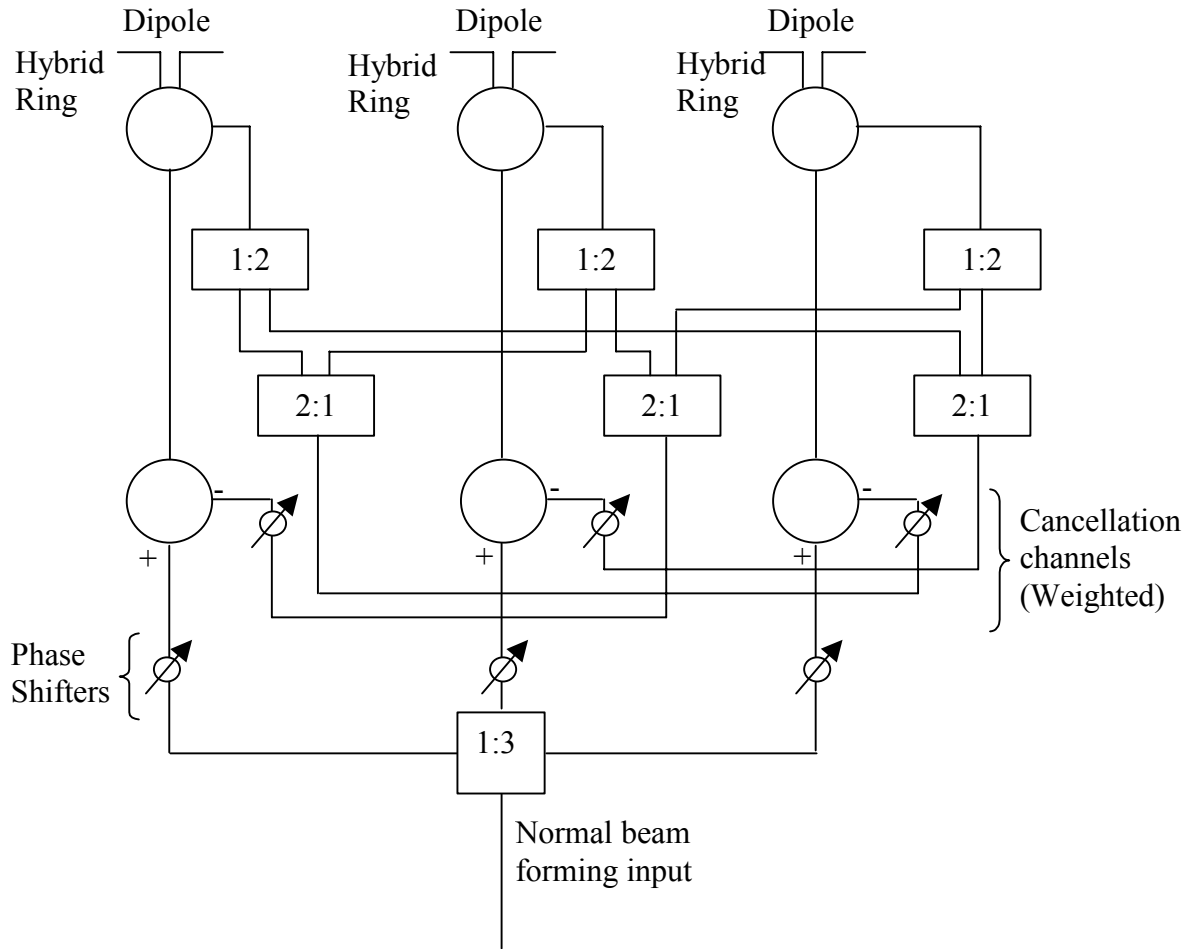
Figure 54.   Compensation circuit layout 1

In both layouts, the difference-port signal is interlinked between the three dipole inputs. This ensures that the two dipoles that are receiving the interference (assuming only first order interference) are used to correct the phase of the dipole that is causing the interference.

In layout 1, weights are applied only after two difference signals from two dipoles are combined while in layout 2, these are applied before the combinations. The application of weights before combining the difference signals increases the hardware but it allows more flexibility in the tuning of the feedback signals.
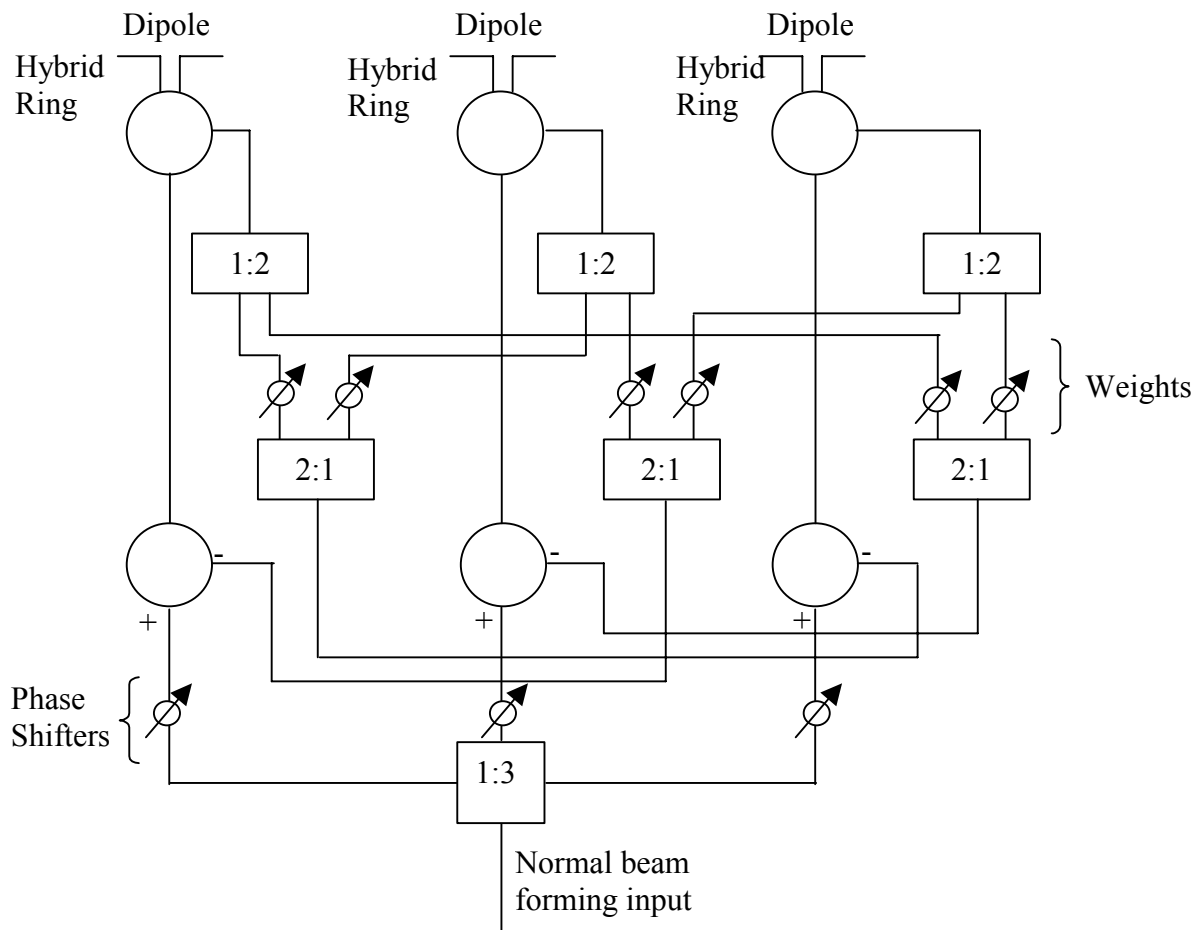
Figure 55.   Compensation circuit layout 2

VI. CONCLUSIONS

Two methods of mutual coupling compensation were investigated. The first was to add dummy elements at the array edges thereby reducing the edge effect for the active dipoles. The second approach was to introduce a cancellation signal to correct for changes in mutual coupling as the incident wave direction changes. The second method requires a two port array element or an auxiliary antenna to provide the cancellation signal. The research effort focused on the development of a hybrid ring fed dipole that has a difference port that can be connected to a feedback or cancellation network.

The dummy element compensation method was able to bring the difference between the theoretical plane wave phase and the actual phase to about 8° at broadside. The phase errors for both 1-2 and 3-1 dipole pairs reduced quickly to less than 5° when the scan angle is increased to about 10°. However, there is a need to vary the dummy separation distance, load terminating the dummy or even the dummy length in order to achieve this accuracy for the remaining scan angles. The objective is to optimize the dummy parameters for the scan angle of interest, which varies from application to application. The additional hardware requirements to achieve such a small incremental gain in accuracy may not be justified. On the other hand, the dummy separation method can be a quick and easy method to smooth the edge effect and provide a small improvement in array performance.

Several steps were taken in the design and demonstration of the cancellation approach. A two-port ring dipole was designed and fabricated. The initial design was done using *CST Microwave Studio*. The final design tuning was done with prototype boards. The final design had return losses greater than 15 dB and isolation between the two ports was also greater than 15 dB. Antenna patterns were also measured for the prototypes.

Future work will involve the design, simulation and demonstration of a three-element cancellation array. Several cancellation concepts were presented in Chapter V.

The ring dipole has other potential applications in addition to the mutual coupling compensation. The difference port provides an element pattern with a null in the *E*-plane.

The element could be used in a monopulse antenna, however, there is a limitation on how narrow the difference pattern "notch" can be. Another possible application is coherent sidelobe cancellation. Both of these applications will be investigated in future programs.

APPENDIX

A.   VARIATION OF LOAD TO DUMMY ELEMENT WHILE VARYING DUMMY DISTANCE
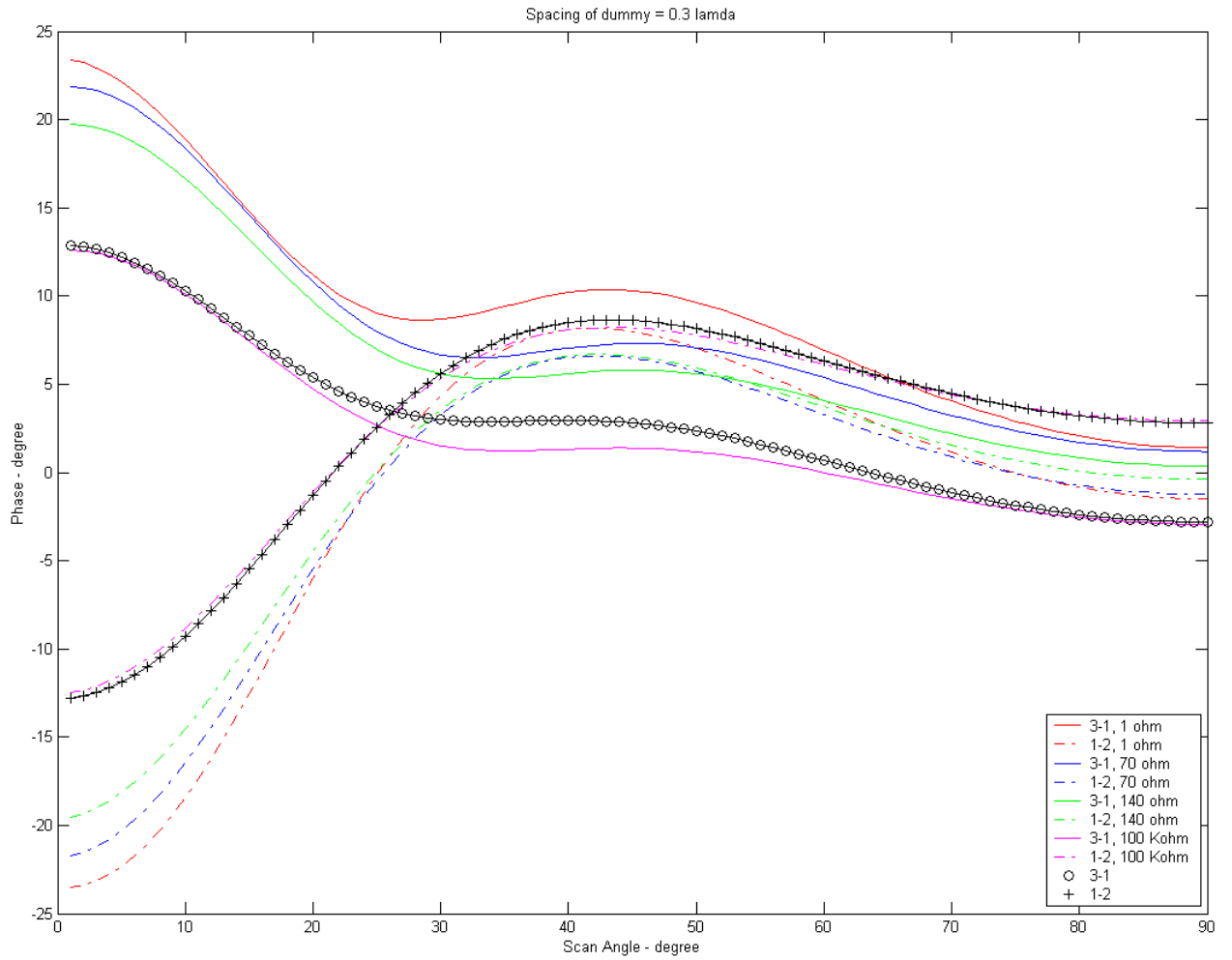
Figure 56.   Dummy separation variation: distance 0.3 λ_o
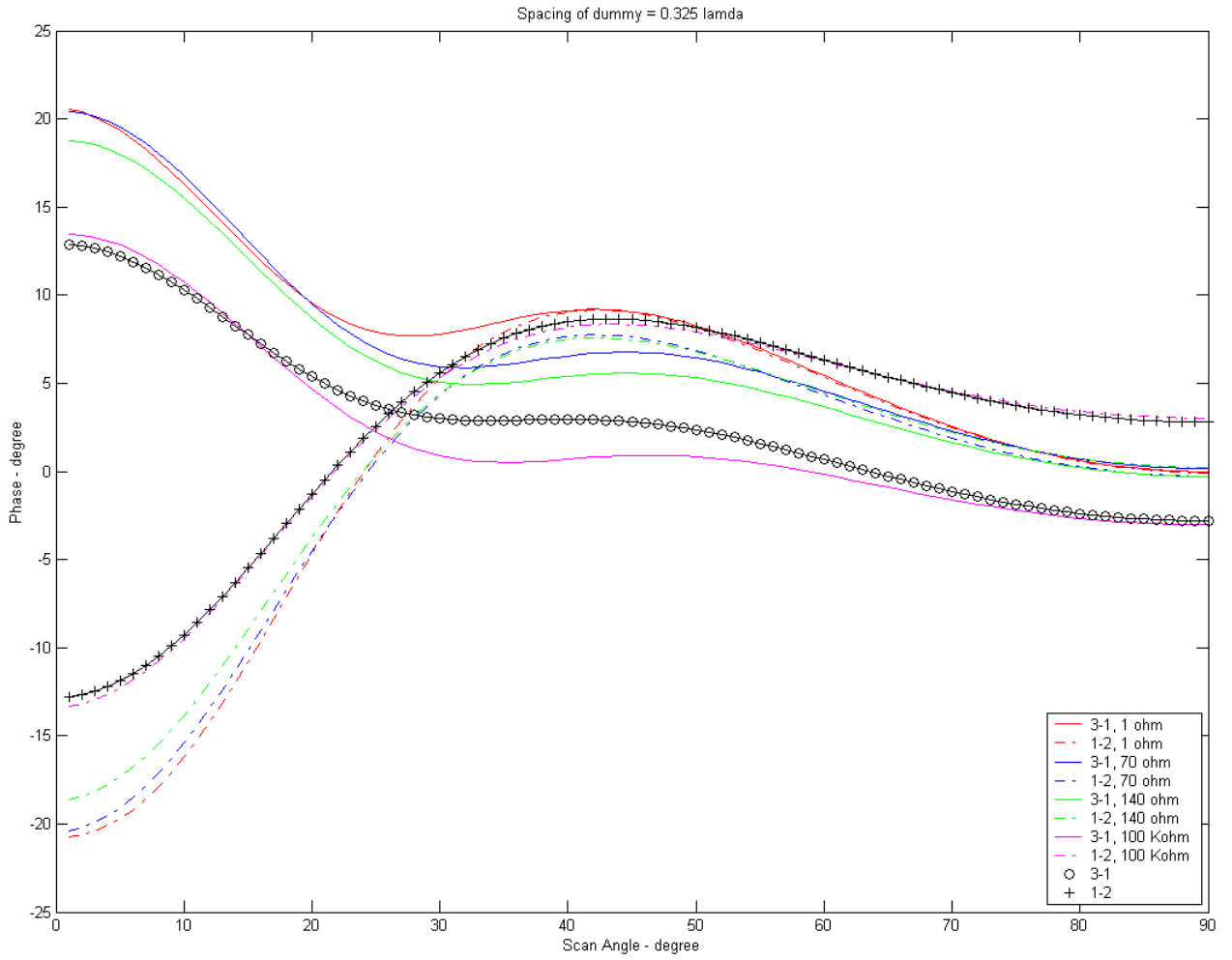
Figure 57.   Dummy separation variation: distance 0.325 λ_o
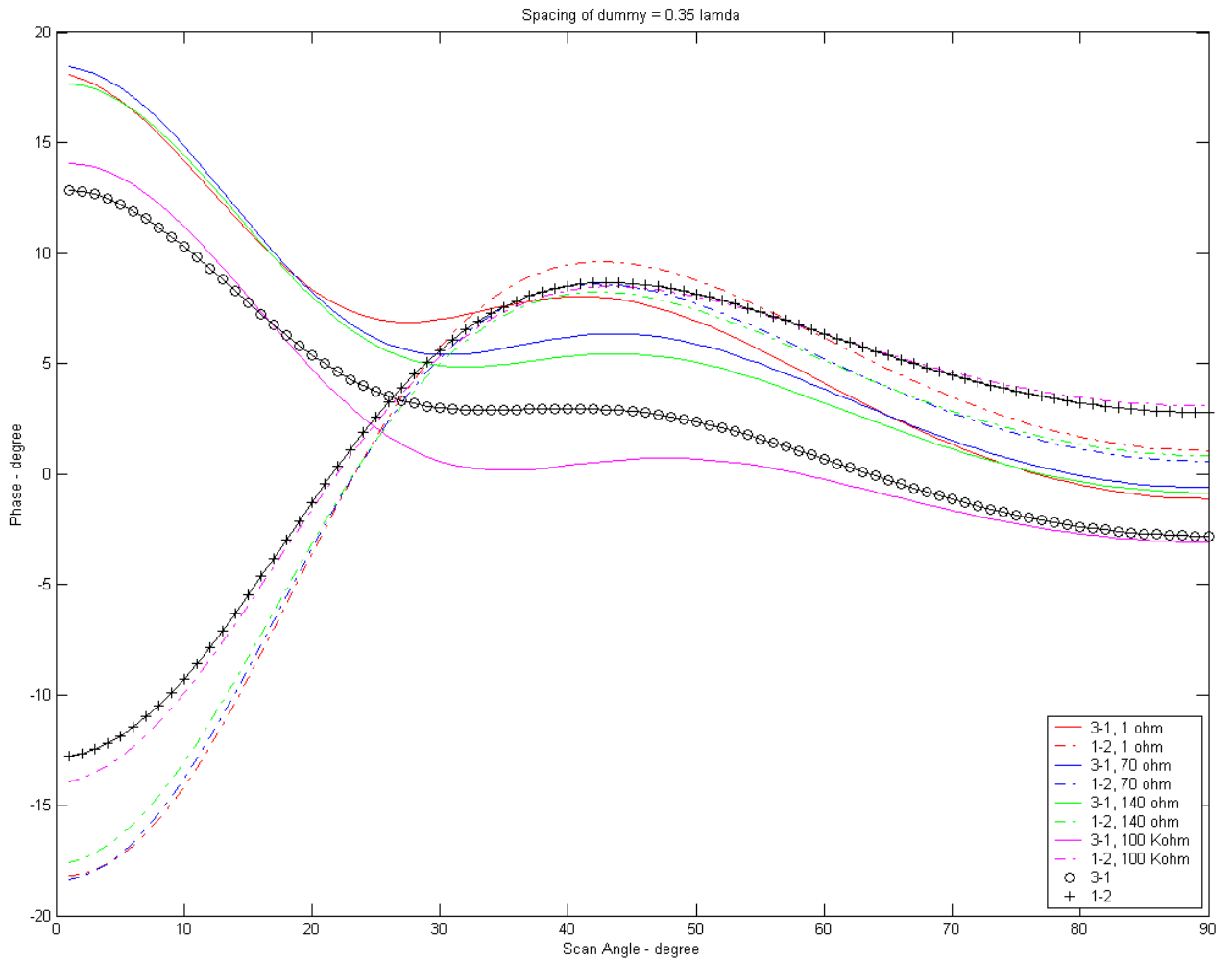
Figure 58.   Dummy separation variation: distance $0.35\,\lambda_o$
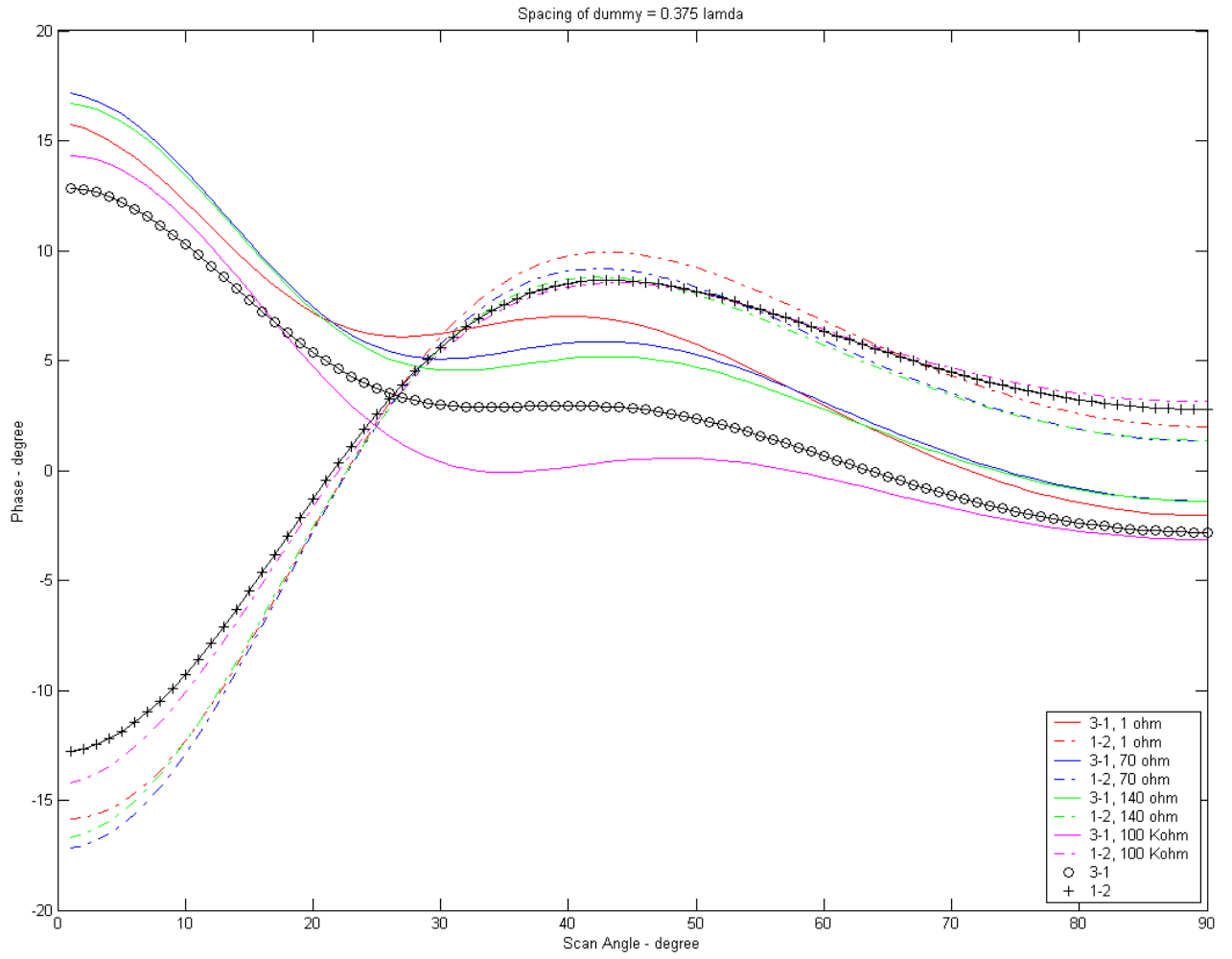
Figure 59.　Dummy separation variation: distance $0.375\,\lambda_o$
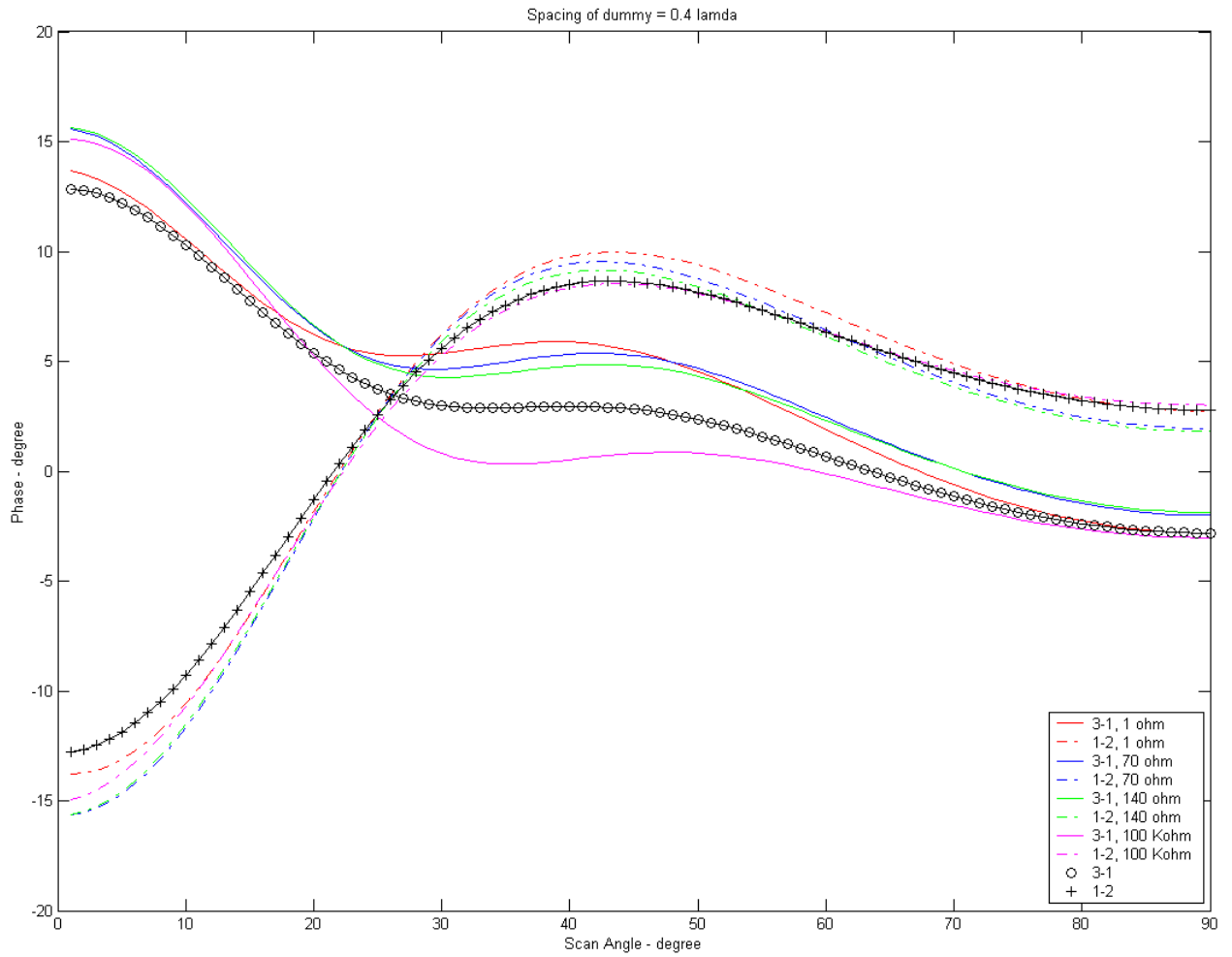
Figure 60.   Dummy separation variation: distance $0.4\,\lambda_o$
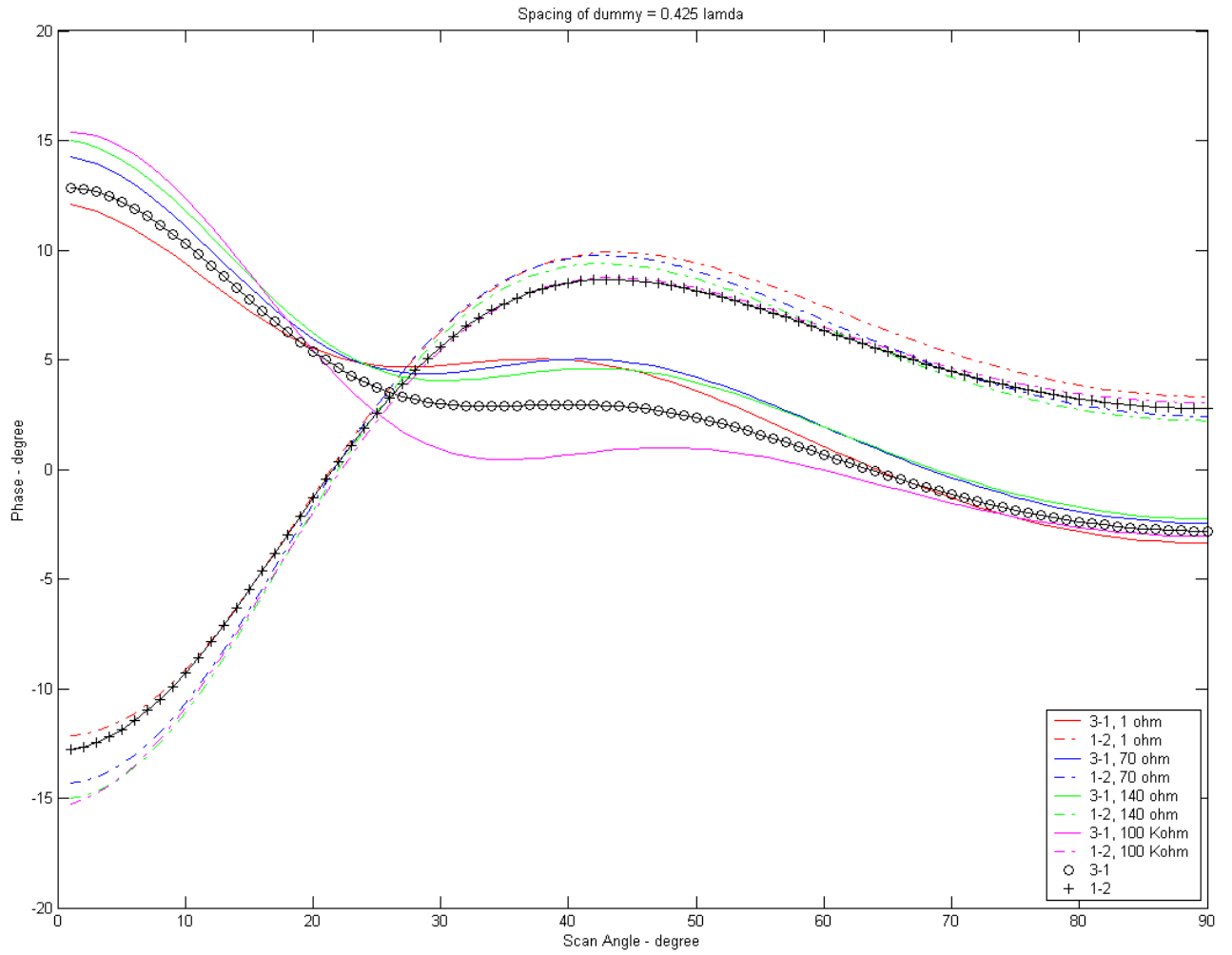
Figure 61.   Dummy separation variation: distance 0.425 λ_o
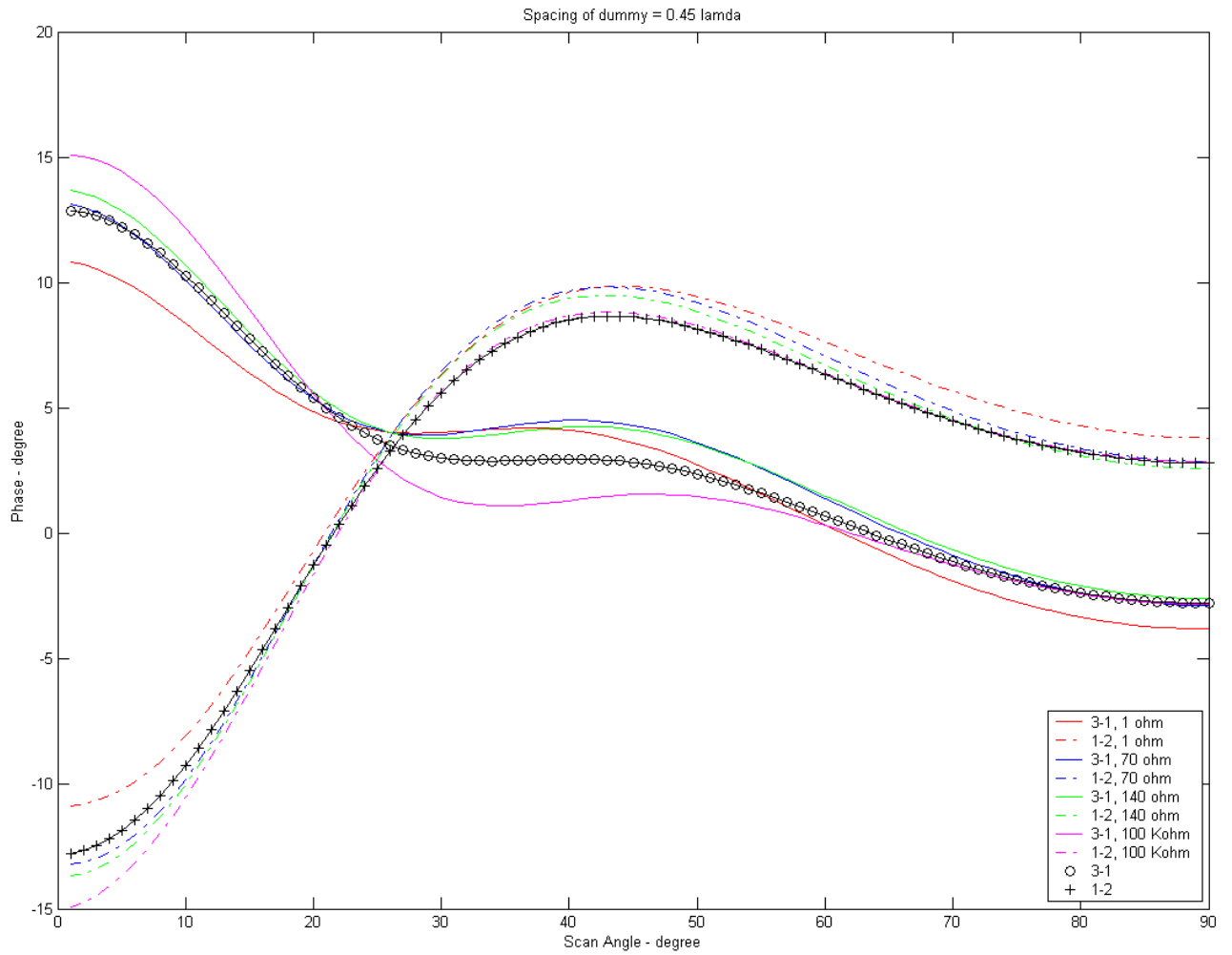
Figure 62.   Dummy separation variation: distance 0.45 λ_o
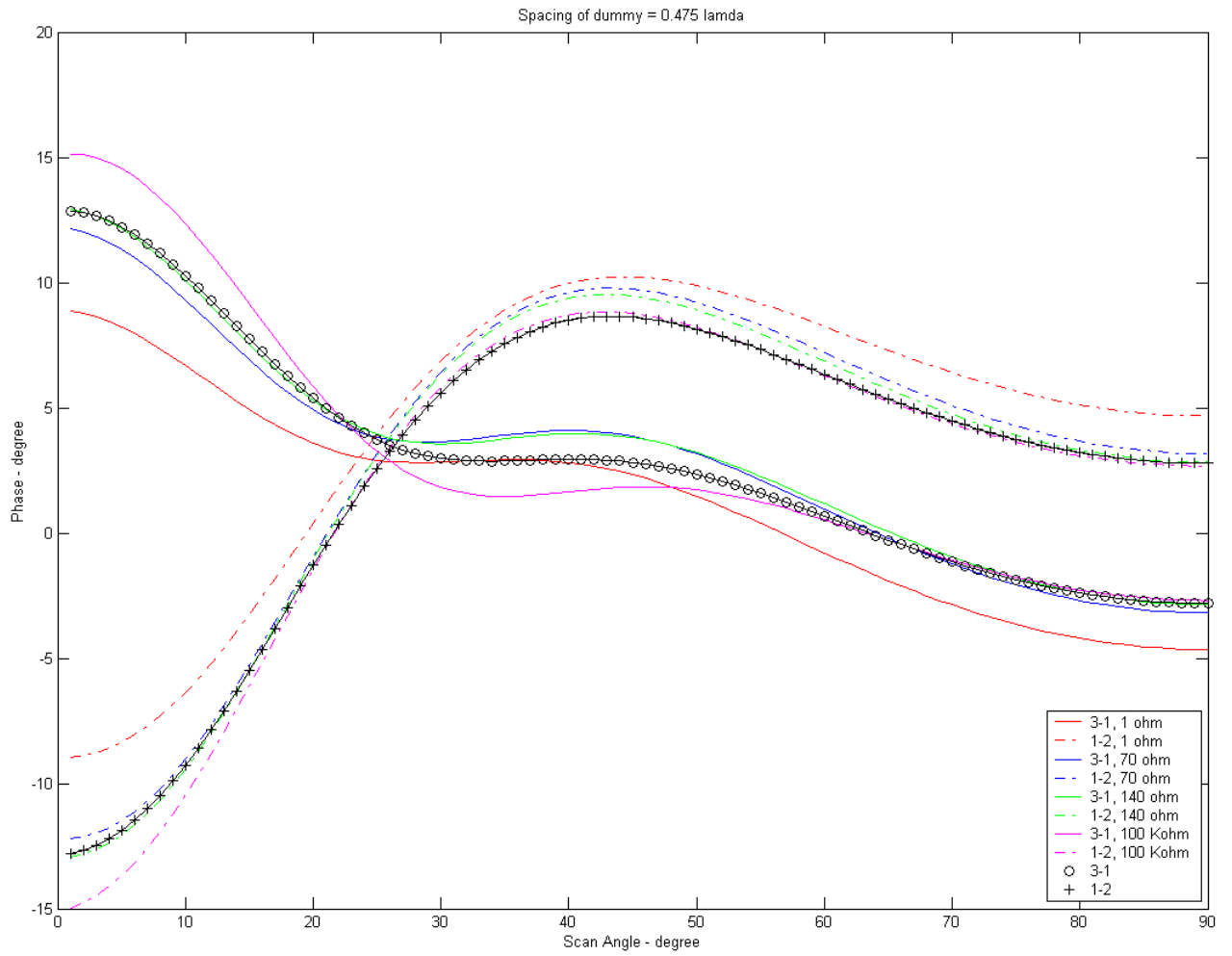
Figure 63.   Dummy separation variation: distance 0.475 λ_o
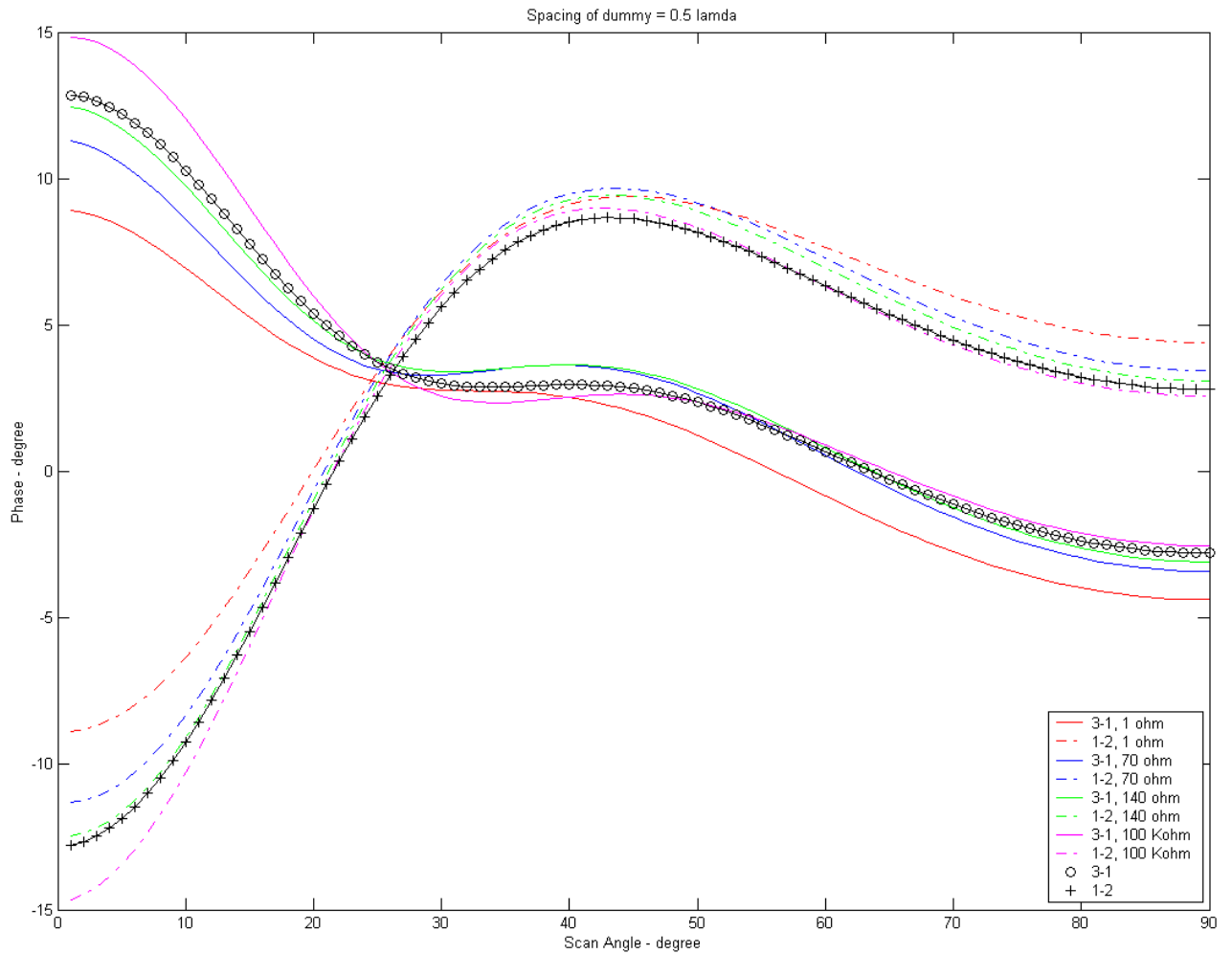
Figure 64.   Dummy separation variation: distance 0.5 λ_o
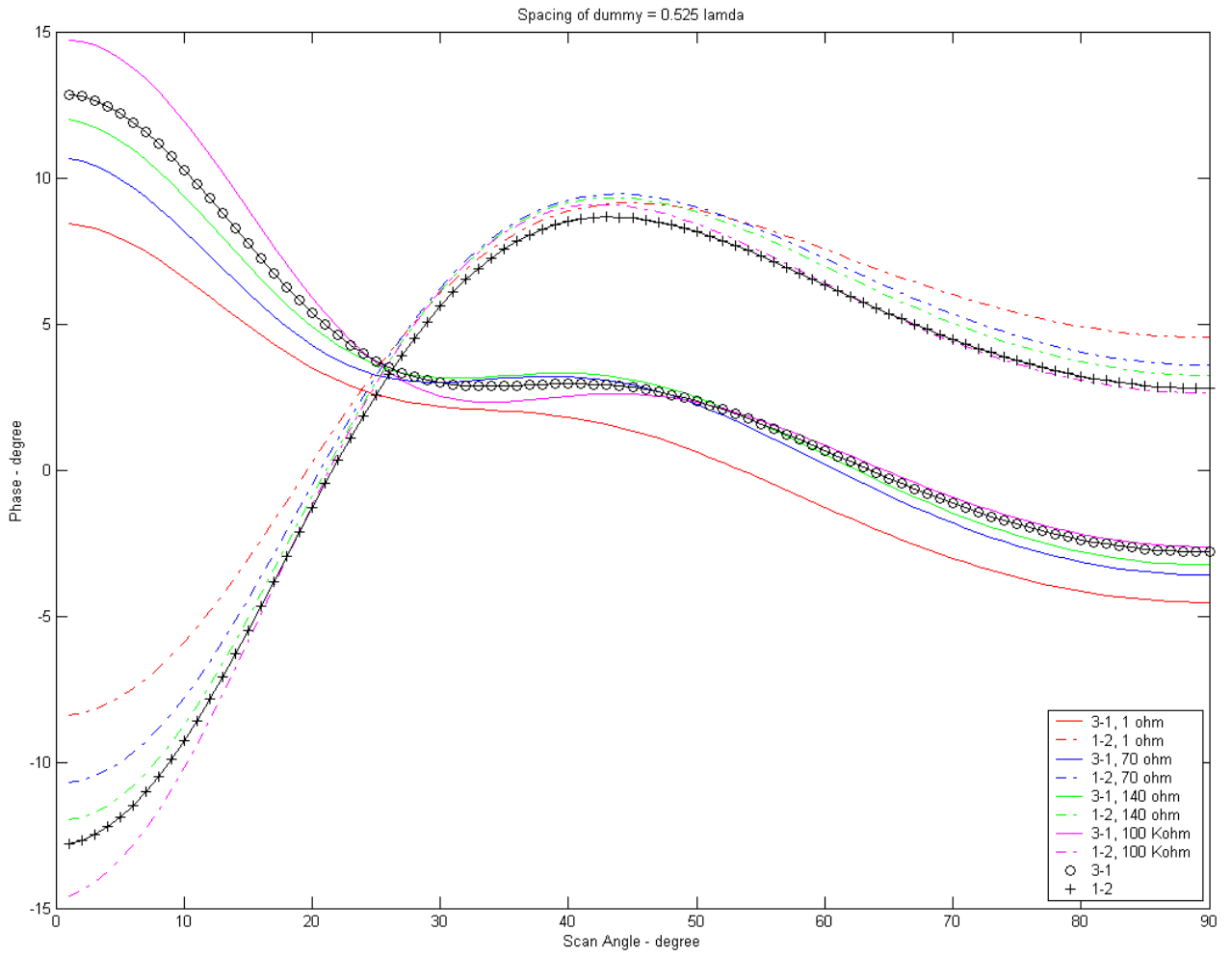
Figure 65.   Dummy separation variation: distance 0.525 λ_o
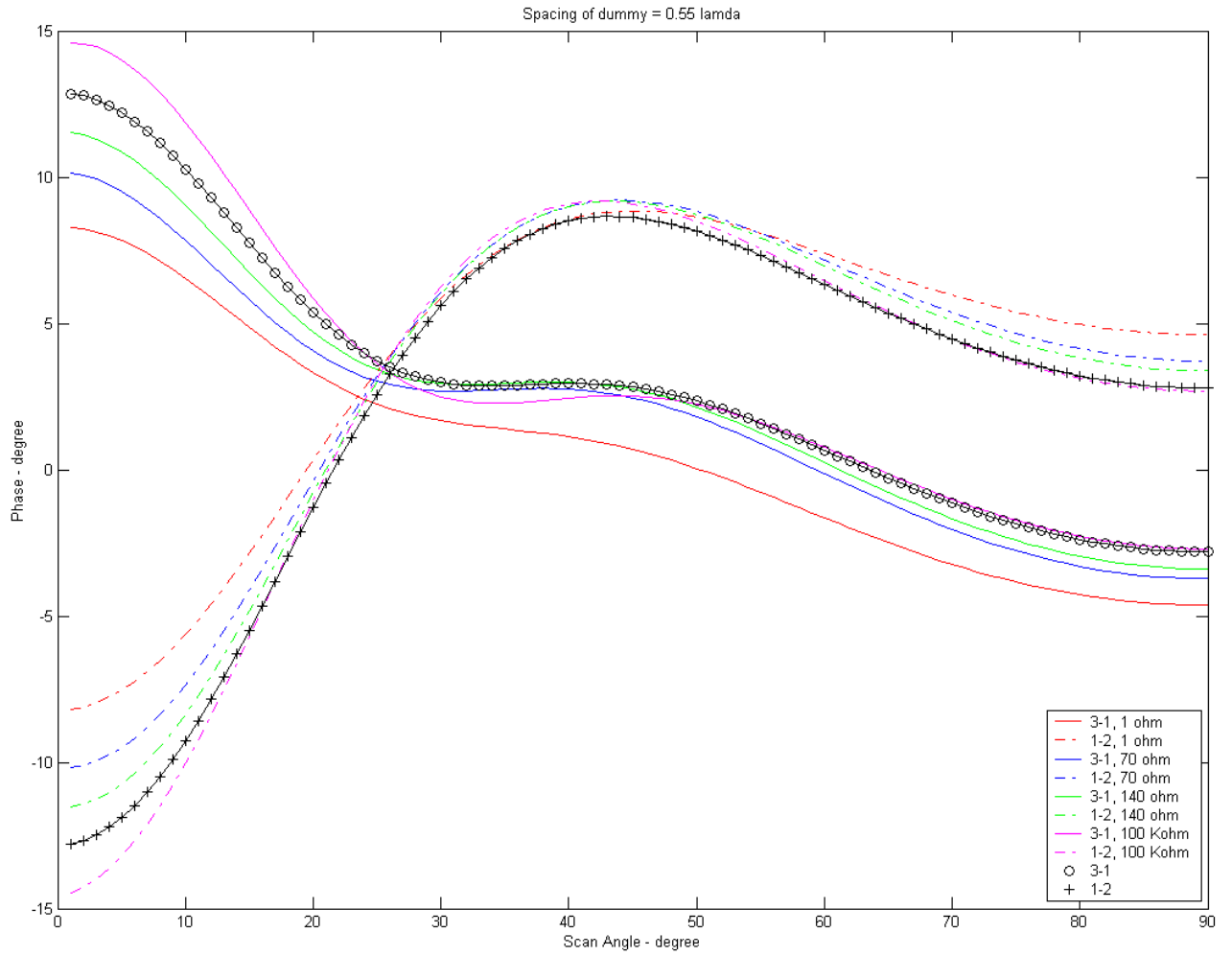
Figure 66. Dummy separation variation: distance 0.55 λ_o
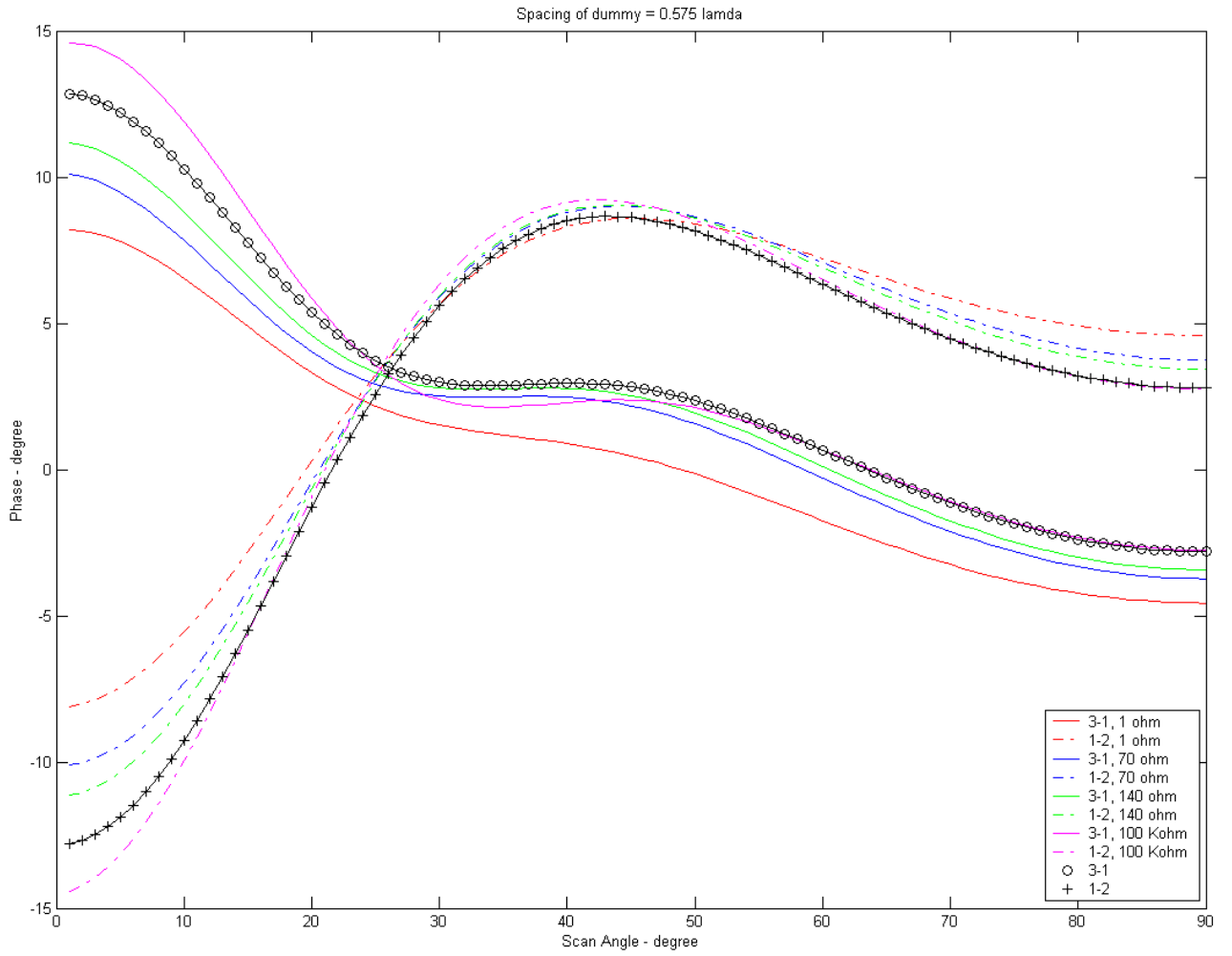
Figure 67.   Dummy separation variation: distance 0.575 λ_o
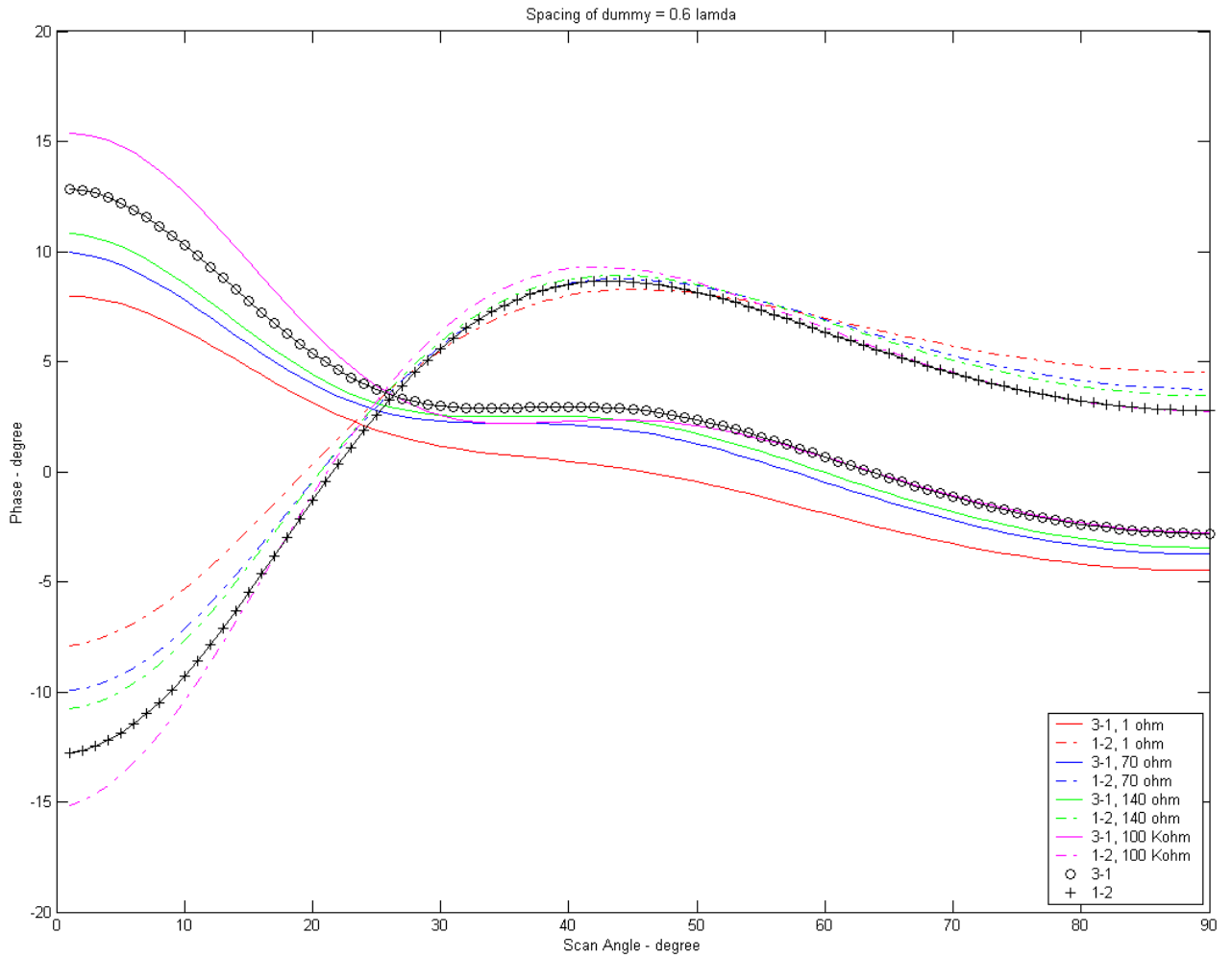
Figure 68. Dummy separation variation: distance $0.6\,\lambda_o$

89
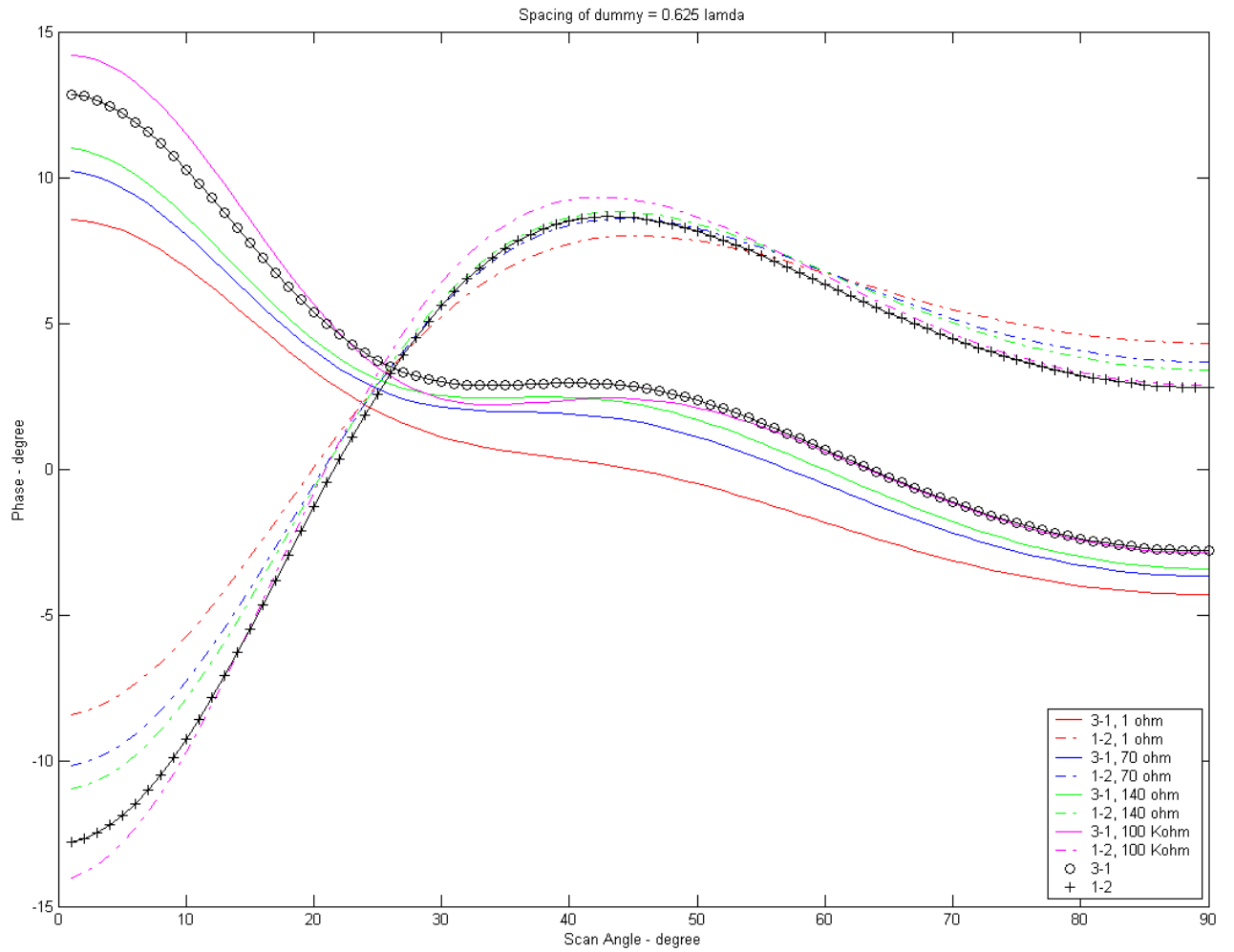
Figure 69.   Dummy separation variation: distance $0.625\,\lambda_o$
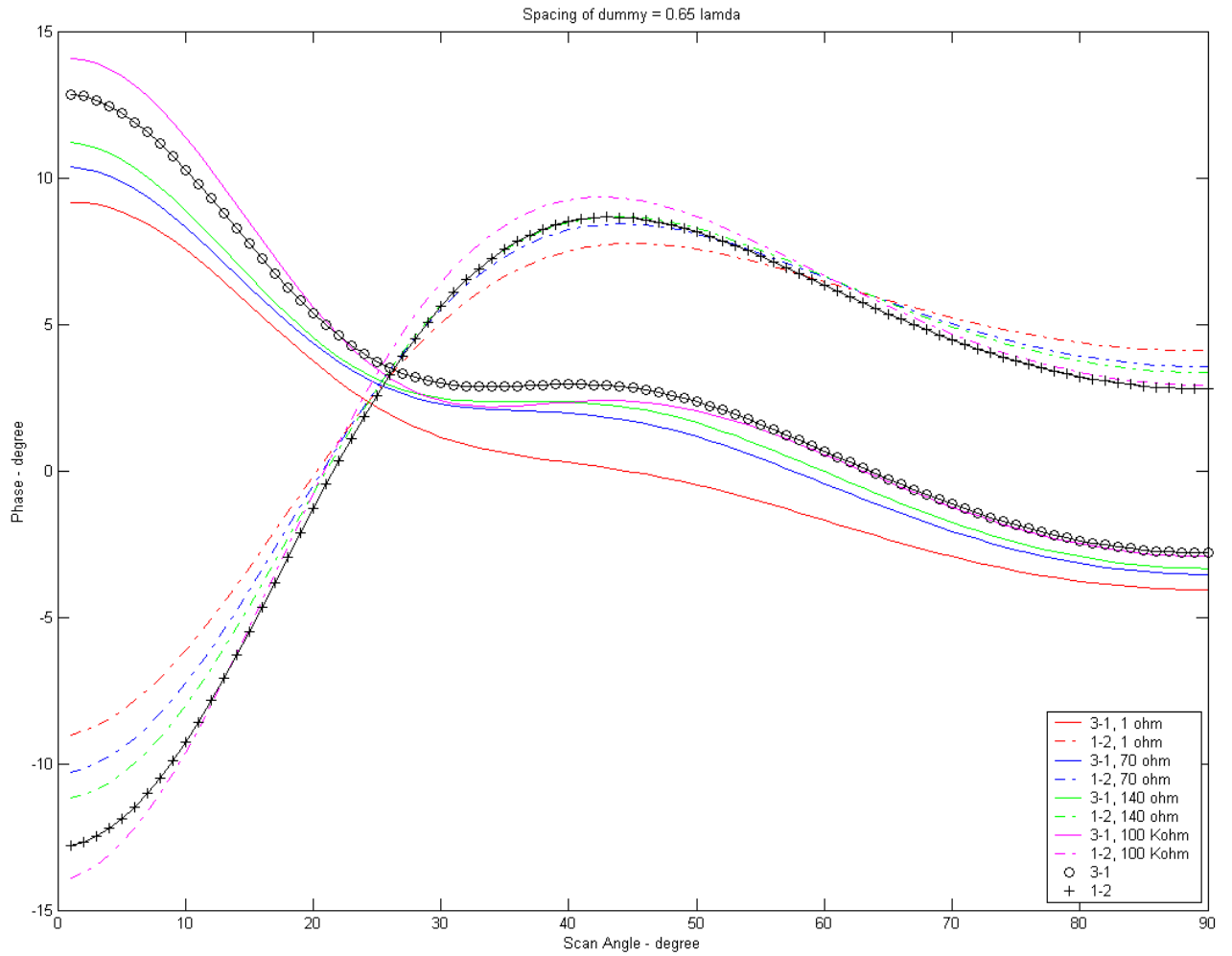
Figure 70.   Dummy separation variation: distance $0.65 \lambda_o$
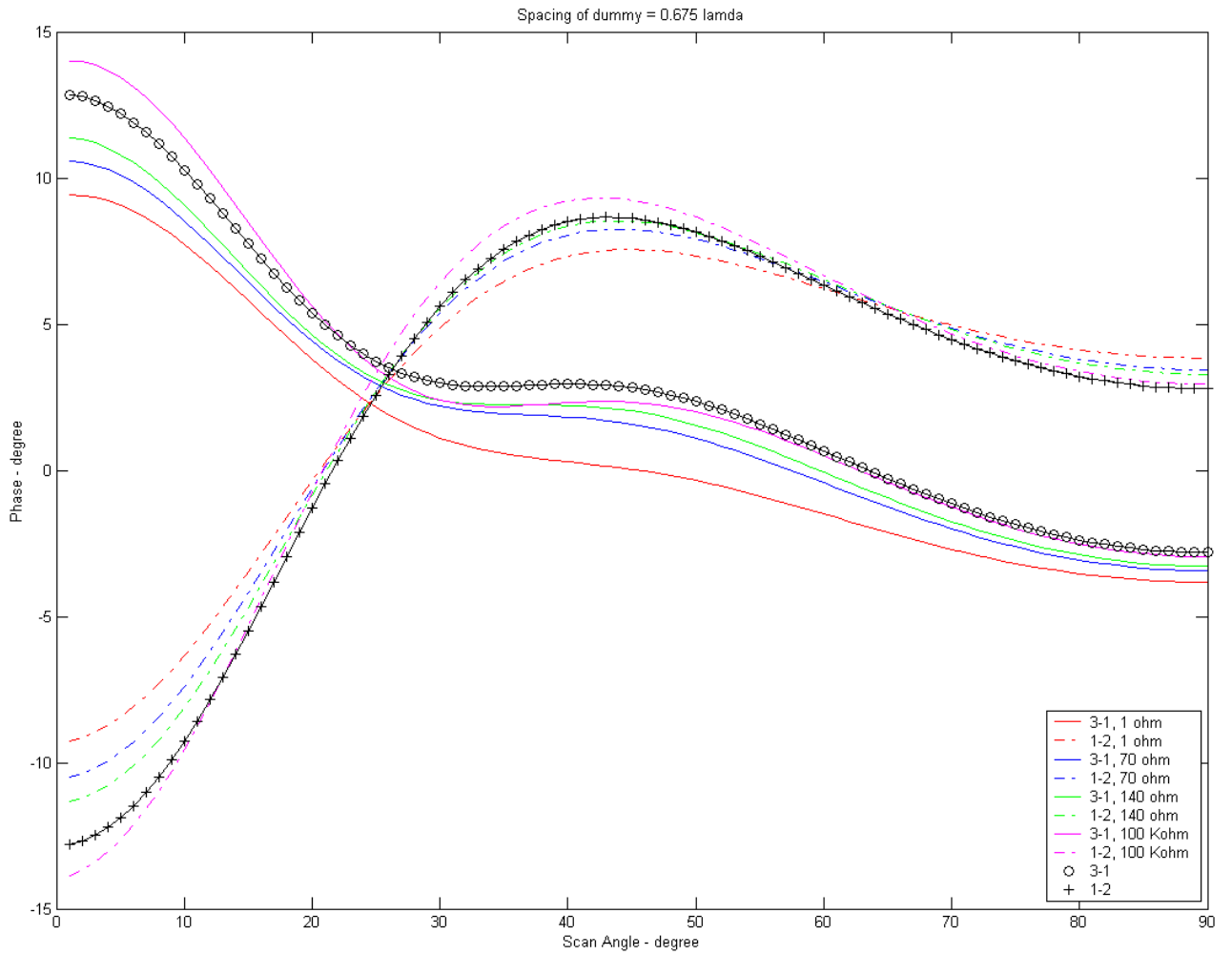
Figure 71. Dummy separation variation: distance 0.675 λ_o
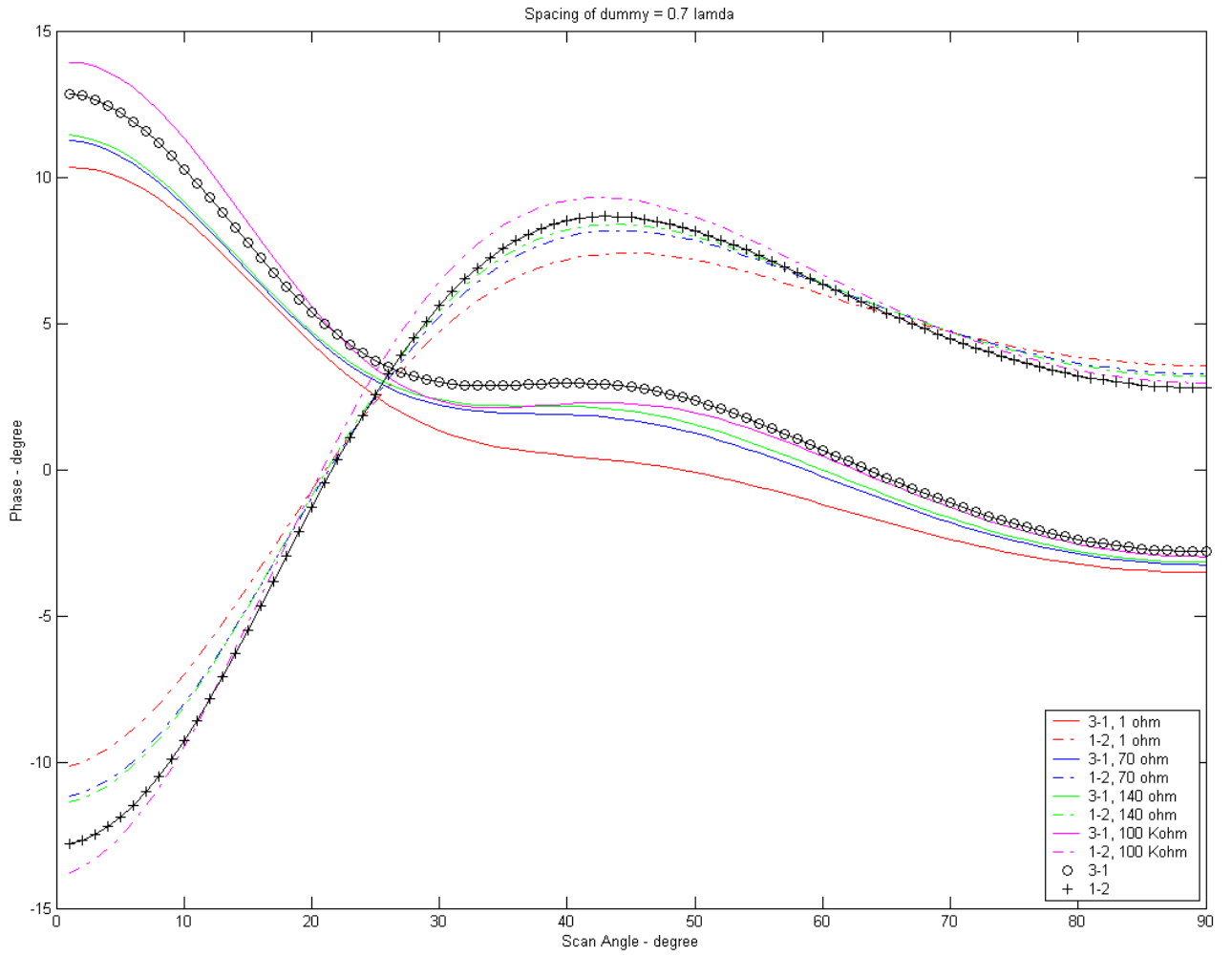
Figure 72.   Dummy separation variation: distance 0.7 λ_o

B. DUMMY ELEMENT LENGTH VARIATION
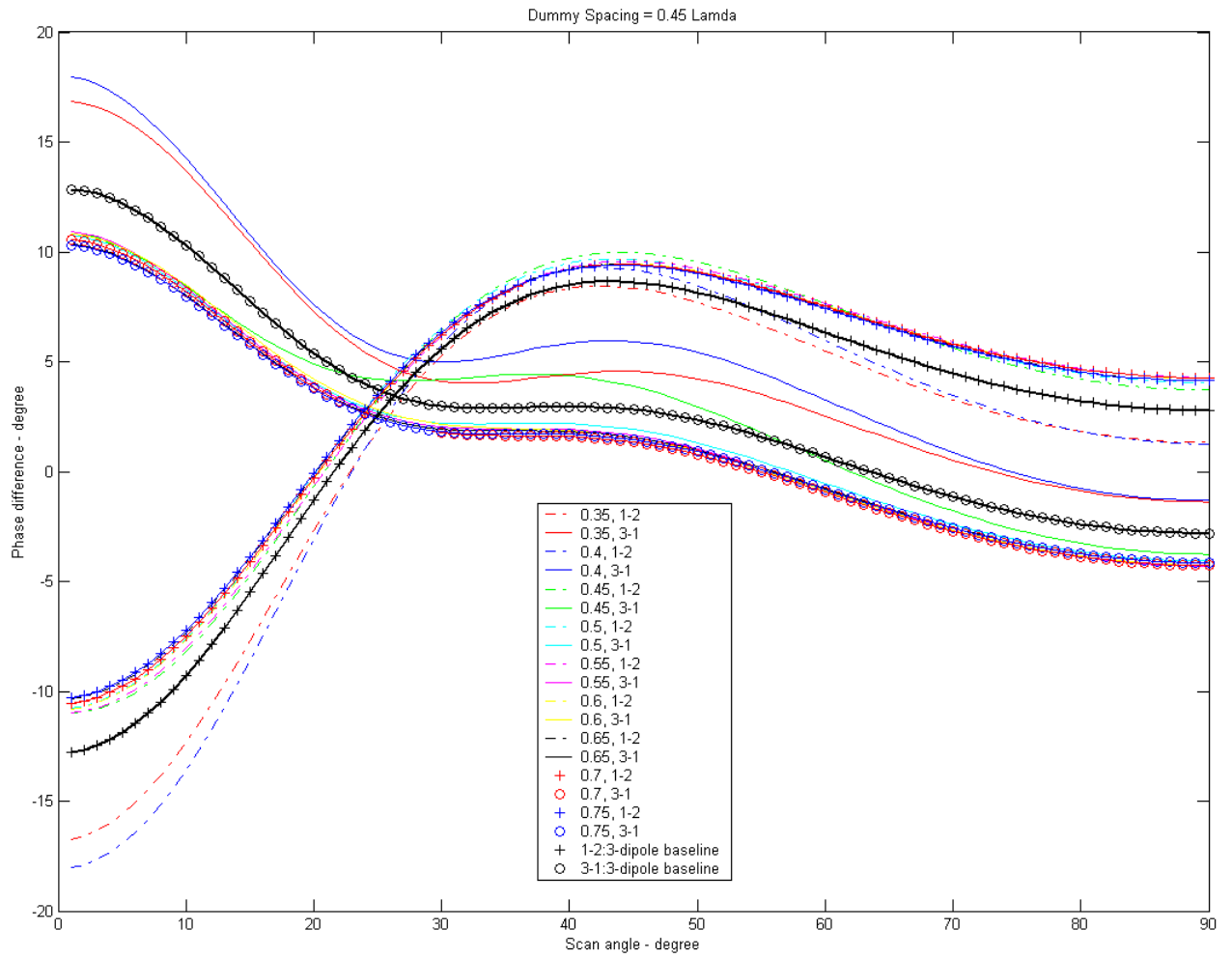
Figure 73.   Dummy element length variation: dummy distance = $0.45\,\lambda_o$
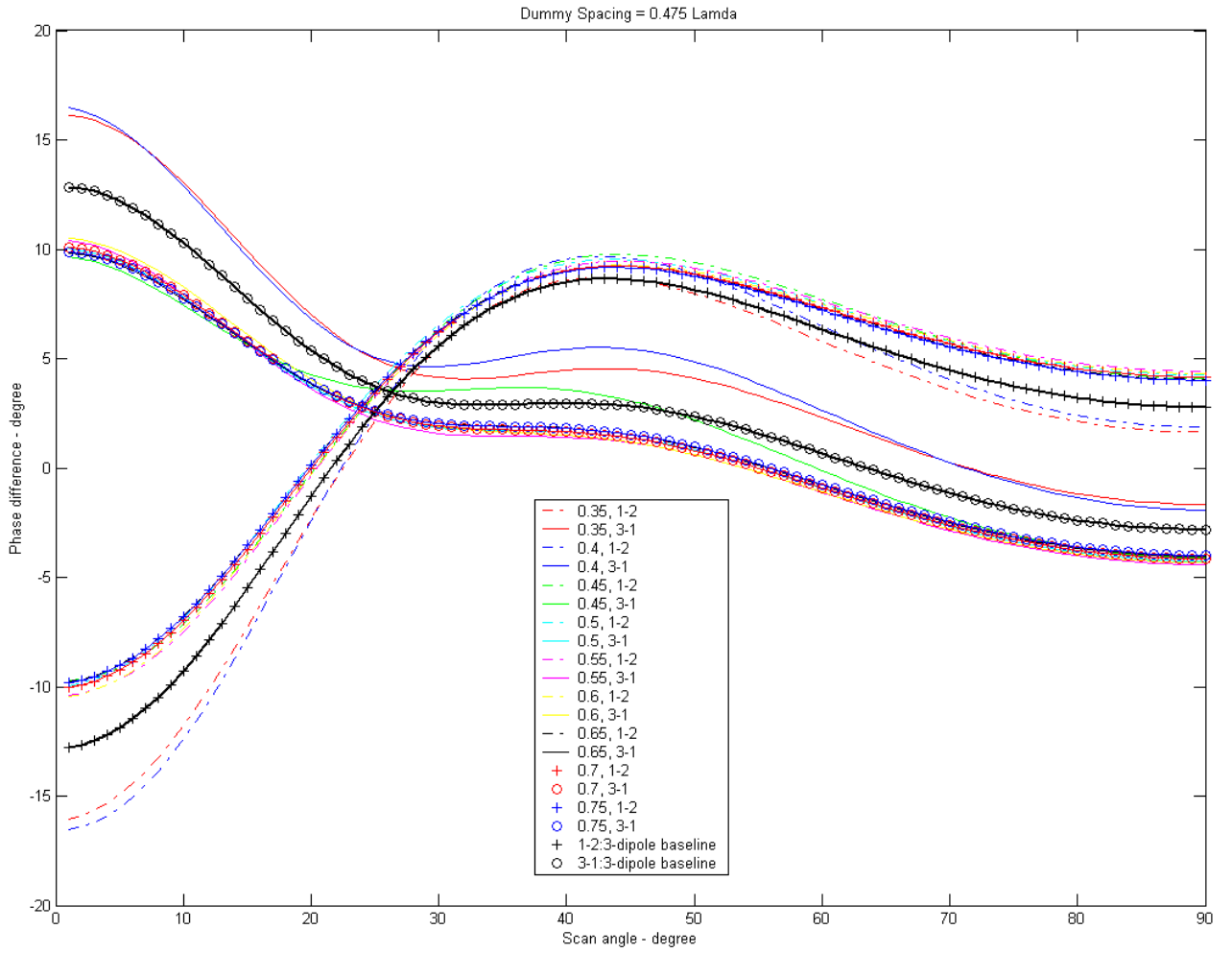
Figure 74.   Dummy element length variation: dummy distance = $0.475\,\lambda_o$
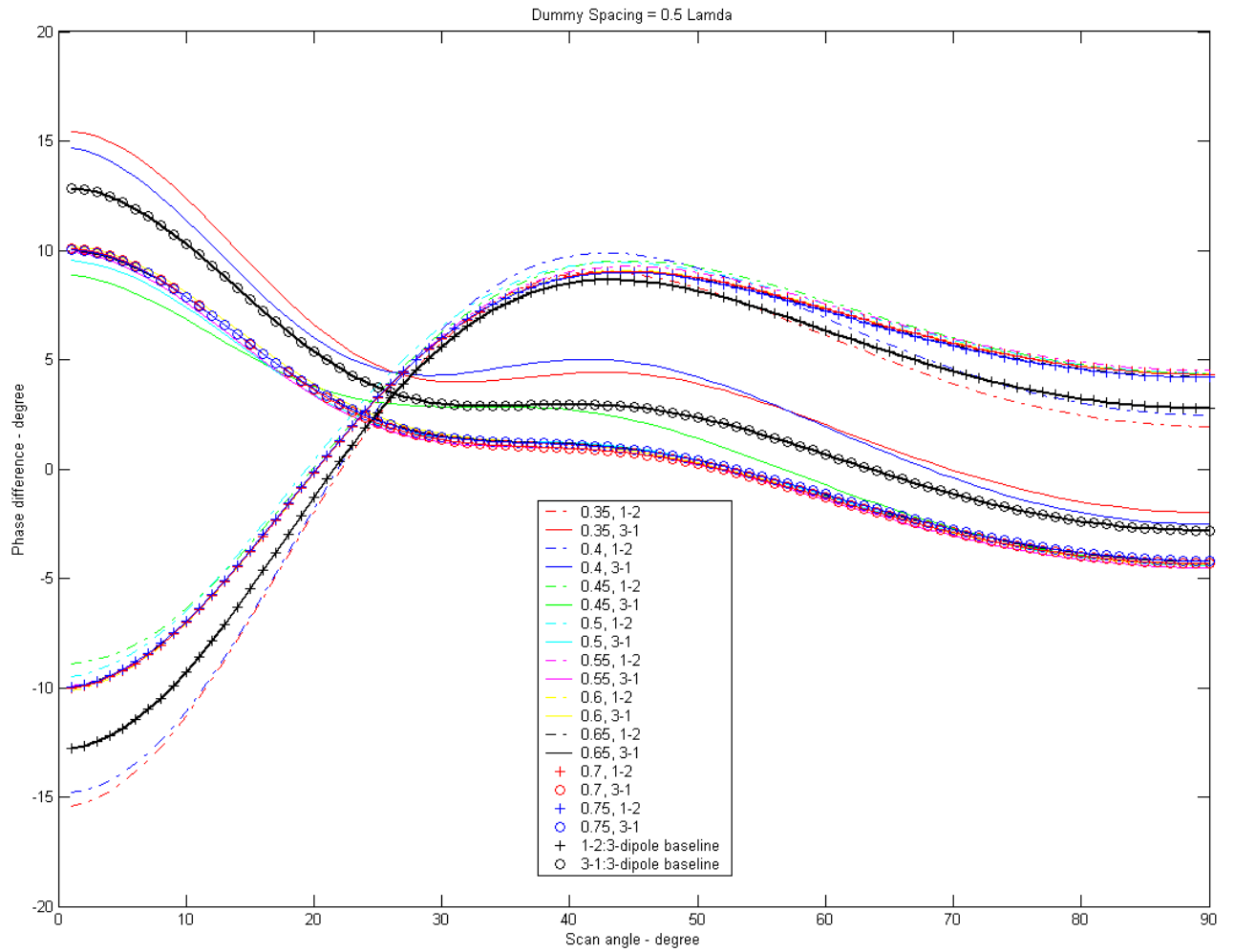
Figure 75.   Dummy element length variation: dummy distance = $0.5\,\lambda_o$
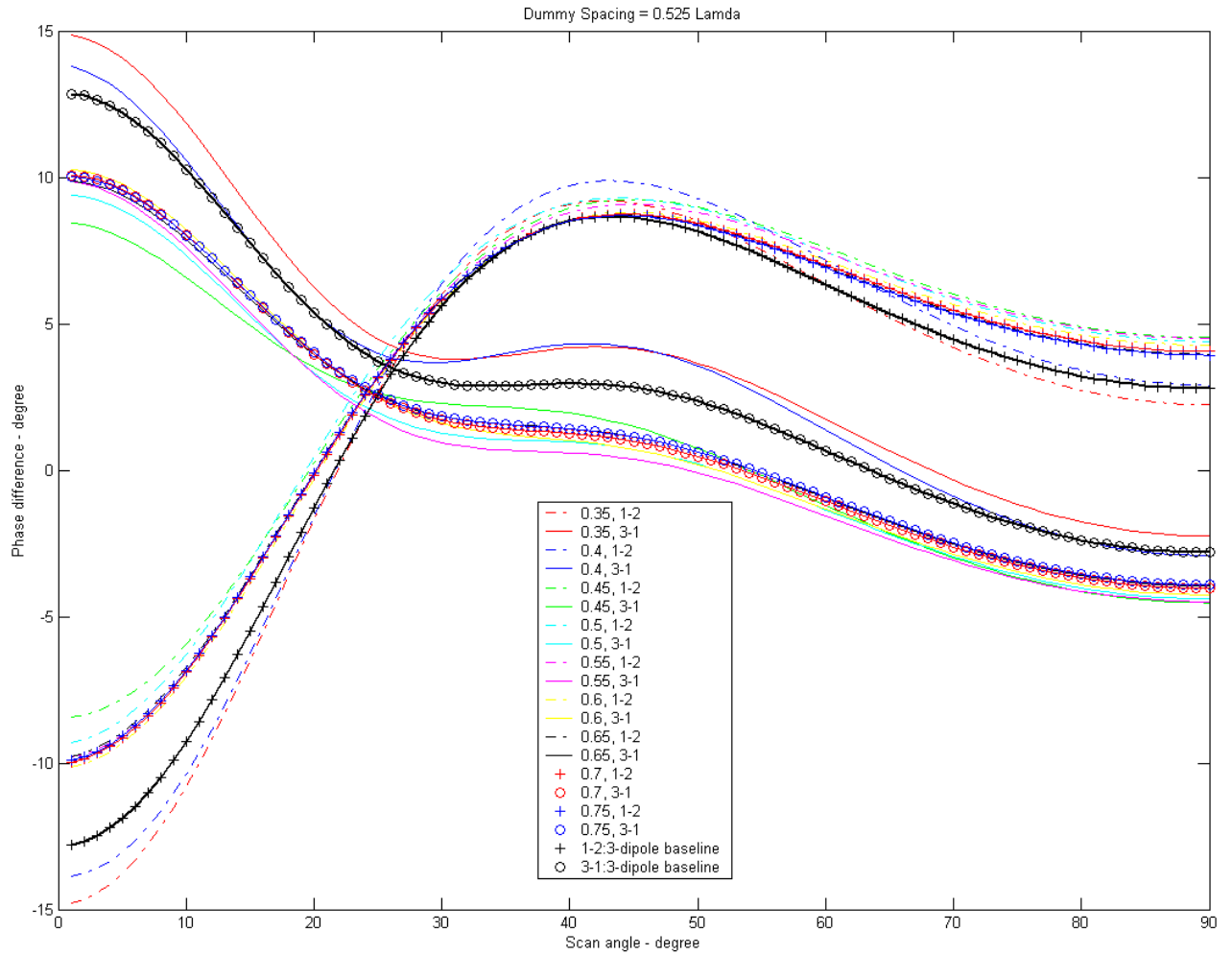
Figure 76.   Dummy element length variation: dummy distance = 0.525 λ_o

97
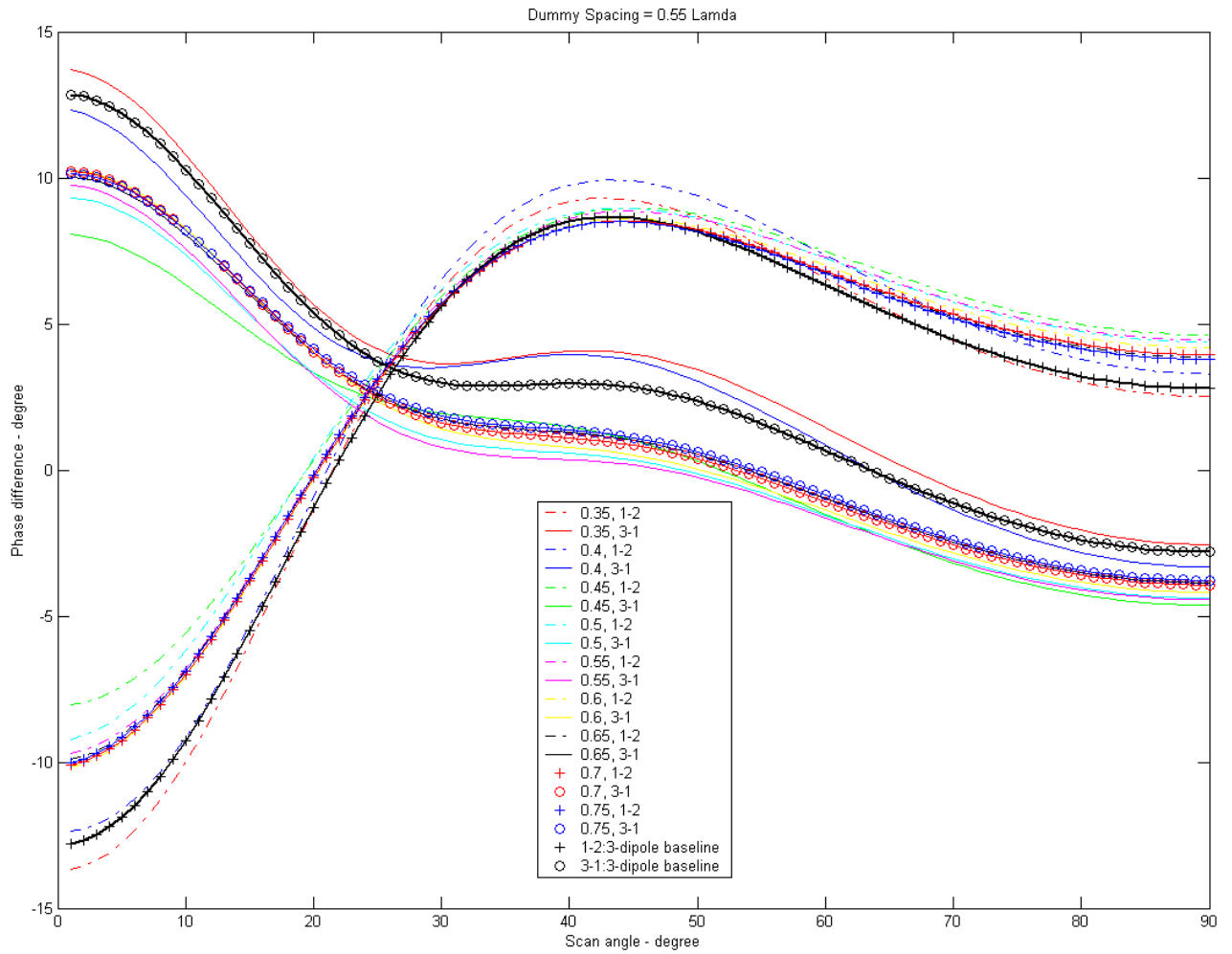
Figure 77.   Dummy element length variation: dummy distance = $0.55\,\lambda_o$
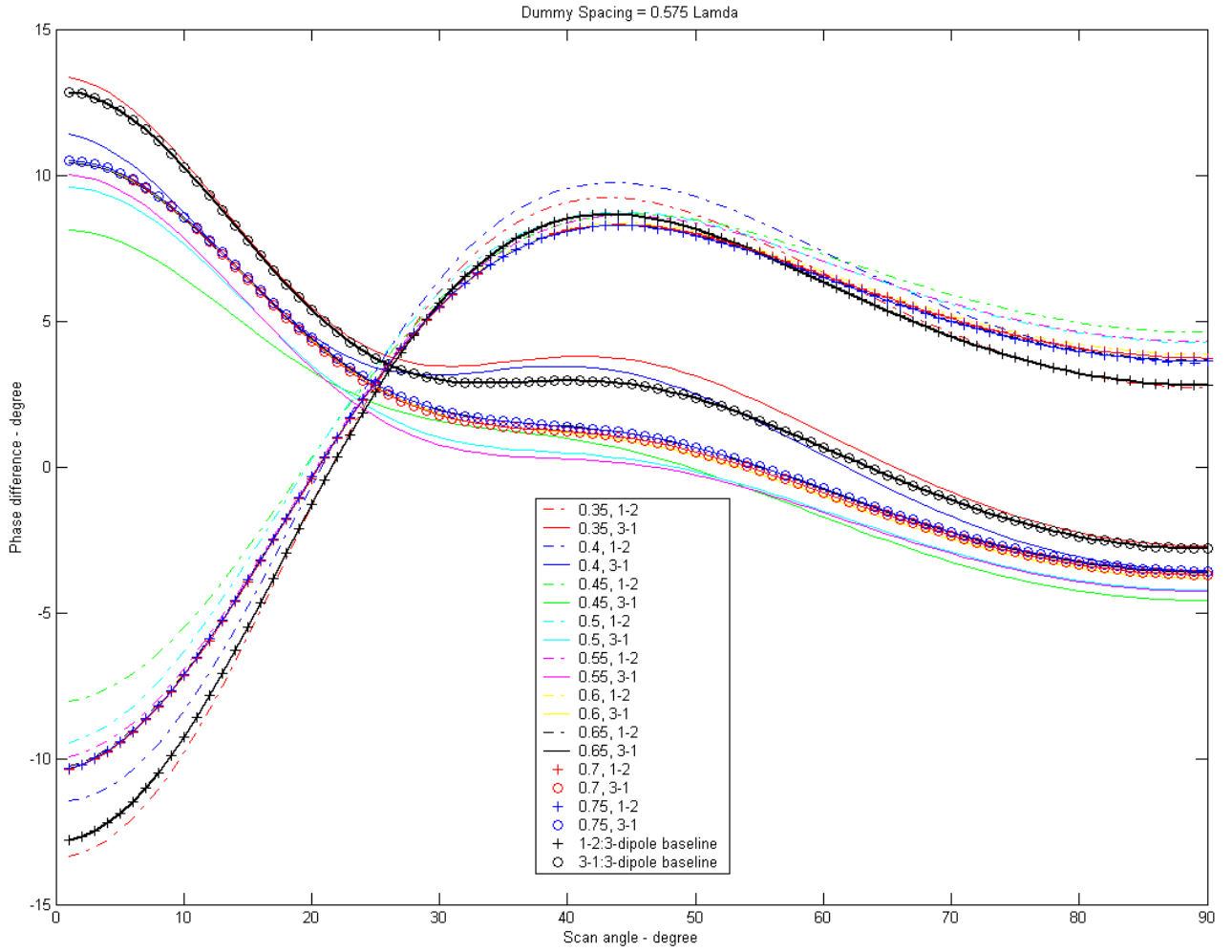
Figure 78.   Dummy element length variation: dummy distance = $0.575\,\lambda_o$
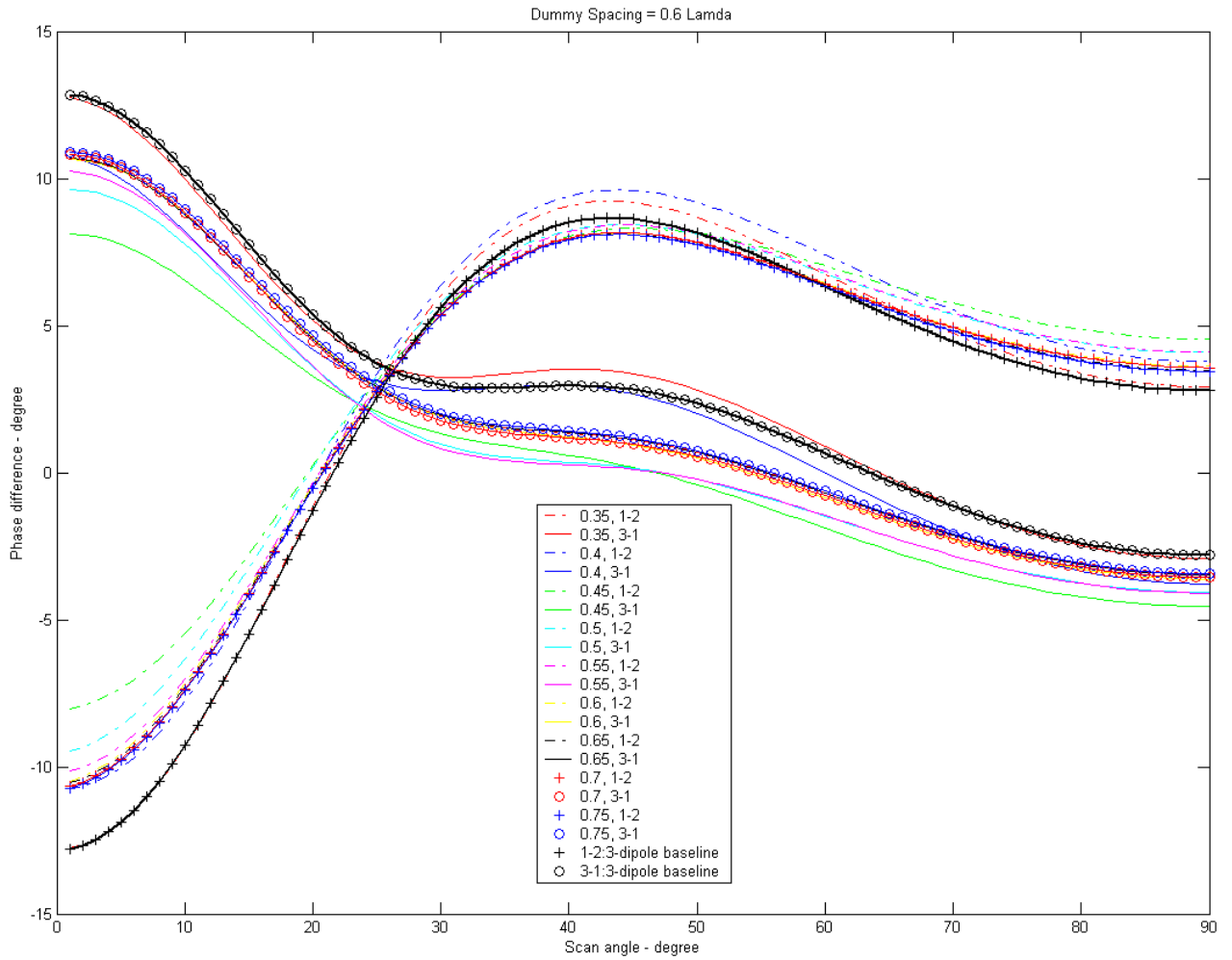
Figure 79.   Dummy element length variation: dummy distance = $0.6\,\lambda_o$
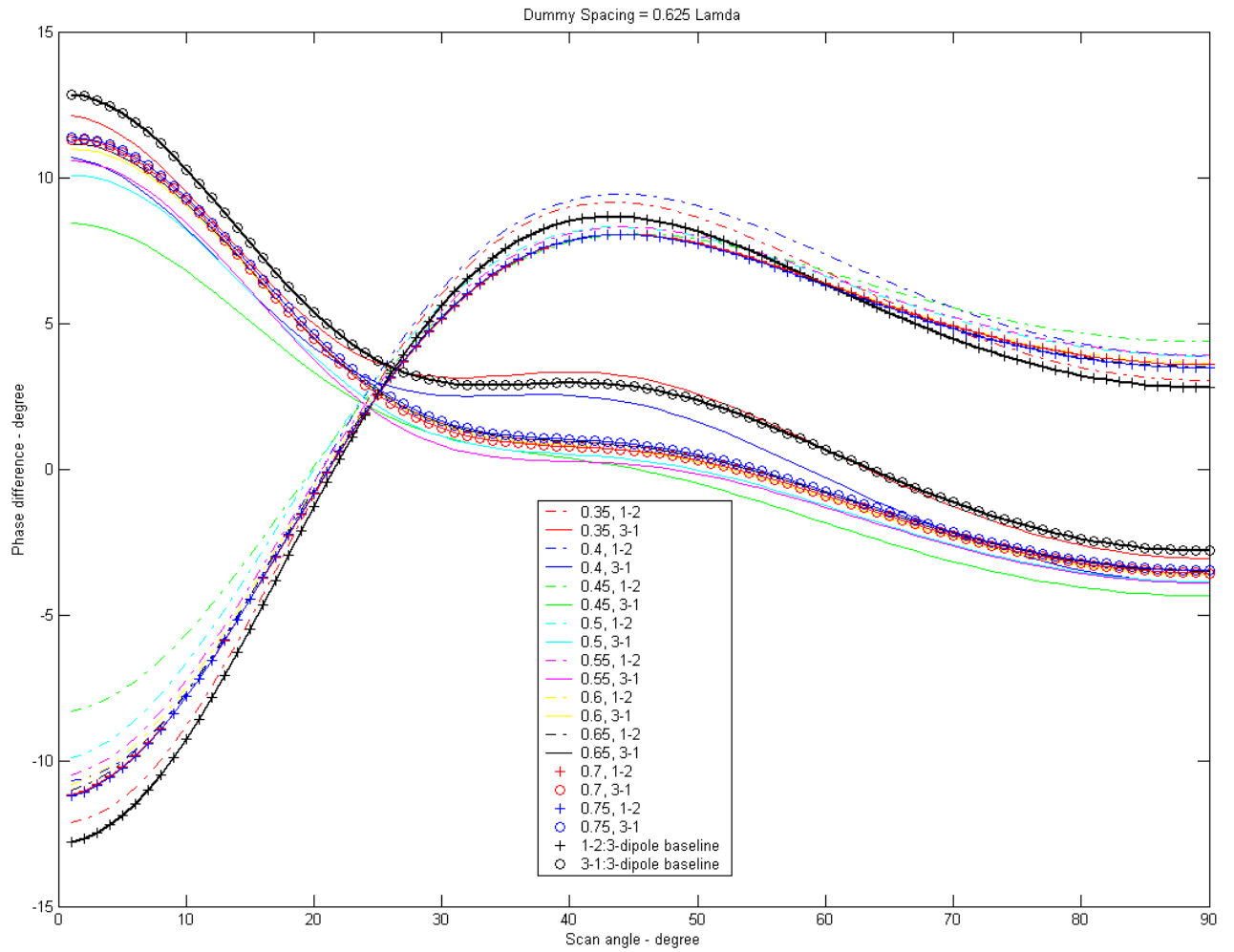
Figure 80.   Dummy element length variation: dummy distance = $0.625\,\lambda_o$
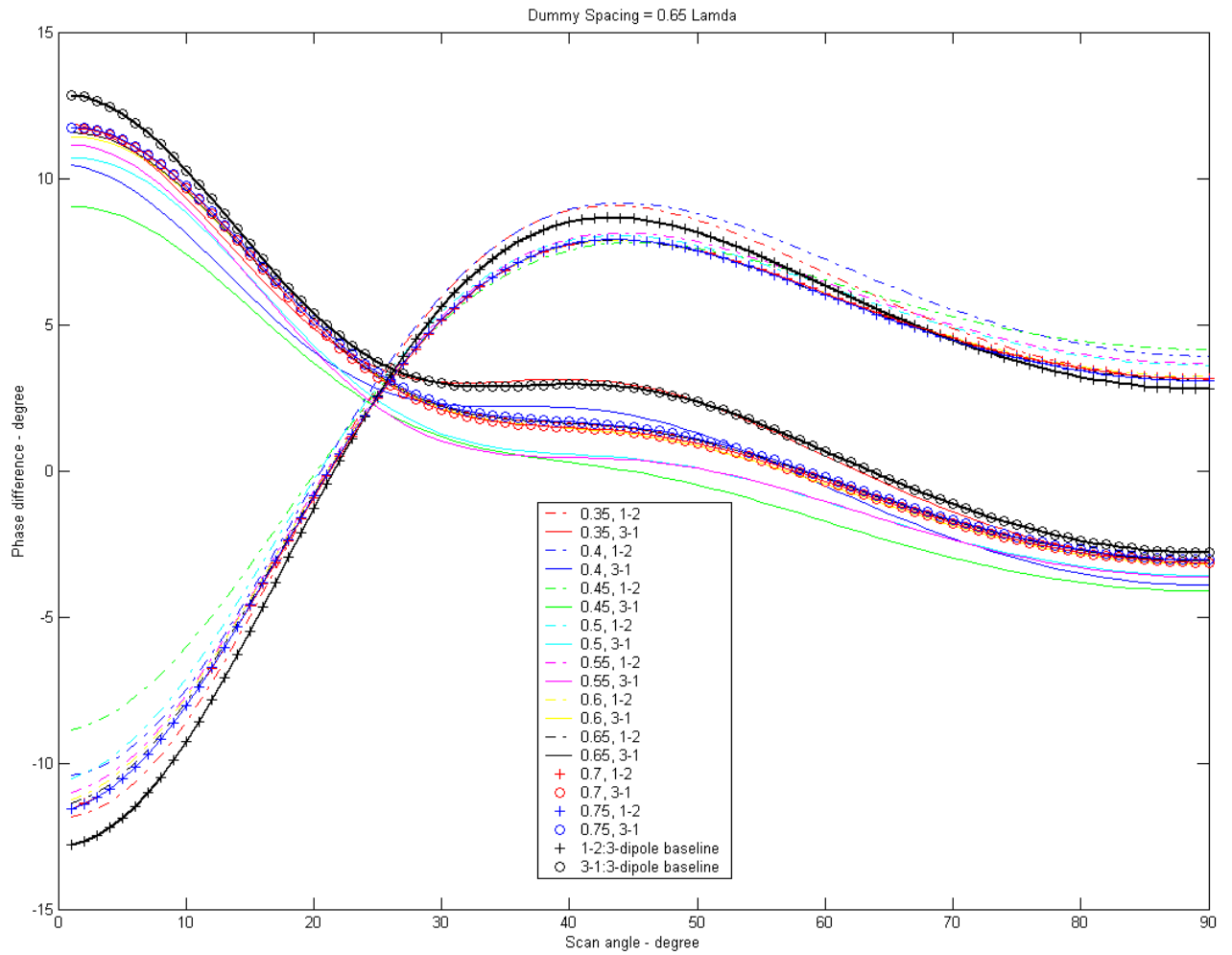
Figure 81.   Dummy element length variation: dummy distance = $0.65\,\lambda_o$

C. COMPLEX LOAD VARIATION
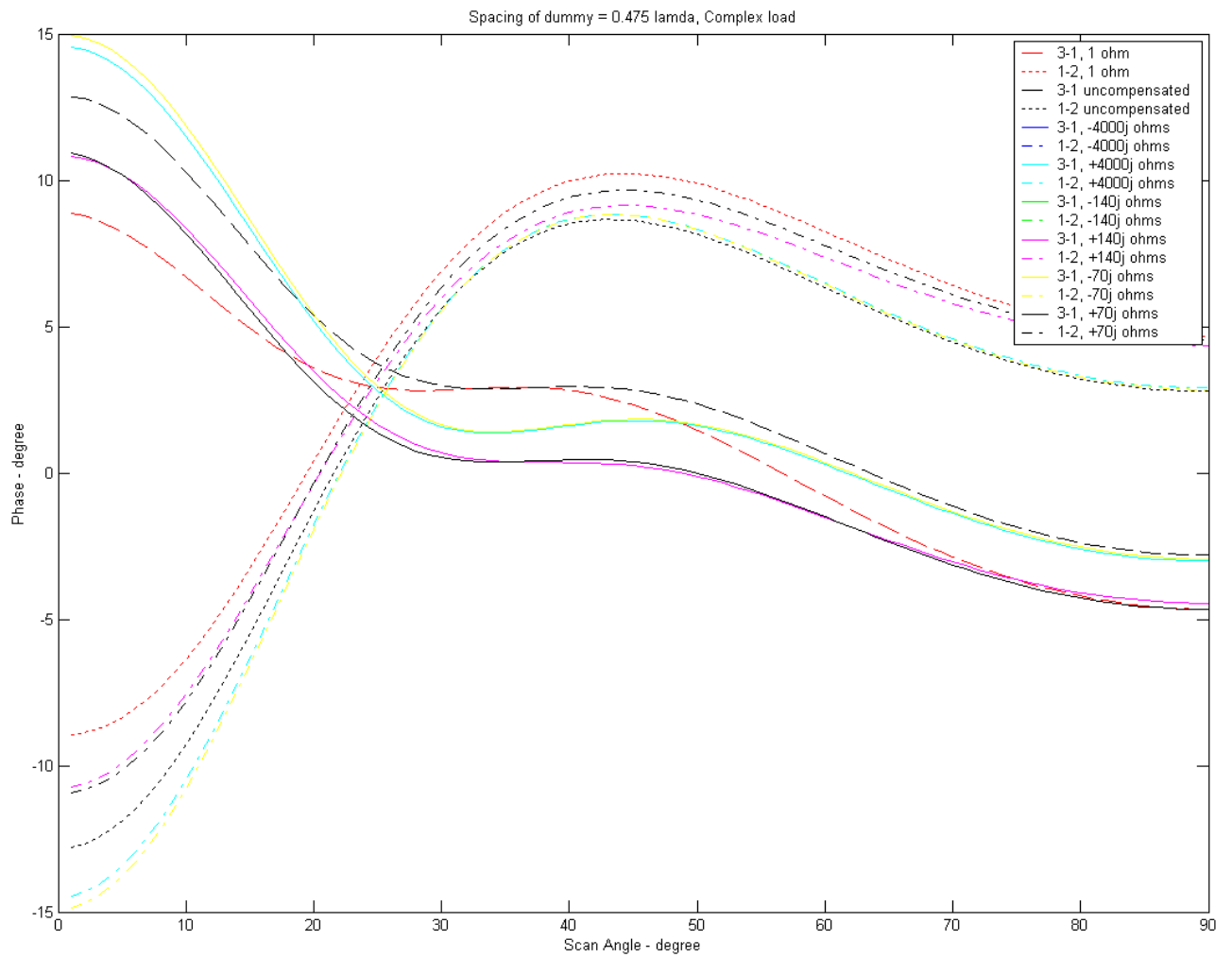
Figure 82.   Complex load: dummy distance = 0.475 λ_o
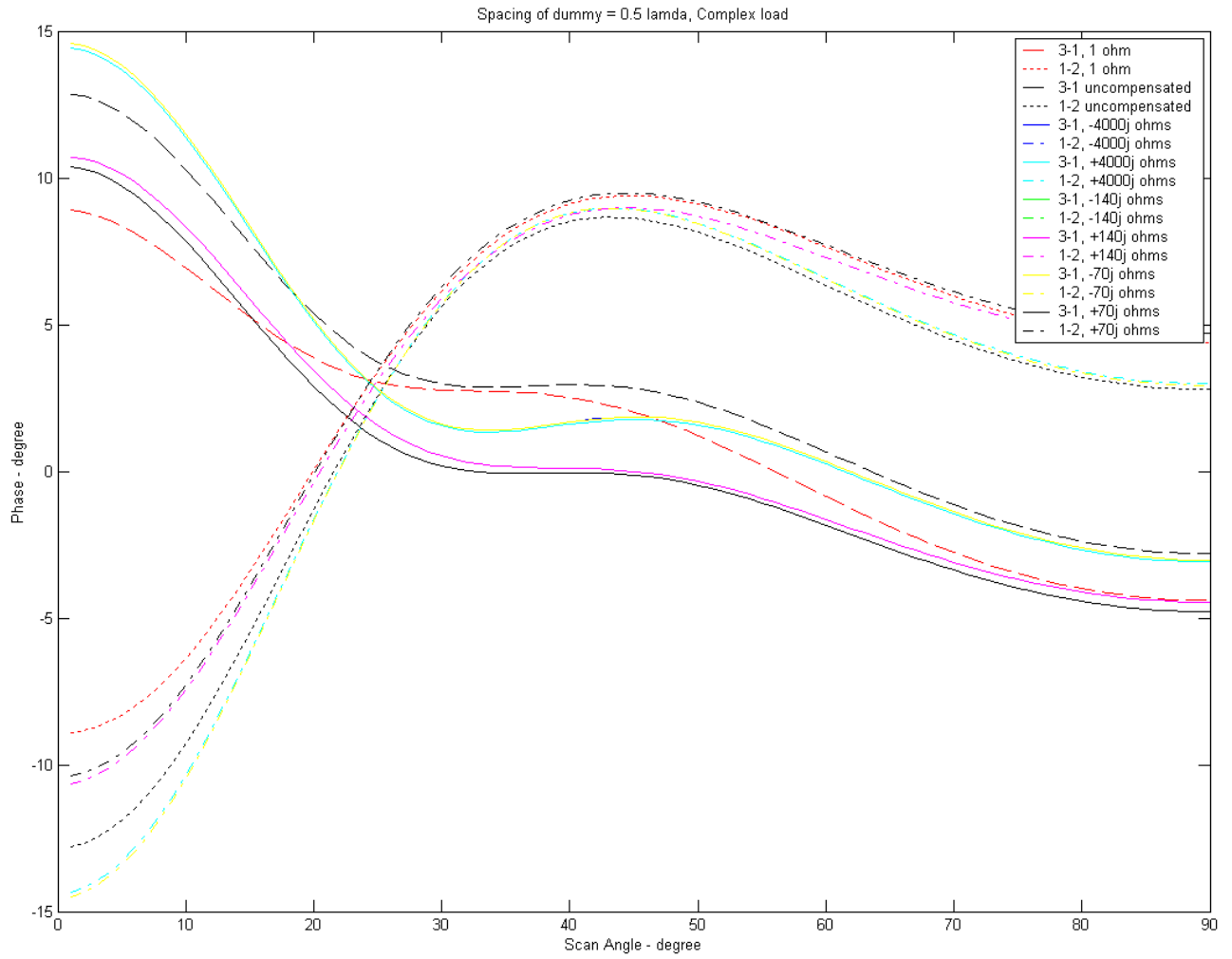
Figure 83.   Complex load: dummy distance = $0.5\,\lambda_o$
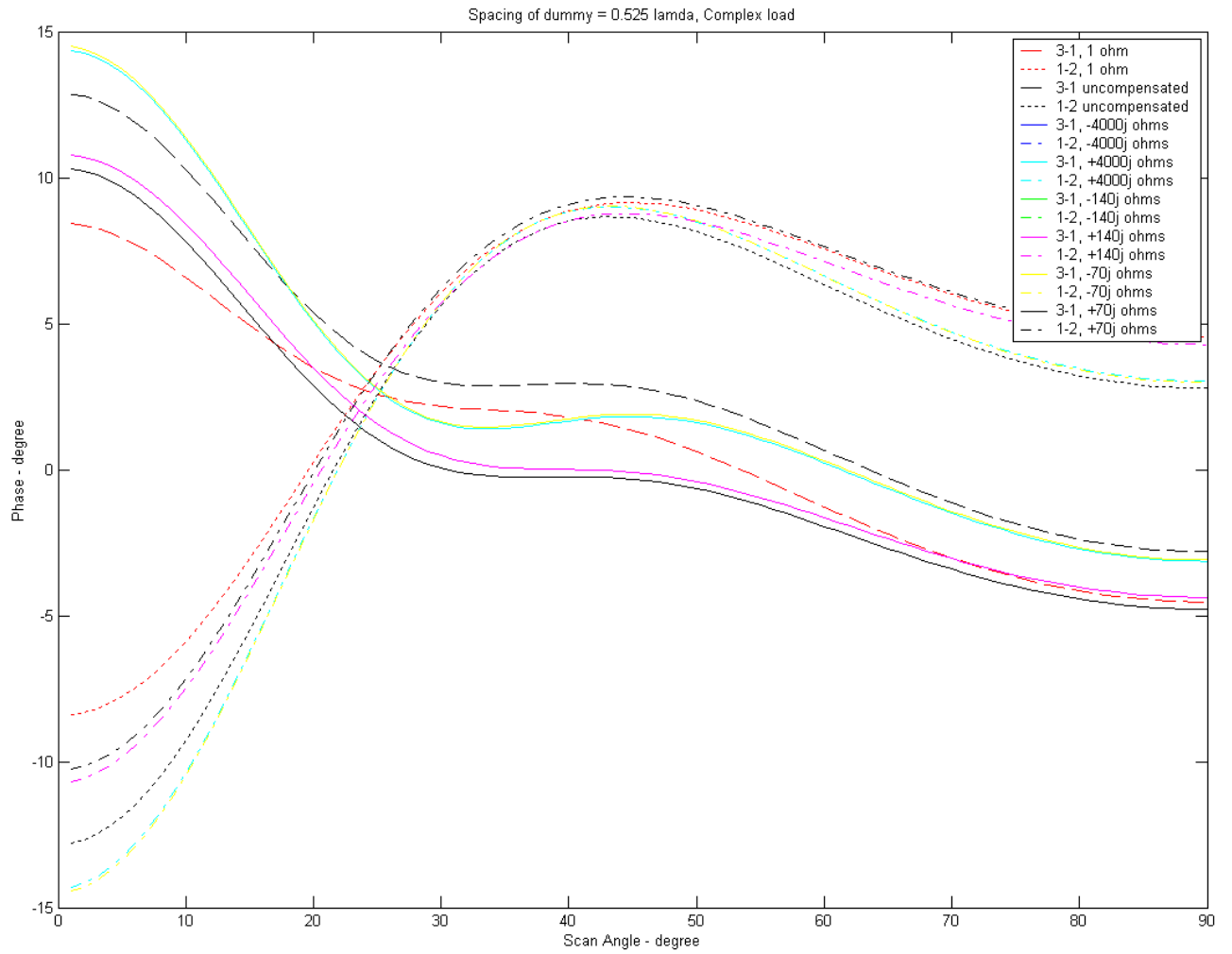
Figure 84.   Complex load: dummy distance = $0.525\,\lambda_o$

105
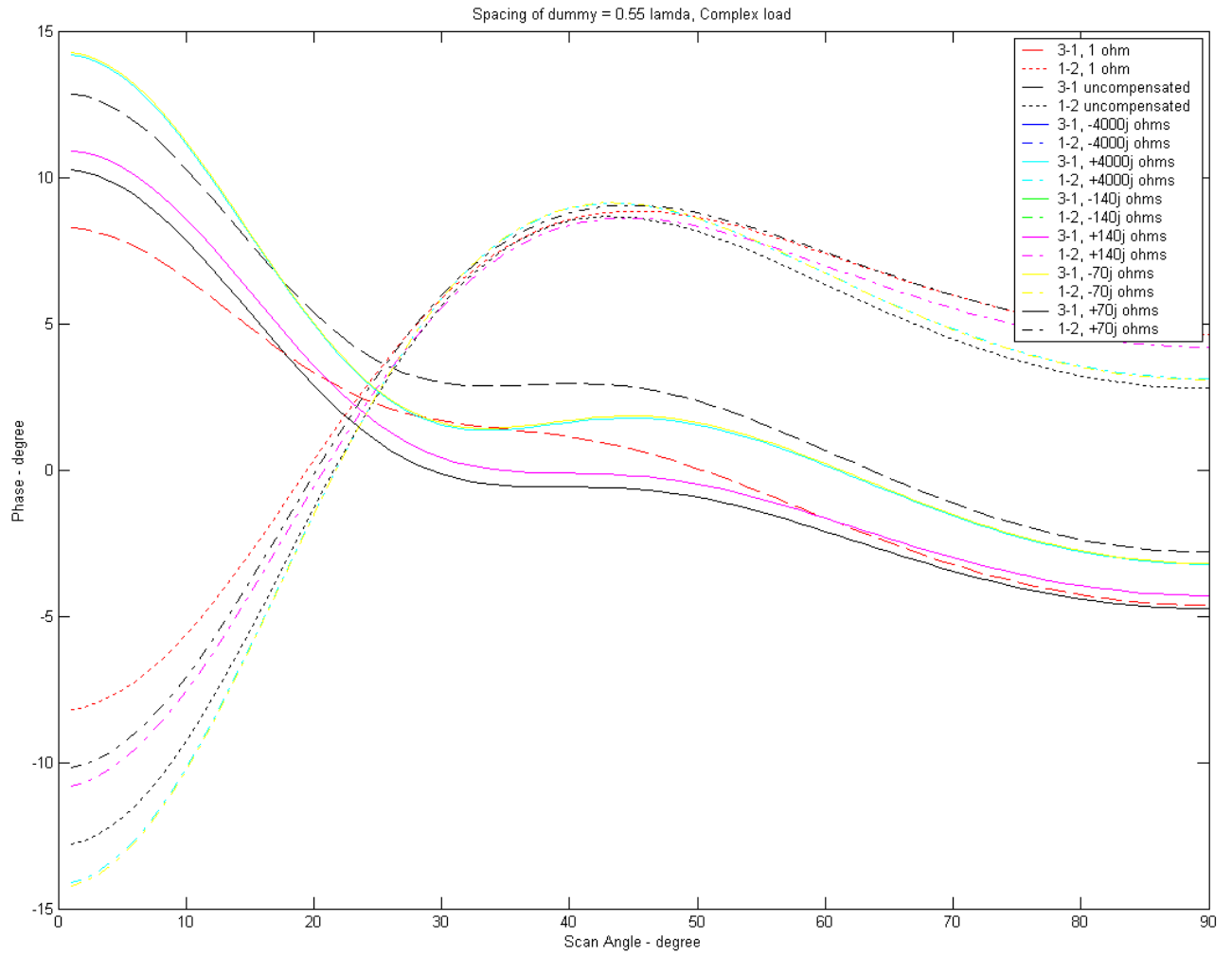
Figure 85.   Complex load: dummy distance = 0.55 λ_o

106
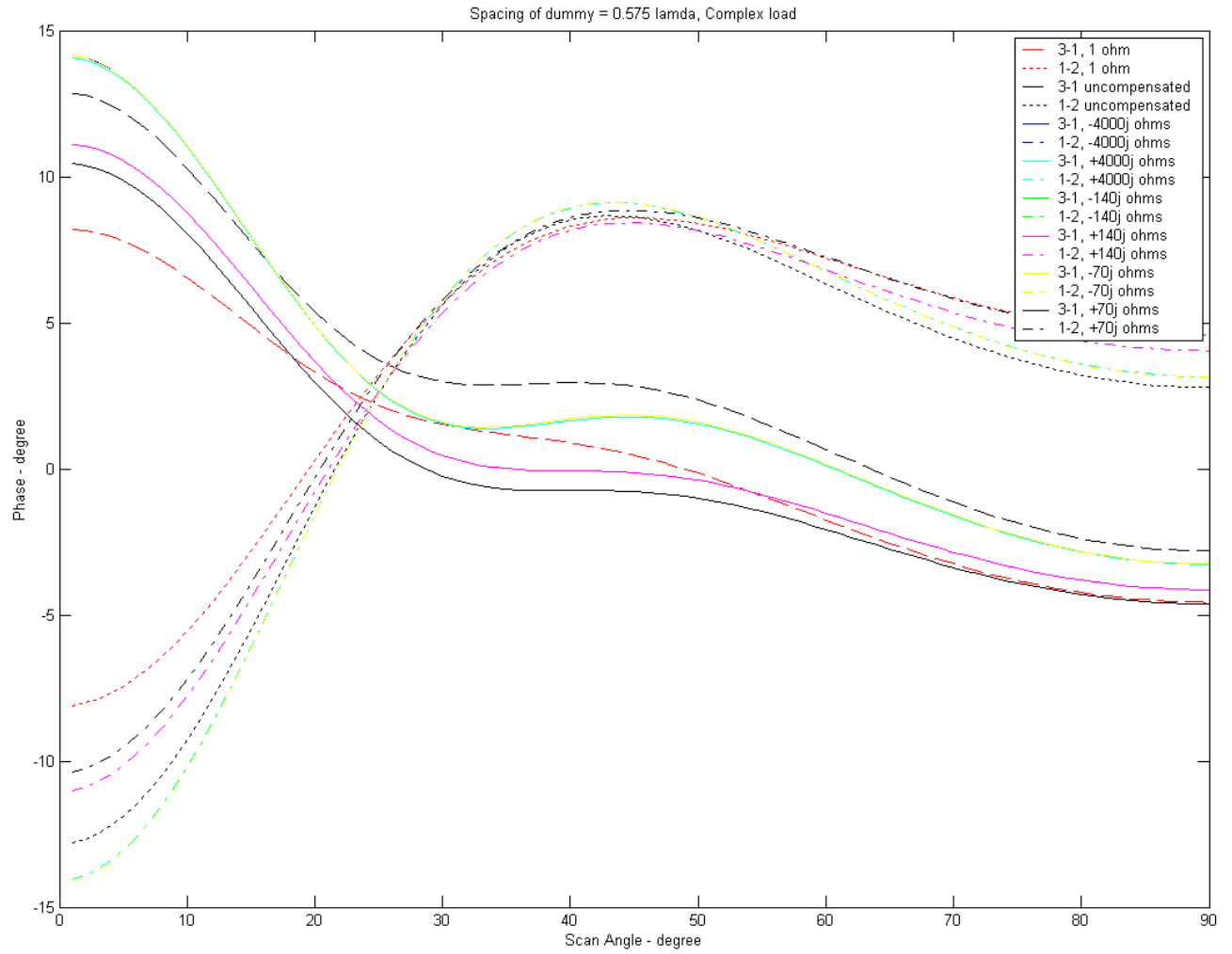
Figure 86.   Complex load: dummy distance = 0.575 λ_o

107
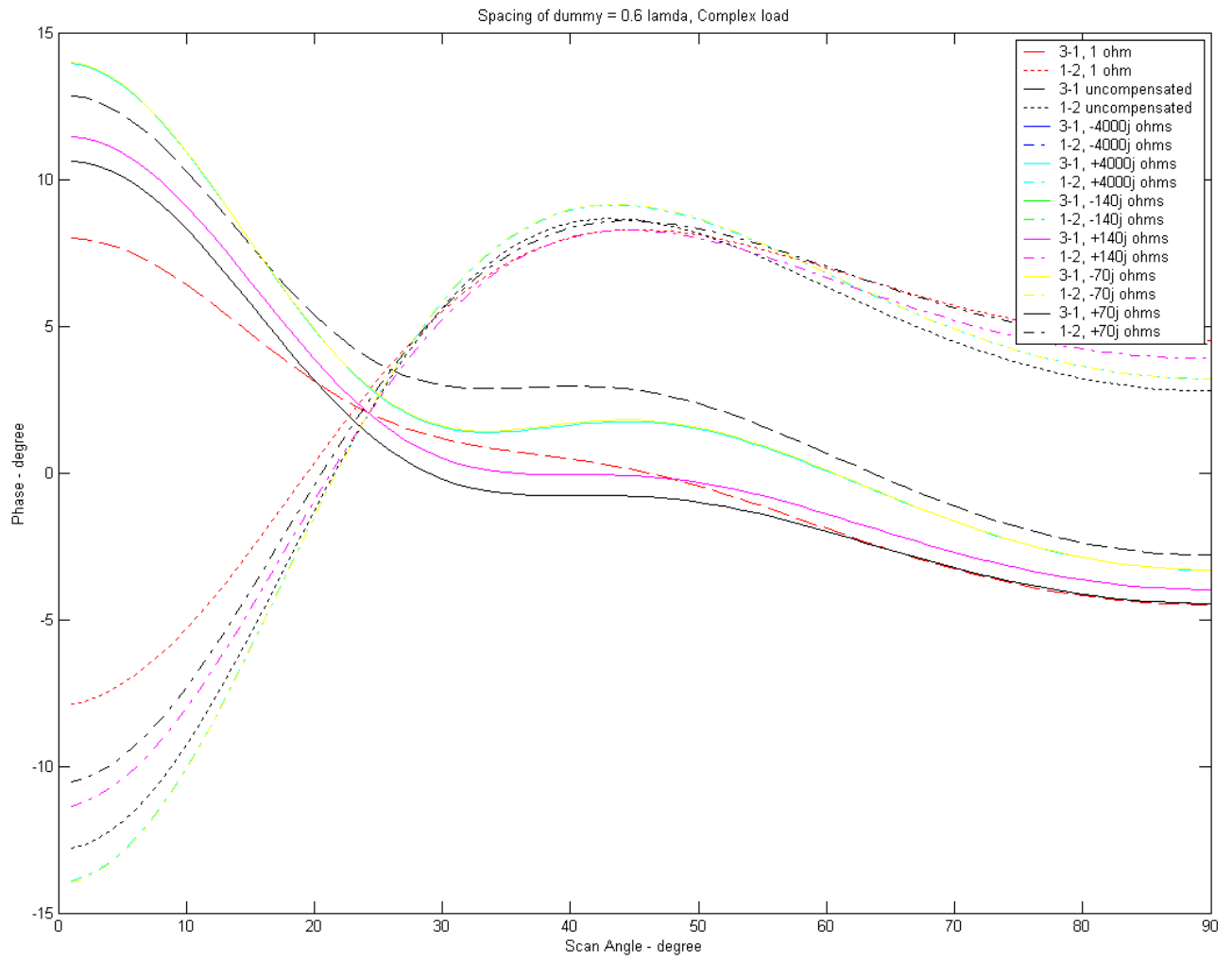
Figure 87.   Complex load: dummy distance = $0.6\,\lambda_o$
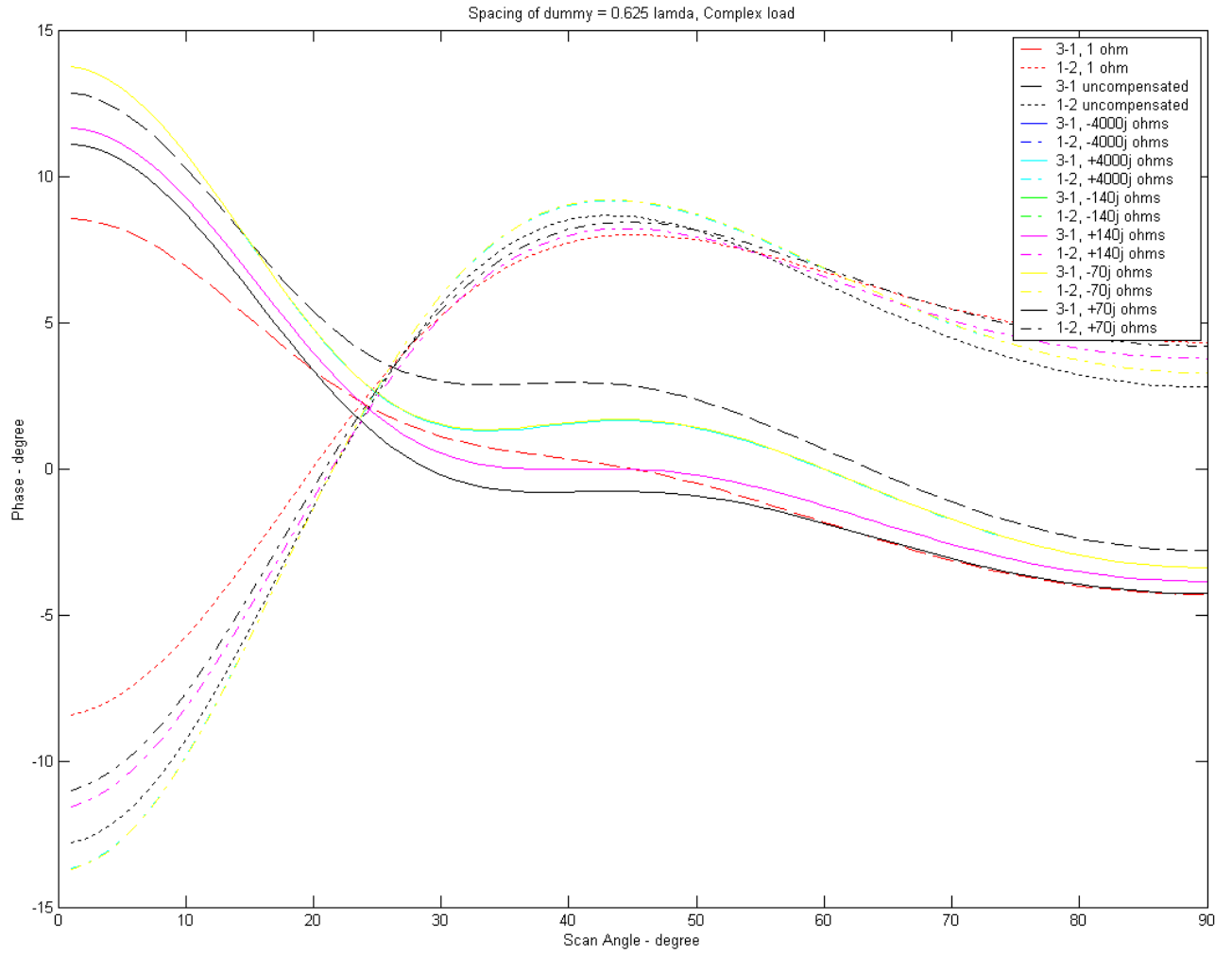
Figure 88.　　Complex load: dummy distance = $0.625 \lambda_o$

D. SCATTERING MATRIX FOR VARIOUS DIPOLE ARM LENGTHS
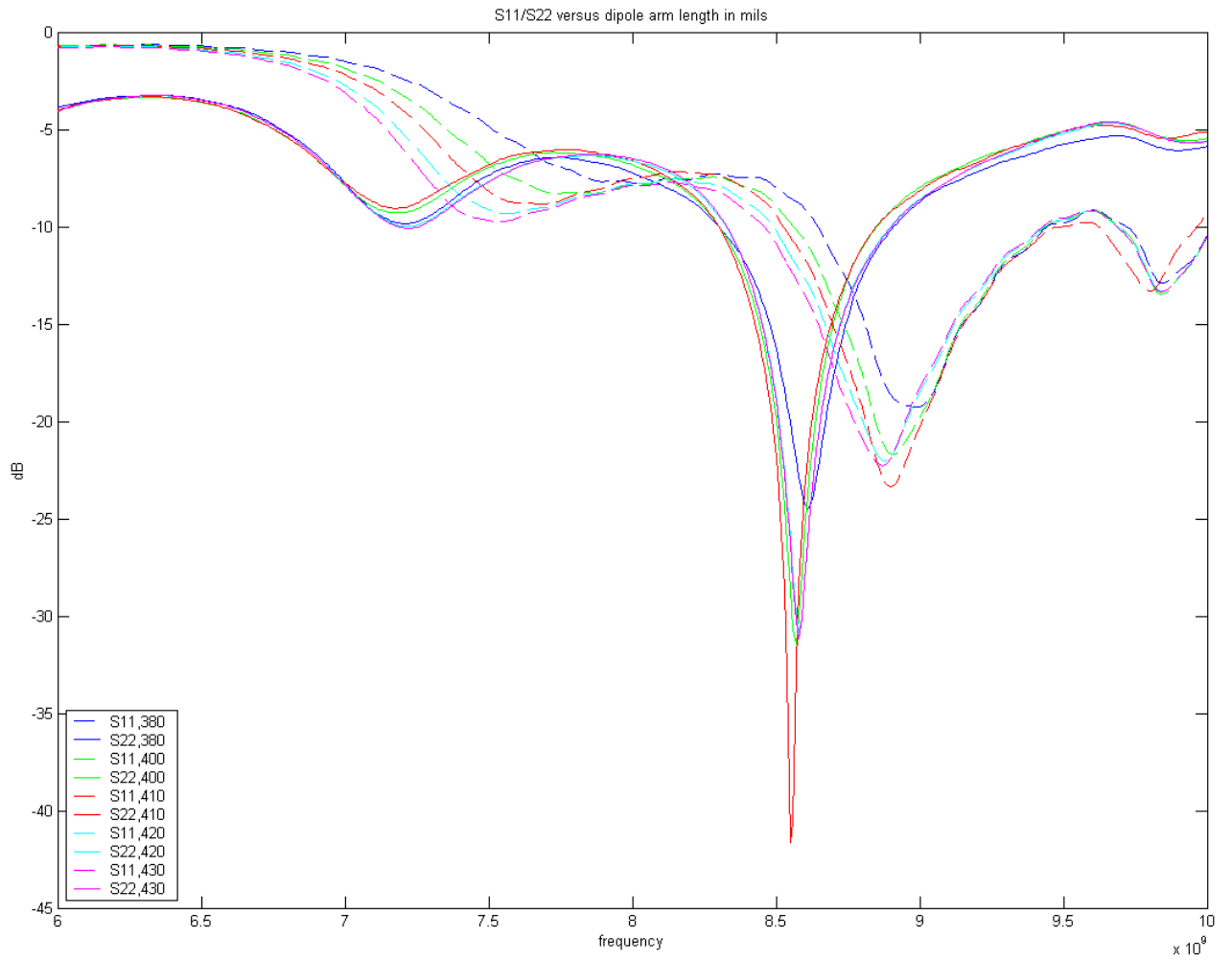
Figure 89.   Scattering parameter – Dipole arm from 380 to 430 mils
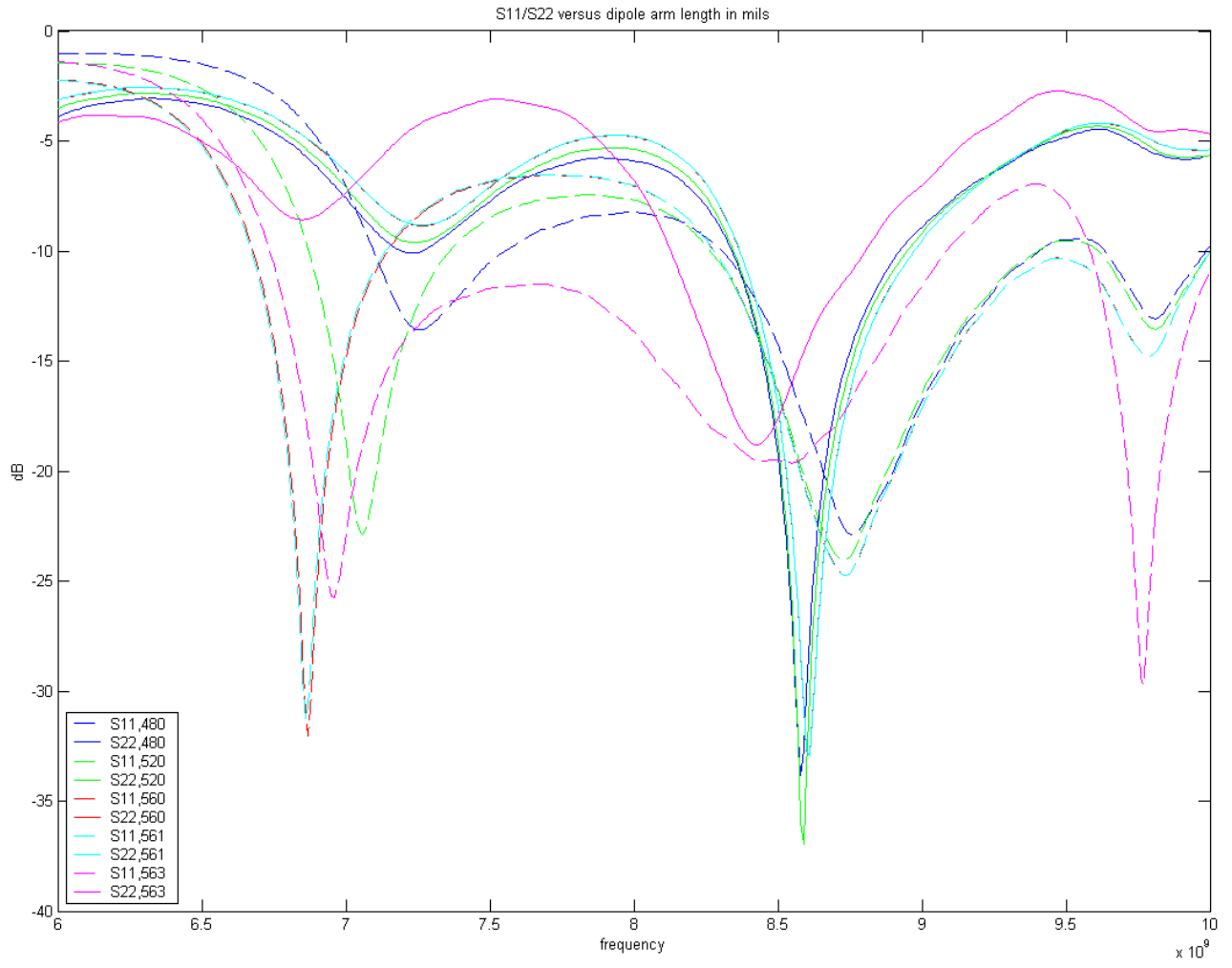
Figure 90.   Scattering parameter – Dipole arm from 480 to 563 mils

111
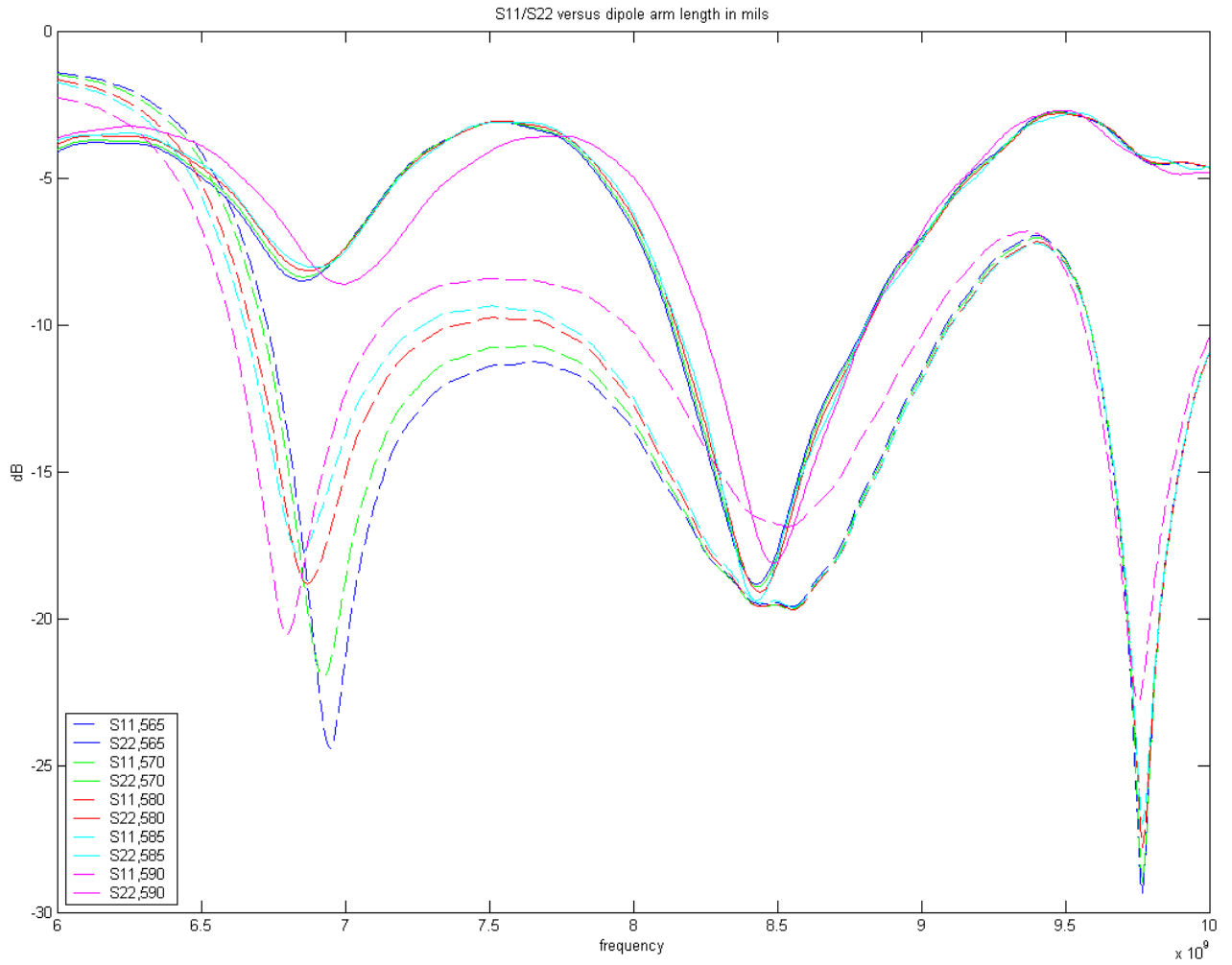
Figure 91. Scattering parameter – Dipole arm from 565 to 590 mils
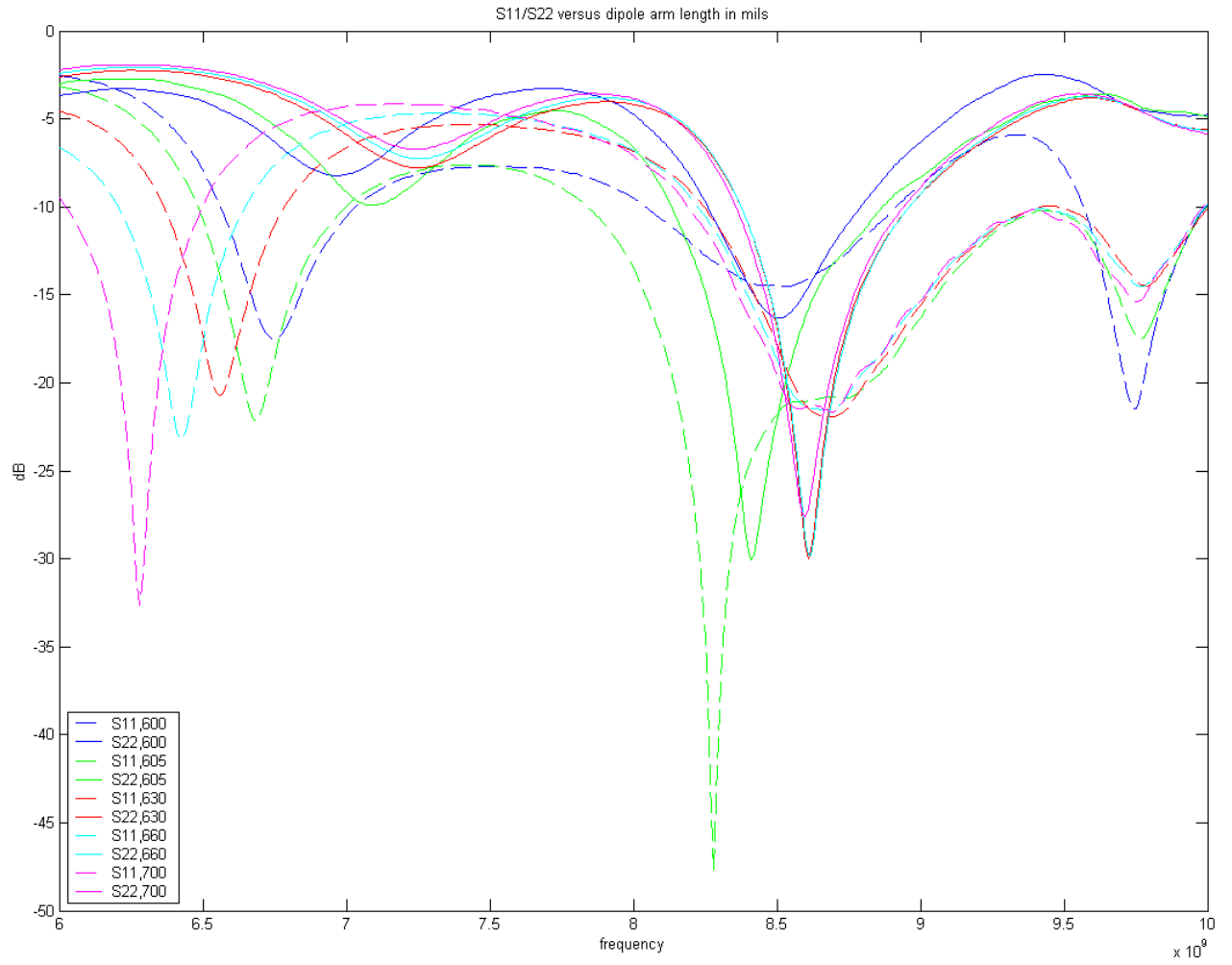
Figure 92.   Scattering parameter – Dipole arm from 600 to 700 mils

E. SMITH CHART FOR DIPOLE ELEMENT PROPERLY MATCHED
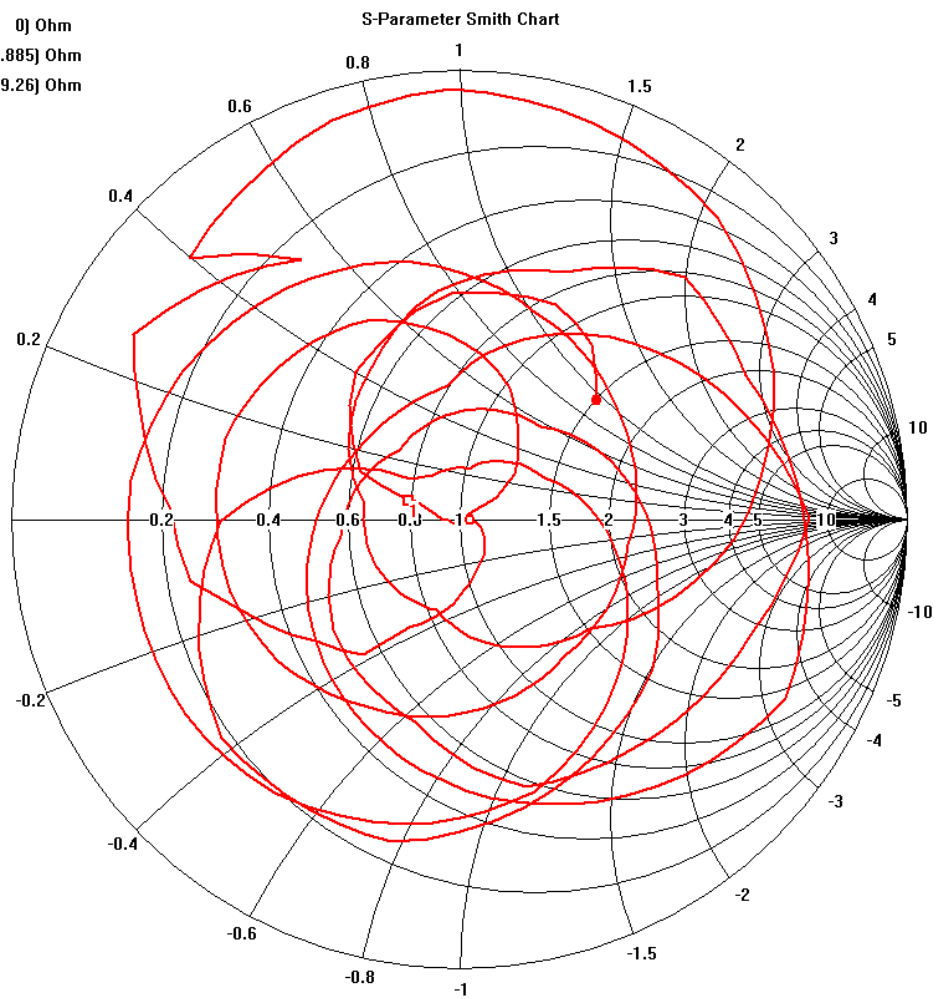
Figure 93. Single dipole element (printed circuit board) – S_{11}

S2,2 (45.01 Ohm)

○ 0.0000 (37.32, -8.613e-016) Ohm
□₁ 8.700 (52.41, -8.432) Ohm
● 10.00 (26.56, -0.5277) Ohm
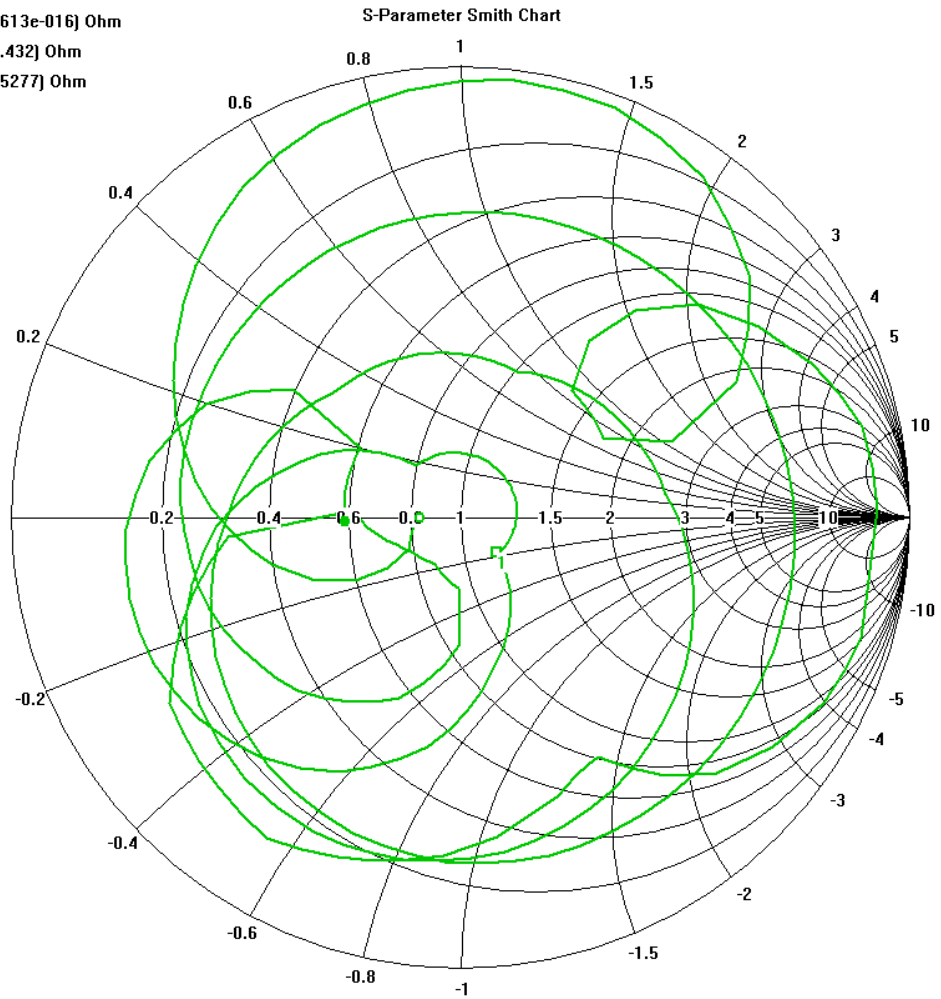
Figure 94. Single dipole element (printed circuit board) – S_{22}

F. ARRAY SCATTERING PARAMETERS
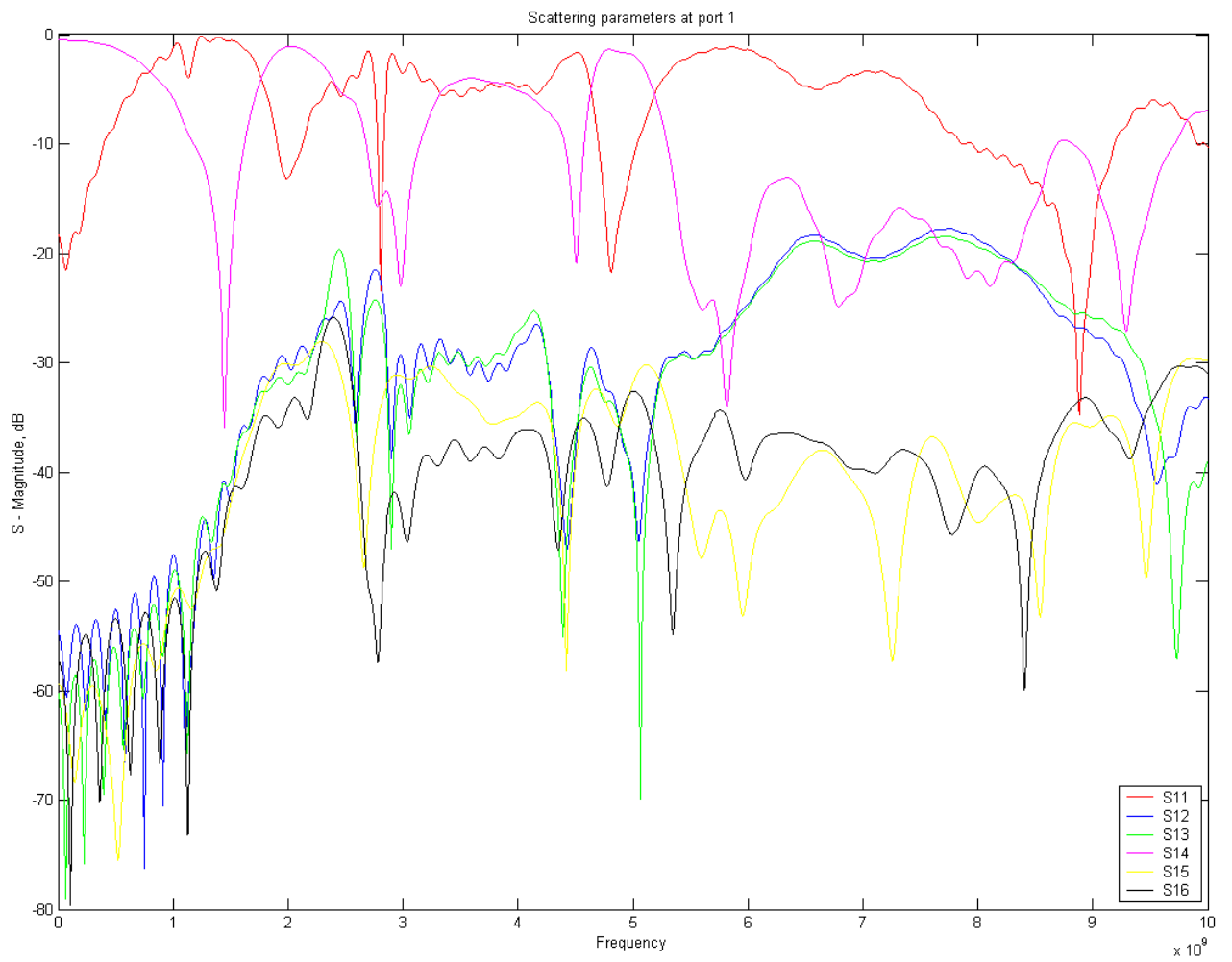
Figure 95.   Array scattering parameter at port 1
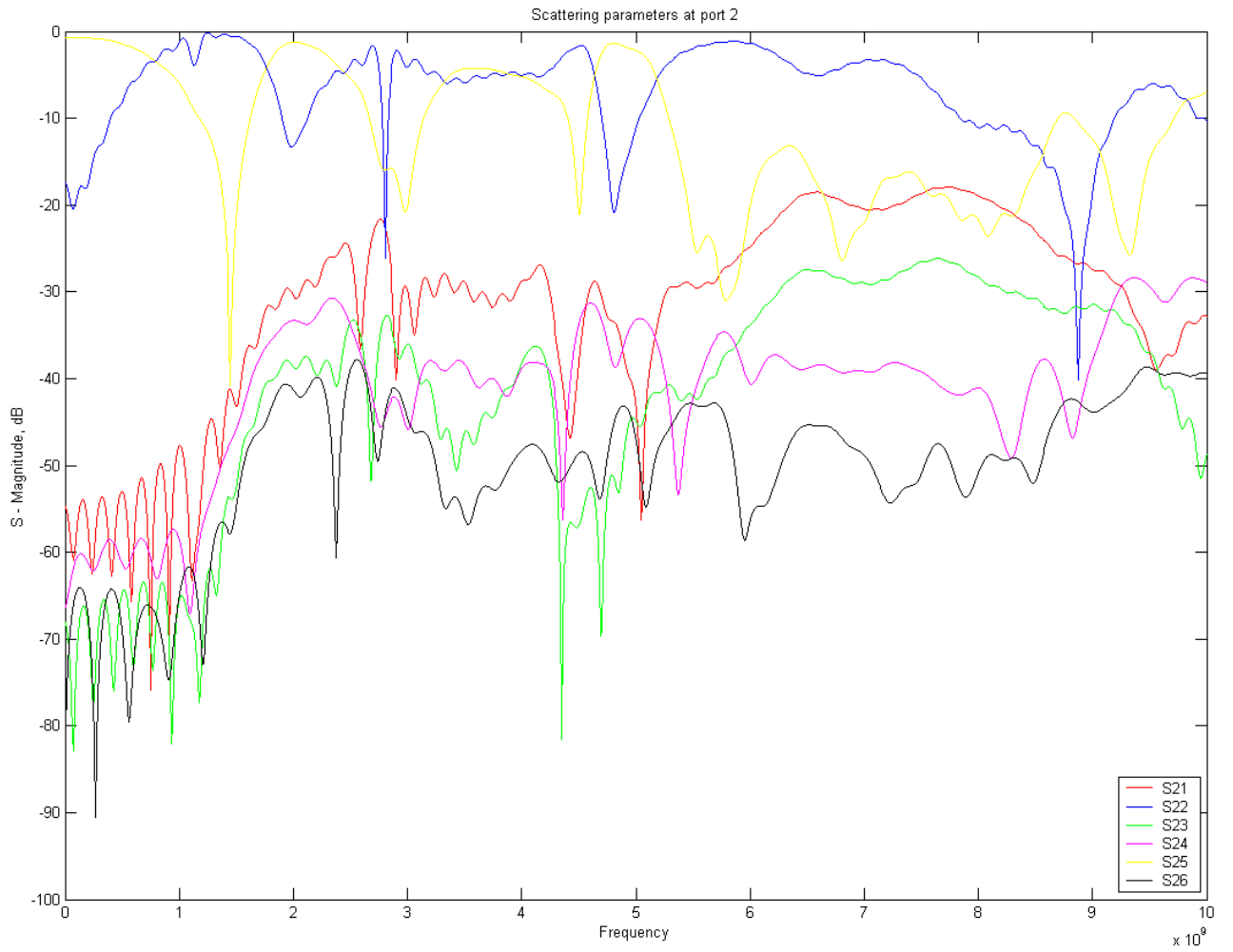
Figure 96.   Array scattering parameter at port 2
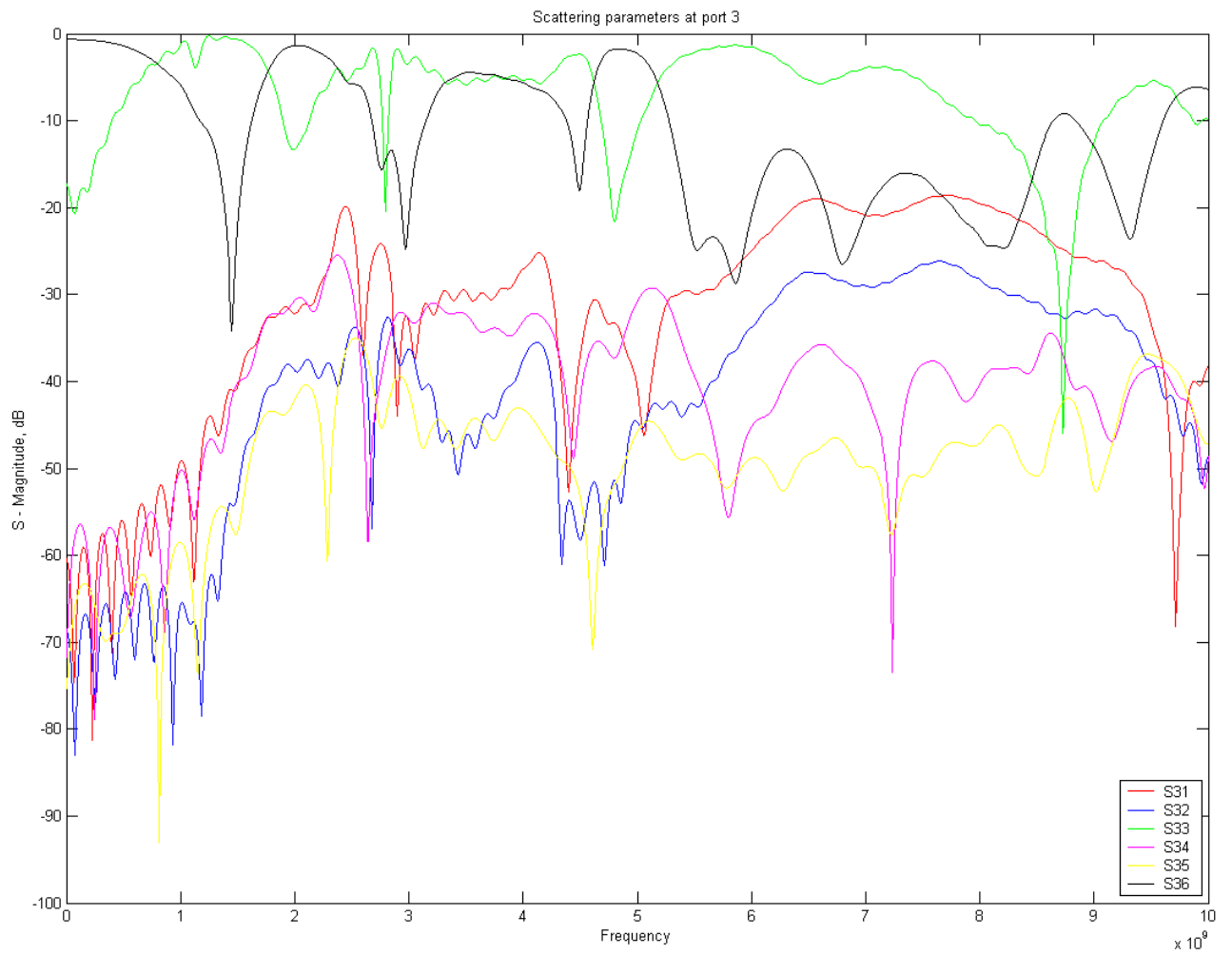
Figure 97.   Array scattering parameter at port 3
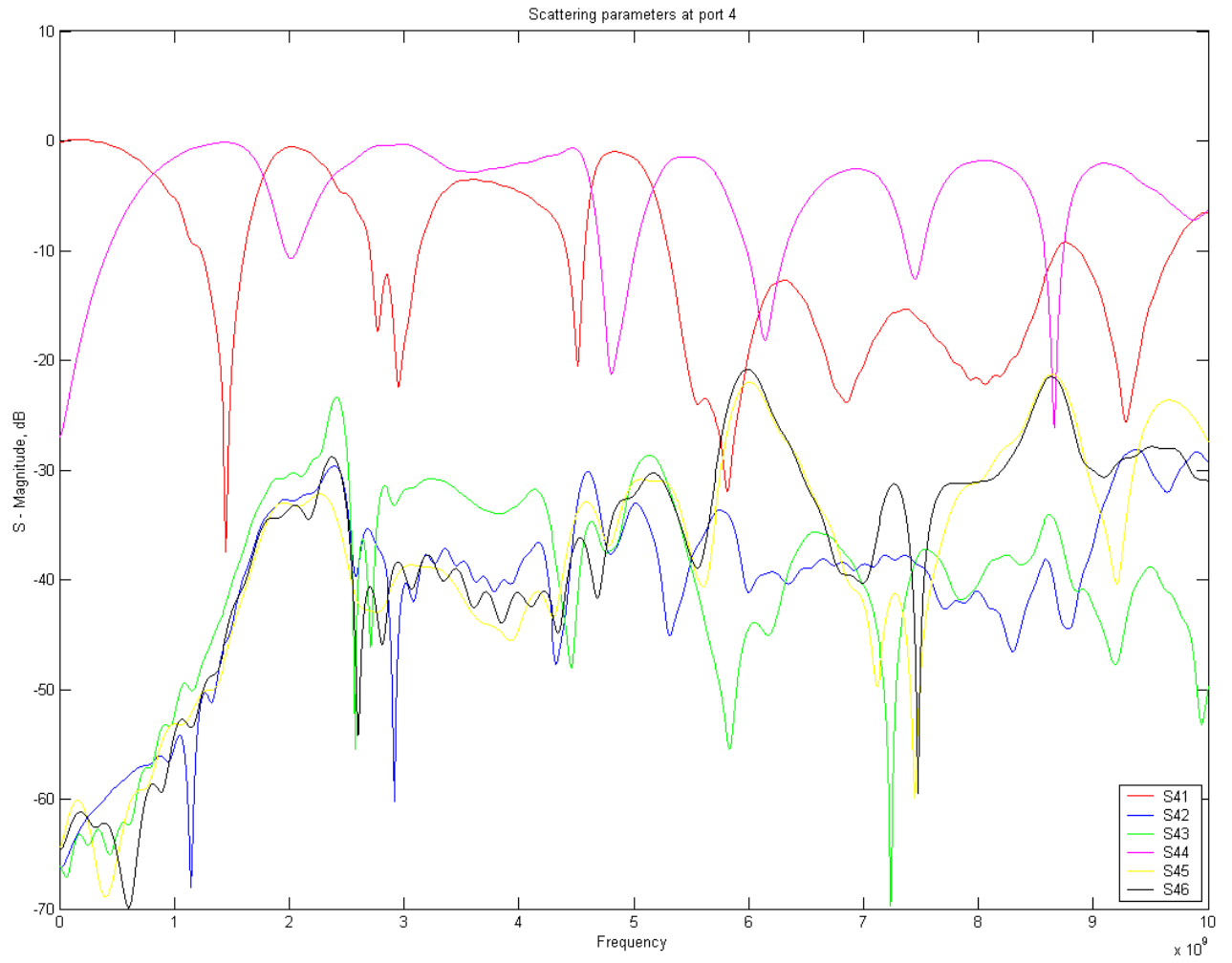
Figure 98.   Array scattering parameter at port 4
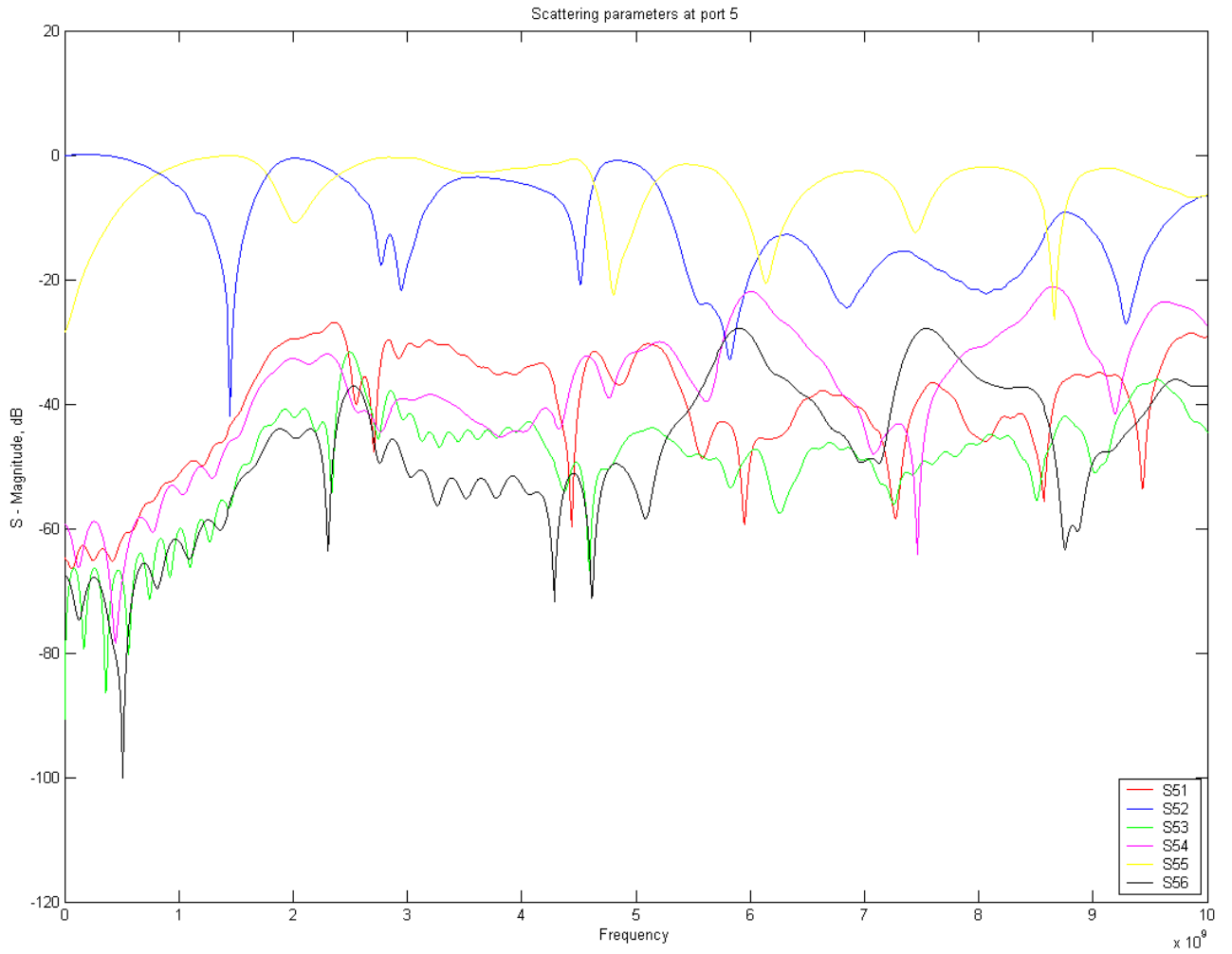
Figure 99.   Array scattering parameter at port 5
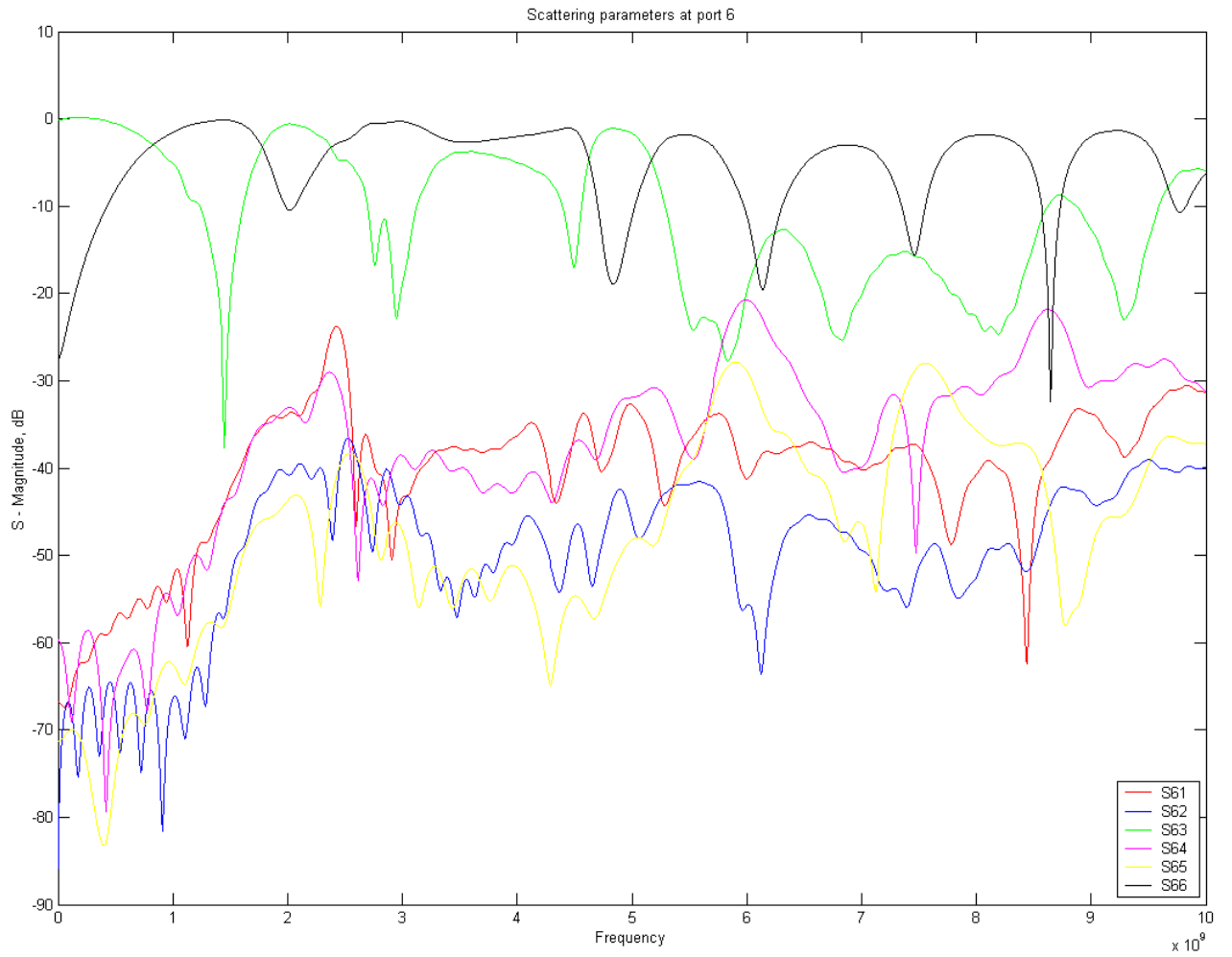
Figure 100.   Array scattering parameter at port 6

G. DIPOLE PATTERN MEASUREMENT SETUP
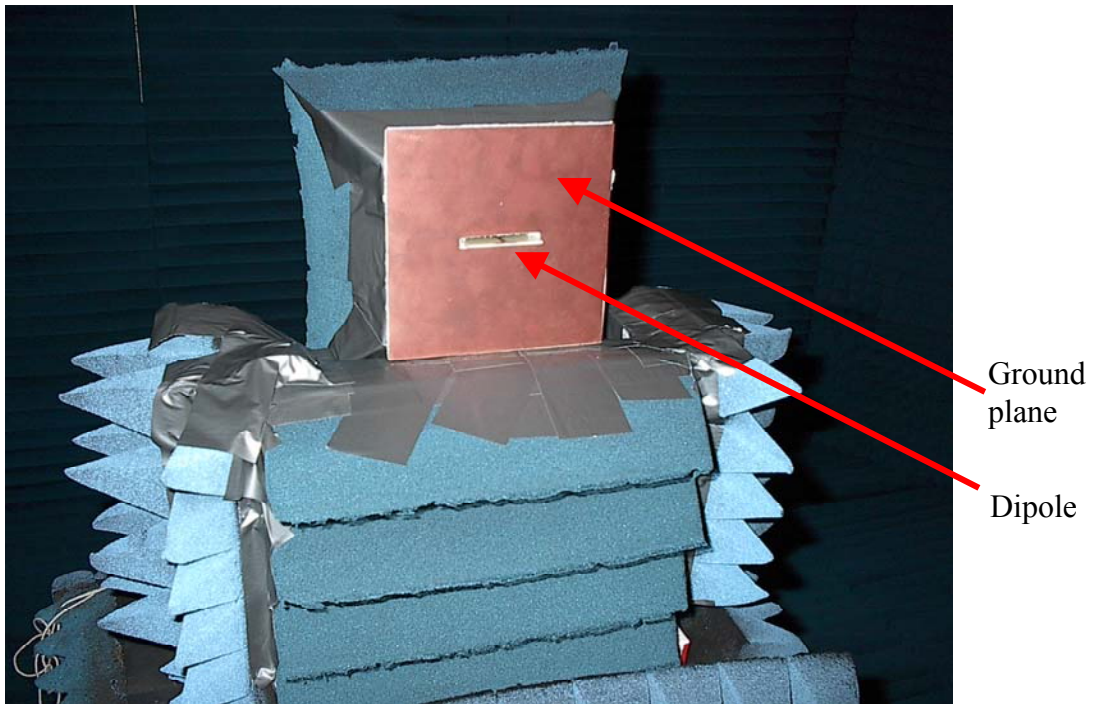
Figure 101.   Dipole with ground plane on turn-table (front view)
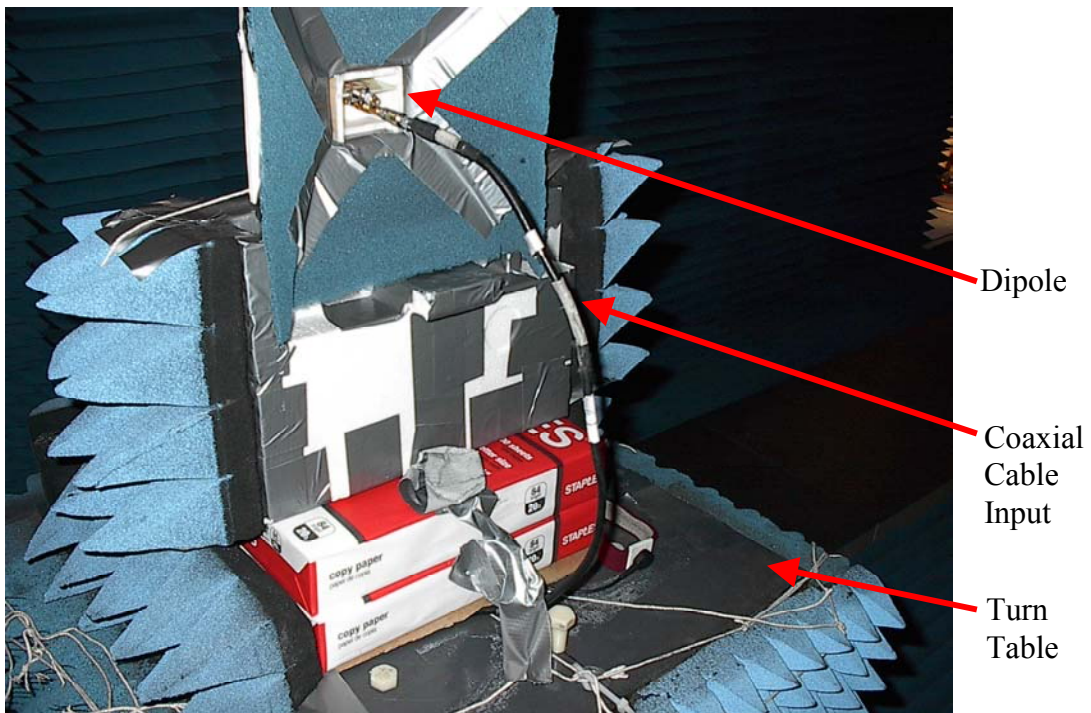
Figure 102.   Dipole with ground on turn-table (back view)

LIST OF REFERENCES

1.   David C. Jenn, Radar and Laser Cross Section Engineering, AIAA, 1995.

2.   David M. Pozar, *Microwave Engineering*, 2nd edition, John Wiley and Sons, Inc, 1997.

3.   Fawwaz T. Ulaby, *Fundamentals of Applied Electromagnetics*, 2001 edition, Prentice Hall, 2001.

4.   Warren L. Stutzman and Gary A. Thiele, *Antenna Theory and Design*, 2nd edition, Wiley, 1998.

5.   David C. Jenn, notes on Finte Element Method, 2002.

6.   B. Krietenstein, R. Schuhmann, P. Thoma, T. Weiland, "The Perfect Boundary Approximation Technique Facing the big Challenge of High Precision Field Computation," *19th International LINAC Conference*, August 1998.

7.   David C. Jenn, "A Complete Matrix Solution for Antenna Analysis," *1989 IEEE AP-S Symposium Digest*, June 1989.

8.   Yeo Chee Beng, "Effects of Mutual Coupling in Small Dipole Array Antenna," Naval Postgraduate School, Monterey, California, March 2002.

THIS PAGE INTENTIONALLY LEFT BLANK

INITIAL DISTRIBUTION LIST

1.   Defense Technical Information Center
        Ft. Belvoir, Virginia

2.   Dudley Knox Library
        Naval Postgraduate School
        Monterey, California

3.   Chairman
        Information Sciences Department
        Naval Postgraduate School
        Monterey, California

4.   Professor David C. Jenn
        Department of Electrical and Computer Engineering
        Naval Postgraduate School
        Monterey, California

5.   Professor Richard D. Adler
        Department of Electrical and Computer Engineering
        Naval Postgraduate School
        Monterey, California

6.   Major Chua Eng Hock
        Singapore